Water in confinement

Ultrafast dynamics of water in reverse micelles

Water in confinement

Ultrafast dynamics of water in reverse micelles

Academisch Proefschrift

ter verkrijging van de graad van doctor
aan de Universiteit van Amsterdam
op gezag van de Rector Magnificus
prof. dr. D. C. van den Boom
ten overstaan van een door het college voor promoties ingestelde
commissie, in het openbaar te verdedigen in de Agnietenkapel
op woensdag 19 maart 2008 om 10.00 uur

door

Adriaan Michiel Dokter

geboren te Haarlem

Promotiecommissie

promotor:	prof. dr. H. J. Bakker
co-promotor:	dr. S. Woutersen
overige leden:	prof. dr. M. Bonn
	prof. dr. E. J. J. Groenen
	prof. dr. K. J. Hellingwerf
	prof. dr. A. Lagendijk
	dr. E. J. Meijer

Faculteit der Natuurwetenschappen, Wiskunde en Informatica

ISBN 978-90-9022789-4

The work described in this thesis was performed at the FOM-*Institute for Atomic and Molecular Physics* (AMOLF), Kruislaan 407, 1098 SJ Amsterdam, The Netherlands. The work is part of the research programme of the *Stichting Fundamenteel Onderzoek der Materie* (FOM), which is financially supported by the *Nederlandse Organisatie voor Wetenschappelijk Onderzoek* (NWO).

Cover: Lake Manyara, Tanzania, 11 January 2005

"But don't think twice, it's all right"

Publications covered in this thesis

Adriaan M. Dokter, Sander Woutersen and Huib J. Bakker. Anomalous slowing down of the vibrational relaxation of liquid water upon nanoscale confinement. *Phys. Rev. Lett. 94*, 178301 (2005).

Adriaan M. Dokter, Sander Woutersen and Huib J. Bakker. Inhomogeneous dynamics in confined water nanodroplets. *Proc. Natl. Acad. Sci. U. S. A. 103*, 15355-15358 (2006).

Adriaan M. Dokter, Sander Woutersen and Huib J. Bakker. Ultrafast dynamics of water in cationic micelles. *J. Chem. Phys. 126*, 124507 (2007).

Adriaan M. Dokter and Huib J. Bakker. Transient absorption of vibrationally excited ice. *J. Chem. Phys. 128*, 024502 (2008).

Adriaan M. Dokter, Christian Petersen, Sander Woutersen and Huib J. Bakker. Vibrational dynamics of ice in reverse micelles. *J. Chem. Phys. 128*, 044509 (2008).

Contents

Chapter 1

Introduction

1.1 Water in confinement

Water plays a crucial role as a solvent in many systems found throughout biology and chemistry. Often such systems do not contain water as a bulk liquid, but as a limited number of water molecules in a confined environment.

The conformations of proteins and membrane sheets are often such that their surface encloses small pockets of water, either continuously or during part of their functional cycle. This is the case in a wide variety of phenomena such as protein–protein interactions, enzymatic catalysis and protein folding. In membrane lipid bilayers nanometre-sized reverse micelles are found during endosome formation [87], which contain fully (three-dimensionally) confined droplets of water.

Water at the interfaces of proteins and membranes is thought to be critical to their equilibrium structure and biological function [96,108]. Only in the presence of water these molecules fold or self-assemble into their functional form, however it is not well understood to what extent water is essential to these systems. Globular enzymes are known to be already functional at hydration levels below that required to cover their surface uniformly [108], while many proteins are only functional when being fully solvated by water.

Important questions can be raised on the effect of geometrical confinement on the properties of water itself: to what extent behave water molecules near a soft-matter interface differently than those in the bulk? And if these molecules do behave differently, what is the length scale over which an interface can affect the properties of water molecules?

Water molecules in the condensed phase have a strong mutual interaction in the form of hydrogen bonding. Each water molecule can accept two hydrogen bonds and donate two hydrogen bonds to other molecules. This hydrogen bonding is very directional, and as a result water is a highly structured liquid. Each molecule is near tetrahedrally coordinated to four other water molecules, and embedded in a dynamical hydrogen bond network made up by all other molecules. Contrary to other hydrogen bonded liquids, the hydro-

gen bond network of water is extended in space in three dimensions. Truncation of this hydrogen-bond network has a strong effect on its strength and structure [50, 51, 66]. Geometrical confinement by an interface may therefore collectively alter the properties of many water molecules, not only of the first solvation layer of the interface .

Reverse micelles have proven to be excellent model systems for studying the properties of water in strong confinement [79]. Such micelles consist of small aqueous droplets that are coated by a layer of surfactant molecules, which are dispersed in an apolar solvent. The hydrophilic head groups of the surfactant molecules point towards the micelle interior, while their hydrophobic tails point outward to the exterior solvent. For a large variety of surfactants and solvents, the size of the micelles can be easily varied, which makes it possible to tune the degree of confinement of water inside the micelles.

Mid-infrared spectroscopy is well suited for studying the hydrogen bonding properties of water. The O–H stretch vibration of a water molecule, which absorbs in this spectral region, is very sensitive to the precise strength or length of the hydrogen bond that is donated. The stronger is the hydrogen bond to an OH-group, the lower is the corresponding O–H stretch absorption frequency (See Fig. 1.1), which causes the O–H stretch absorption band of water to be strongly broadened.

The infrared absorption spectrum of water inside reverse micelles differs significantly from that of bulk water, as was shown by infrared absorption studies [21, 49, 51, 53, 63, 85]. The infrared line shapes deviate most strongly from bulk water for very small micelles, and converge to the bulk spectra for large micelles, as illustrated in Fig. 1.1. These observations show that the hydrogen bonding of water in reverse micelles changes as a result of confinement. Unfortunately, with conventional infrared spectroscopy it is not possible to distinguish the absorption contributions from molecules in the core of the micelles from those closer to the micelle outer wall. Hence, it remains unclear whether the confinement affects the hydrogen bonding of all molecules, or only that of a limited amount of molecules near the outer shell of the micelle.

Besides studying the steady-state absorption, other spectroscopic techniques are available that are sensitive to the molecular *dynamics* of water. These techniques can be used to study the effect of confinement on the motions of the water molecules, and enable studies on the dynamic properties of the water hydrogen bonding network. The dynamics of confined water in reverse micelles was first investigated by measuring the ^{1}H and ^{17}O spin-relaxation of water using Nuclear Magnetic Resonance (NMR) [26, 53, 75, 86, 100, 114, 130]. This work showed convincingly that the mobility of water slows down as a result of confinement. Because different types of water will rapidly exchange roles on the timescale of NMR (10^{-4} s), only information on the *average* mobility of confined water could be obtained. The same holds for more recent Quasi-Elastic Neutron Scattering studies [10, 56]. From these studies it is therefore not clear whether three-dimensional confinement lowers the mobility of many water molecules, or that a confining interface slows down the dynamics of only a few neighbouring

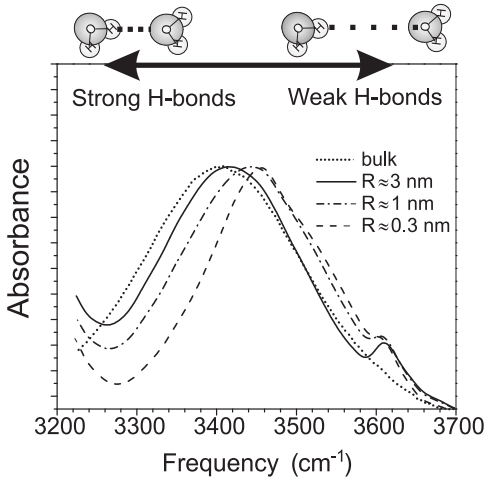

FIGURE 1.1. O–H stretch infrared absorption for bulk water (H_2O:D_2O=1:40) and water in AOT reverse micelles[a] of various sizes (the micelle radius R is approximately proportional to the parameter w_0 defined in chapter 3 (see Eq. 3.10 and 3.15), which had a value of 20,7 and 2 for the displayed spectra above, respectively. An approximate relation between R and w_0 can be found in reference [112]). There is a strong correlation between O–H stretch absorption frequency and hydrogen bond strength. Strong hydrogen bonds absorb primarily at the low frequency side, while weak hydrogen bonds absorb primarily at the high frequency side of the spectra. The absorption spectrum shifts to higher frequencies for water confined in smaller reverse micelles, which means on average the hydrogen bonds are weakening upon confinement.

molecules.

The development of ultrafast optical techniques has enabled studies on water dynamics in which the time-scales of molecular motions (ps to sub-ps) can be resolved. Several ultrafast experiments were recently reported in literature, aimed at a better understanding of the ultrafast dynamics of strongly confined water [30, 34, 37, 38, 46, 99, 109, 111, 112, 122]. Early ultrafast studies used small probe molecules to examine the interior water pool of reverse micelles [109]. In the work presented in this thesis we use mid-infrared pump-probe spectroscopy to study the dynamics of the O–H stretch vibration of water directly. This technique will prove to be very useful in distinguishing the dynamics of water molecules close to a soft-matter interface from water molecules further away.

[a]AOT (Sodium bis(2-ethylhexyl) sulfosuccinate) is the most commonly used surfactant in preparing water in oil reverse micelles.

1.2 Vibrational pump-probe spectroscopy

Vibrational pump-probe spectroscopy exploits the fact that vibrationally excited molecules have a somewhat different absorption spectrum than molecules in the vibrational ground state. Vibrationally excited molecules can be prepared by an intense laser pulse (which for now we assume to be unpolarised), which removes a fraction of molecules from the ground state to a vibrationally excited state. The sample is now no longer in a thermal equilibrium state, and we can measure the absorption difference $\Delta\alpha$ between this non-equilibrium state of the sample (of absorption α) and the unperturbed equilibrium state (of absorption α_0) at a time t after the pump pulse:

$$\Delta\alpha(\omega, t) \equiv \alpha_0(\omega) - \alpha(\omega, t). \tag{1.1}$$

Note that with this definition the absorbance change is positive in the case of increased transmission through the sample (bleaching) and negative in the case of decreased transmission (induced absorption) as a result of the pump pulse.

The vibrational excitation of molecules leads to three distinct contributions to the pump-probe spectrum. First, the excited molecules can be further excited from the first to the second excited state, causing increased (induced) absorption at frequencies matching this 1→2 transition. Decreased absorption (bleaching) is observed at the fundamental 0→1 transition as a result of two effects. First, the presence of less molecules in the ground state leads to a decreased ground state absorption. Second, stimulated emission from the excited state to the ground-state also decreases the absorption. Because of the equal probability for stimulated emission and absorption these two effects are of equal magnitude. Adding all terms we write for the absorption $\alpha(t)$ after excitation by the pump pulse

$$\alpha(\omega, t) = \underbrace{\alpha_0(\omega)}_{\text{equil. abs.}} - \underbrace{2\sigma_{01}(\omega)N_1(t)}_{\text{bleaching}} + \underbrace{\sigma_{12}(\omega)N_1(t)}_{\text{induced absorption}}, \tag{1.2}$$

where $N_1(t)$ is the number of excited molecules at time t after the pump pulse. With Eq. 1.1 we can write for the absorbance change

$$\Delta\alpha(\omega, t) = \sigma_{\mathrm{PP}}(\omega)N_1(t), \quad \sigma_{\mathrm{PP}}(\omega) = 2\sigma_{01}(\omega) - \sigma_{12}(\omega), \tag{1.3}$$

where we defined $\sigma_{\mathrm{PP}}(\omega)$ as the pure pump-probe spectrum. As a result of vibrational relaxation all molecules eventually decay to the ground state, causing the transmission change to decay to zero. The population of excited molecules in general decays exponentially

$$N_1(t) = N_1(0)e^{-t/T_1}, \tag{1.4}$$

where T_1 is the vibrational relaxation time constant.

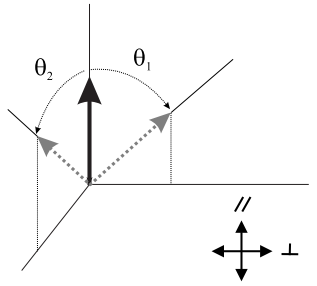

FIGURE 1.2. An absorbing dipole in the parallel polarisation direction can rotate over two independent angle θ_1 and θ_2. Rotation over both angles decreases the dipole component in the parallel polarisation direction. Rotation over angle θ_1 increases the dipole component in the perpendicular polarisation direction, but rotation over angle θ_2 does not.

1.2.1 Effect of Molecular Reorientation on the Absorbance

When linearly polarised light is used as a pump pulse, preferentially molecules that have their transition dipole parallel to the pump polarisation will be excited (See Eq. 2.6). This results in a stronger absorbance change for probe light polarised parallel to the pump polarisation ($\Delta\alpha_{\parallel}$) than for probe light polarised perpendicular to the pump polarisation ($\Delta\alpha_{\perp}$). The orientational distribution of excited molecules is initially anisotropic.

Besides vibrational relaxation there is now a second process that changes the amplitude of the absorbance in time, namely the orientational motions of the molecules. On average excited molecules will rotate out of the parallel probe polarisation direction into the perpendicular polarisation direction. This causes $\Delta\alpha_{\parallel}$ to decay more quickly and $\Delta\alpha_{\perp}$ more slowly than expected on the basis of the vibrational relaxation rate alone. We can average out the absorbance changes due to reorientation by constructing a combination of the signals $\Delta\alpha_{\parallel}$ and $\Delta\alpha_{\perp}$. In order to do so we should realise that in three dimensions a molecule with its transition dipole aligned parallel to the pump light polarisation has two independent degrees of freedom to reorient, as illustrated in Fig. 1.2. Reorientation in only one of these degrees of freedom causes the absorbance in the perpendicular polarisation direction to increase. Reorientation in the other degree of freedom leaves the absorbance in this polarisation direction unaffected. The inflowing flux of excited molecules into the perpendicular polarisation direction is therefore only *half* that of the outflowing flux from the parallel polarisation direction. To average out both fluxes we should thus average the signals as follows

$$\Delta\alpha_{\mathrm{RF}}(\omega,t) = \frac{\Delta\alpha_{\parallel} + 2\Delta\alpha_{\perp}}{3}. \tag{1.5}$$

This rotation free absorbance change $\Delta\alpha_{\mathrm{RF}}(\omega,t)$ now only reflects the vibra-

tional relaxation. The parallel and perpendicular absorbance can also be used to construct the anisotropy parameter $R(t)$:

$$R(\omega,t) = \frac{\Delta\alpha_{\parallel} - \Delta\alpha_{\perp}}{\Delta\alpha_{\parallel} + 2\Delta\alpha_{\perp}}. \tag{1.6}$$

This parameter decays only as a result of the orientational motions of the absorbing molecules, and not as a result of vibrational relaxation.

By more rigourous treatments of the effect of orientational motion on the time-dependent absorbance [121], it can be shown that in pump-probe and NMR experiments

$$R(t) = \frac{2}{5}\langle P_2(\cos\theta_{fi})\rangle \tag{1.7}$$

$$= \frac{2}{5}\langle(3\cos^2\theta_{fi} - 1)/2)\rangle, \tag{1.8}$$

where θ_{fi} equals the angle between the initial and final orientation of an initially excited molecule, $P_2(x)$ the second order Legendre polynomial and $\langle\ldots\rangle$ the ensemble average at time t. This relates the macroscopic observable $R(t)$ to the microscopic reorientational motions of individual molecules through an ensemble average[b]. In the case of reorientation as a rotational diffusion process with diffusion constant $D_{\rm or}$ the anisotropy parameter decays exponentially with time constant $\tau_{\rm or} = 1/(6D_{\rm or})$:

$$R(t) = \frac{2}{5}e^{-t/\tau_{\rm or}}. \tag{1.9}$$

We can understand the squared cosine dependence of the anisotropy parameter by realising that absorption experiments can only give information on the alignment ($\propto \cos^2\theta$) of molecules, not on their orientation ($\propto \cos\theta$). The absorption probability itself has a $\cos^2(\theta)$ dependence (Eq. 2.6), so by means of an absorption experiment no information can be obtained on the orientation of molecules.

1.2.2 Multiple component systems

Often systems are encountered that contain different components contributing to the pump-probe response that have different associated vibrational relaxation and reorientation time-constants. The rotation free signal is then of the form

$$\Delta\alpha_{\rm RF}(\omega,t) = \sum_i \Delta\alpha_{{\rm RF},i}, \quad \Delta\alpha_{{\rm RF},i} = A_i(\omega)e^{-t/T_{1,i}}, \tag{1.10}$$

[b] In terms of the correlation functions that will be discussed in chapter 2.3 we may realise that $\cos\theta_{fi}(t) = u(0)u(t)$ so that $R(t) = \frac{2}{5}C_{\rm or}(t) = \frac{2}{5}\langle P_2(u(0)u(t))\rangle$, where $C_{\rm or}(t)$ is usually referred to as the second order orientational correlation function. Depending on the experimental technique different correlation functions can be measured, for example dielectric relaxation experiments measure the first order correlation function $\langle P_1(\cos\theta_{fi})\rangle = \langle\cos\theta_{fi}\rangle$.

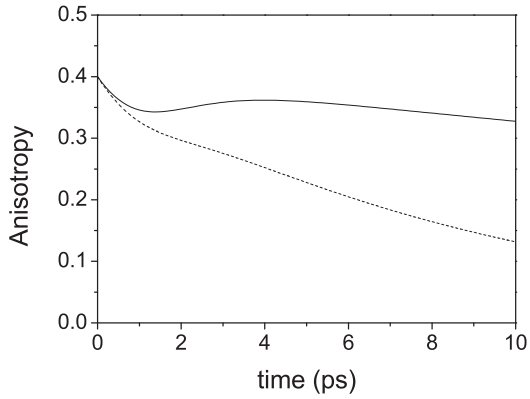

FIGURE 1.3. Example of the decay of the anisotropy parameter $R(t)$ for a two-component system. Component a has a vibrational lifetime and reorientation time characteristic of liquid water (diluted HDO in D_2O, $T_{1,a}$=0.7 ps, $\tau_{or,a}$=3 ps). Component b has a vibrational lifetime characteristic for water solvating an anionic group ($T_{1,b}$=3 ps). We illustrate the resultant anisotropy decay for two different reorientational time-constants for component b: dotted line $\tau_{or,b}$=9 ps, solid line $\tau_{or,b}$=50 ps. A_a:A_b=7:3.

where $A_i(\omega)$ is a pre-factor that depends on the concentration and cross-section of component i ($A_i(\omega) = \sigma_{PP,i}(\omega)N_{1,i}(0)$). The total anisotropy parameter will be a weighted average of the anisotropy parameters for the sub-ensembles of the different components:

$$R(\omega,t) = \sum_i f_i(\omega,t)R_i(t), \quad f_i(\omega,t) = \frac{\Delta\alpha_{\mathrm{RF},i}(\omega,t)}{\Delta\alpha_{\mathrm{RF}}(\omega,t)}. \tag{1.11}$$

If all vibrational relaxation times of the different components are equal ($T_{1,i} = T_1$), the time dependence of the weighing factors f_i drop out:

$$f_i(\omega) = A_i(\omega)/\sum_i A_i(\omega). \tag{1.12}$$

In this case the total anisotropy is just the weighted average (according to cross-section and concentration) of the anisotropy for the individual components. If each component has a different vibrational relaxation time, the anisotropy parameter becomes more difficult to interpret. As an example let us consider a system of two components a and b for which

$$A_a(\omega) > A_b(\omega), \quad T_{1,a} < T_{1,b}.$$

At early probe delays the a component dominates the signal because of its higher amplitude A_a. At later delays however, the A_b component starts to dominate

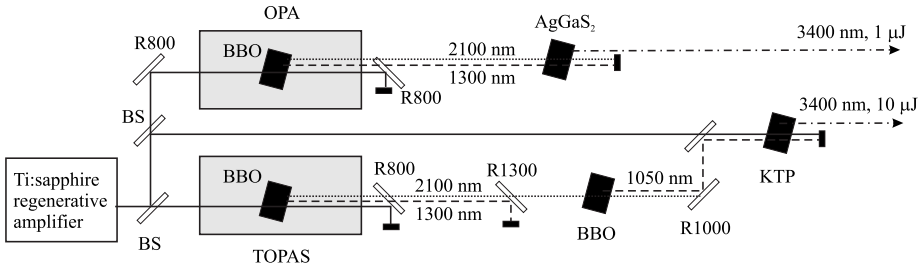

FIGURE 1.4. mid-infrared light generation scheme. Abbreviations: BS, Beam splitter; Rxxx, dielectric high-reflector for xxx nm light

because its signal decays much more slowly:

$$R(\omega,t) \simeq \begin{cases} R_{\mathrm{a}}(\omega,t) & \text{for } t \ll T_{1,\mathrm{a}}, \\ R_{\mathrm{b}}(\omega,t) & \text{for } t \gg T_{1,\mathrm{a}}. \end{cases}$$

In the time domain $0 < t < T_{1,\mathrm{b}}$ we will have the anisotropy parameter change its character from representing primarily the anisotropy value of component a to that of component b. How the anisotropy parameter evolves in time depends strongly on the exact values for the amplitude A_i and the reorientational and vibrational relaxation time-constants. This is illustrated in Fig. 1.3, where by increasing a single time constant the anisotropy decay is changed from fairly mono-exponential to highly non-exponential. An example of an experimentally measured anisotropy decay for a multiple component system can be found in Fig. 4.4.

1.3 Experimental methods

1.3.1 Generation of femtosecond mid-infrared laser pulses

In order to perform pump-probe spectroscopy on the O–H stretch absorption of water, we need two independently frequency-tunable pulses of mid-infrared light that can act as pump and probe pulses. There are no pulsed lasers available that emit light in the mid-infrared frequency range directly, and we therefore need to frequency convert the light from a commercial laser that emits light at a different wavelength. Our fundamental pulsed light source is a commercial Titanium:sapphire regenerative amplifier system (Quantronix Titan) which delivers pulses of 100 fs pulse length centred at 800 nm. The pulse repetition rate of the laser is 1 kHz and the pulse energy is 3 mJ. We use parametric generation in two separate Optical Parametric Amplifiers (OPA's) to create independently tunable pump and probe pulses. Both OPA's are based on wave mixing in a β-Barium-Borate (BBO) crystal. The mid-infrared light generation scheme is depicted in Fig. 1.4. The device used to generate the pump pulses

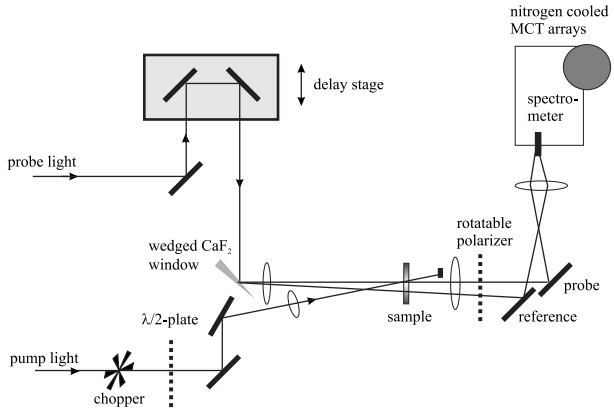

FIGURE 1.5. Experimental setup

is a 5-pass TOPAS (Travelling wave Optical Parametric Amplifier of Superfluorescence; Light Conversion, Ltd.). The BBO crystal in this device is tuned such that the fundamental 800 nm light is divided into photons of 1300 nm and 2100 nm. A second BBO crystal outside the TOPAS is used to generate the second harmonic of the 2100 nm light at 1050 nm. In the last generation step we use difference frequency mixing in a Potassium-Titanyl-Phosphate (KTP) crystal between a fresh part of the 800 nm pulse and the 1050 nm light. We then obtain mid-infrared light at 3400 nm with a pulse energy of $\sim$10 μJ.

The device used to generate the probe pulse is a 2-pass OPA (Spectra-Physics, Inc.) that uses a white-light continuum seed to start the parametric amplification. The white-light is generated by focussing a small fraction of 800nm light into a sapphire plate. The BBO crystal in the OPA is tuned such that the 800 nm pump light is divided into photons of 1300 nm and 2100 nm. Mid-infrared probe pulses are generated by difference frequency mixing of the signal and idler beams in a Silver-Gallium-Sulfide ($AgGaS_2$) crystal, resulting in 3-μm pulses of $\sim$1 μJ pulse energy. The probe pulses are spectrally broad compared to the pump pulses (200 cm^{-1} and 80 cm^{-1} FWHM, respectively). The time resolution is $\sim$150 fs.

1.3.2 Pump-probe setup

Figure 1.5 shows the setup used in the pump probe experiments. The probe beam is reflected off a wedged Calcium Fluoride (CaF_2) window to lower its intensity by 95%. The front and back reflections of the wedged window are used as probe and reference beam respectively. The pump and probe beam are overlapped and focussed in the sample, the foci having a diameter of approximately 200 μm and 150 μm. The probe focus is smaller than the pump focus such that the probe beam samples a volume that was rather evenly excited by the pump. The reference beam also passes the sample, but with its focus

at a different location. After the sample the transmitted probe and reference beams are sent through a polariser. Using an automated rotatable mount, the polariser can be set either parallel or perpendicular with respect to the pump polarisation, so that either the probe component parallel or perpendicular to the pump polarisation is transmitted.

Both the reference and probe beam are spectrally resolved using a polychromator. The probe and the reference are detected on two separate lines of a nitrogen-cooled Mercury-Cadmium-Telluride (MCT) detector array (3x32 pixels). When the polychromator is centred at 3400 cm^{-1}, the detector array can cover a spectral range of 500 cm^{-1}, which implies a spectral resolution of 15 cm^{-1}.

The probe light is sent over a computer-controlled delay stage. The relative delay t between the pump and probe pulses is varied by changing the path length travelled by the probe pulse. To measure the absorbance change induced by the pump pulse, the pump beam is chopped at 500 Hz so that the array measures alternatively the sample transmission with the pump beam present $[T(\omega, t)]$ and without the pump beam present $[T_0(\omega)]$. The absorbance change is defined as

$$\Delta\alpha(\omega, t) = \log(T(\omega, t)) - \log(T_0(\omega)). \tag{1.13}$$

The probe transmission is always recorded relatively to the reference transmission to divide out shot-to-shot noise, according to $T(\omega, t) = I_{\mathrm{pr}}(\omega, t)/I_{\mathrm{ref}}(\omega)$, where I_{pr} and I_{ref} are the intensities measured by the array detector. By this detection scheme the absorbance change is recorded at 500 Hz according to

$$\Delta\alpha(\omega, t) = \log\left(\frac{I_{\mathrm{pr}}(\omega, t)}{I_{\mathrm{ref}}(\omega)} \Big/ \frac{I_{\mathrm{pr},0}(\omega)}{I_{\mathrm{ref},0}(\omega)}\right). \tag{1.14}$$

Instead of measuring the parallel and perpendicular absorbance change consecutively using the rotatable polariser, both probe polarisation components can also be measured simultaneously by using a separate array line for each. The third array line is then used to record the reference spectrum. In this configuration measurements are sped up by a factor of two. Great care should however be taken that the parallel and perpendicular probe components are projected on the array with a relative frequency shift of less than $\sim$3 cm^{-1}, otherwise artifacts in the measured anisotropy parameter show up (See Fig. 1.6). Such precise alignment can be achieved by recording the linear absorption of a sample with a narrow absorption band (e.g. the overtone of the C=O-stretch for an acetone sample). By scanning the grating of the polychromator in 0.5 cm^{-1} frequency steps, the central frequency of the sharp absorption can be determined with high spectral resolution for each pixel. When the array is aligned properly, this central frequency should be equal for all pixels of all array lines.

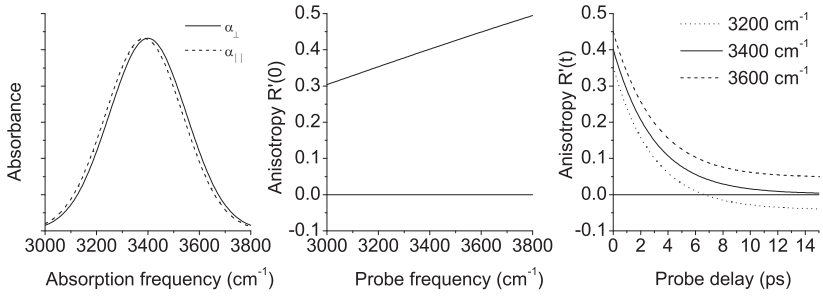

FIGURE 1.6. Illustration of anisotropy parameter artifacts that occur when the parallel and perpendicular absorbance change is recorded with a small relative frequency shift of $\delta = 15$ cm^{-1}, which is the spectral resolution of the array. The apparent anisotropy parameter $R'(t)$ then equals $\frac{\Delta\alpha_{\parallel}(\omega,t)-\Delta\alpha_{\perp}(\omega-\delta,t)}{\Delta\alpha_{\parallel}(\omega,t)+2\Delta\alpha_{\perp}(\omega-\delta,t)}$. The observed anisotropy decay is simulated for a Gaussian absorption band of 150 cm^{-1} spectral width, having an exponential anisotropy decay $R(t) = \frac{2}{5}e^{-t/3}$ at all absorption frequencies. The frequency shift δ introduces a frequency dependent start anisotropy $R'(0)$ and endlevels in the anisotropy decay of $R'(t)$ that are not present in the real anisotropy decay $R(t)$.

Chapter 2

Theory of light-matter interaction

The experimental technique of pump-probe spectroscopy is based on measuring the absorption of light in a sample in a time-resolved way, after the sample has been excited by an intense light pulse. In this chapter we present a theoretical description of the absorption of light by a molecular system. We aim to understand the light-absorbing properties of an ensemble of molecules as in the case of a disordered liquid like water. The light absorption of such an ensemble of molecules is found by averaging the absorbing properties of one molecule over all the states of the environment (or bath) of a molecule that can occur in the ensemble. In the case of a liquid, the environment of each molecule fluctuates in time and depends on the conformations and motions of its neighbouring molecules. In the case of the O–H stretch absorption of water it is mainly the spread and dynamics of the hydrogen bond O$\cdots$O coordinate that causes variation in the absorbing properties of each molecule [78, 104].

The theory presented here will be limited to what is needed to understand the experiments in the following chapters. More extended treatments of the quantum-mechanical description of light-matter interaction can be found in many textbooks, in particular references [19, 71, 84, 123].

2.1 Light absorption

Let us consider the molecular system (e.g. a water molecule in the liquid phase in a bath of neighbouring molecules) described by the equilibrium Hamiltonian $\hat{H}_0$. When this system is irradiated by a light field, it will experience the light's oscillating electric field component $\vec{E}(t)$:

$$\vec{E}(t) = E_0 \hat{\epsilon} \cos(\omega t), \tag{2.1}$$

where E_0 is the electric field amplitude and $\hat{\epsilon}$ its polarisation unit vector. The light field gives rise to a perturbing Hamiltonian $\hat{H}' = -\vec{\hat{M}} \cdot \vec{E}(t)$ to the system,

where $\vec{\hat{M}}$ equals the dipole operator of the system. The total Hamiltonian for the system is now given by $\hat{H}(t) = \hat{H}_0 + \hat{H}'(t)$.

The light field can induce transitions between the system states, for which the transition rates are given by Fermi's golden rule:

$$P_{i\to f}(\omega) = \frac{\pi E_0^2}{2\hbar^2}\left|\langle i|\hat{\mu}|f\rangle\right|^2[\underbrace{\delta(\omega_{fi}-\omega)}_{\text{abs.}}+\underbrace{\delta(\omega_{fi}+\omega)}_{\text{stim.em.}}], \tag{2.2}$$

where $\hat{\mu} = \hat{\epsilon}\cdot\vec{\hat{M}}$, $\omega_{fi} = (E_f - E_i)/\hbar$ the transition frequency between the states f,i of energy E_f, E_i. We see from this equation that the transition probabilities for stimulated emission ($E_f < E_i$) and absorption ($E_f > E_i$) are equal. If we want to know the rate of energy loss from the field we need to consider the difference in absorption and stimulated emission transition rates. These rates depend on the populations p_n of the levels, which obey a Boltzmann distribution at thermal equilibrium:

$$p_n = e^{-\beta E_n}/Z, \quad Z = \sum_n e^{-\beta E_n}, \tag{2.3}$$
$$p_n = \langle n|\hat{\rho}|n\rangle, \quad \hat{\rho} = e^{-\beta H_0}/\mathrm{Tr}[e^{-\beta H_0}].$$

The rate at which *energy* is transferred from state $i \to f$ is found by multiplying the transition rate by the photon energy and the thermal equilibrium population. The total energy transfer rate is found by summing the initial and final states (i,f) over all possible lower and upper states (n,m), where $E_n < E_m$:

$$\begin{aligned} P_{\text{abs}} &= \sum_{i,f=m,n}(p_i\cdot P_{i\to f})\cdot\hbar\omega_{fi} \\ &= \frac{\pi E_0^2}{2\hbar}\sum_{n,m}\omega_{mn}(p_n-p_m)\left|\langle n|\hat{\mu}|m\rangle\right|^2\delta(\omega_{mn}-\omega), \end{aligned} \tag{2.4}$$

where we used $\omega_{fi} = -\omega_{if}$ and $\delta(\omega) = \delta(-\omega)$. We should note that in the adopted formalism each state is characterised not only by the vibrational quantum state of the molecule, but also by the state of the environment or bath of the molecule. In Eq. 2.4 we are summing over all these bath and molecular system states.

It is useful to discuss the different terms in the expression for the absorbed power of Eq. 2.4. As discussed previously P_{abs} is proportional to the laser intensity ($\propto E_0^2$) and the photon energy ($\propto \omega_{mn}$). The delta function guarantees that only pairs of states whose energy difference matches the photon energy contribute to the absorption, which is an expression of energy conservation. The absorbed power scales with the population difference $p_n - p_m$ of each pair of states. The absorption vanishes when $p_n = p_m$ because then the rates of absorption and stimulated emission are equal and no net energy transfer from the light field to the system is achieved. The form of the squared matrix element $\left|\langle n|\hat{\mu}|m\rangle\right|^2$ will depend on the type of dipolar transition. To understand its

meaning in the context of vibrational spectroscopy it is useful to expand the dipole operator in terms of the vibrational coordinate x:

$$\vec{\hat{M}} \simeq \vec{M}_0 + \hat{x}\frac{\partial \vec{M}}{\partial x}. \tag{2.5}$$

Using $\hat{\mu} = \hat{\epsilon} \cdot \vec{\hat{M}} = |\vec{\hat{M}}| \cos\theta$ (where θ equals the angle between the system's transition dipole moment and the laser polarisation) and the above equation we find

$$\big|\langle n|\hat{\mu}|m\rangle\big|^2 = \big|\langle n|\hat{x}|m\rangle\big|^2 \Big(\frac{\partial \vec{M}}{\partial x}\Big)^2 \cos^2(\theta). \tag{2.6}$$

Each term in this expression implies an important selection rule in vibrational spectroscopy. For a harmonic system the term $\langle n|\hat{x}|m\rangle$ is only nonzero for $n = m \pm 1$, which shows that only transition are allowed that change the energy of the oscillator by one quantum of energy. The proportionality to $\left(\frac{\partial \vec{M}}{\partial x}\right)^2$ shows that only those vibrations are infrared active that modulate the dipole moment. As a consequence, symmetric vibrations such as those of O_2 or N_2 are not observed in infrared spectroscopy. The proportionality to $\cos^2(\theta)$ shows that the absorption probability depends on the relative alignment between the molecular dipole moment and the laser field polarisation. In a sample of randomly oriented oscillators linearly polarised light will induce an inhomogeneous orientational distribution of excited molecules, since more excited molecules will be found parallel to the light polarisation than perpendicular.

2.2 Absorption in terms of the dipole correlation function $C_\mu(t)$

The absorption cross section is conventionally defined as the absorbed power P_{abs} divided by the intensity of the incident light field $I = \frac{1}{2}c\epsilon_0 E_0^2$:

$$\alpha(\omega) = P_{\text{abs}}/I. \tag{2.7}$$

We use Eq. 2.3 to obtain the identity $p_n - p_m = p_n(1 - \exp[-\beta\hbar\omega_{nm}])$ and combine Eq. 2.4 and 2.7 to write

$$\alpha(\omega) = \frac{\pi}{\hbar c\epsilon_0}\omega(1 - e^{-\beta\hbar\omega})\sigma(\omega), \tag{2.8}$$

$$\sigma(\omega) = \sum_{n,m} p_n \big|\langle m|\hat{\mu}|n\rangle\big|^2 \delta(\omega_{mn} - \omega), \tag{2.9}$$

where $\sigma(\omega)$ is called the *line shape function* which only depends on the system and not on the laser field.

The line shape function can be written as a Quantum Time Correlation Function (QTCF). This can be derived using the following identity for the delta

function:

$$\delta(\omega) = \frac{1}{2\pi}\int_{-\infty}^{\infty} e^{i\omega t}dt. \tag{2.10}$$

Eq. 2.10 allows us to write the line shape as

$$\begin{aligned}\sigma(\omega) &= \frac{1}{2\pi}\sum_{n,m}\int_{-\infty}^{\infty} dt\ e^{i(\omega_{mn}-\omega)t}p_n\langle n|\hat{\mu}|m\rangle\langle m|\hat{\mu}|n\rangle \\ &= \frac{1}{2\pi}\sum_{n,m}\int_{-\infty}^{\infty} dt\ e^{-i\omega t}p_n\langle n|\hat{\mu}|m\rangle\langle m|e^{i\omega_m t}\hat{\mu}e^{-i\omega_n t}|n\rangle \\ &= \frac{1}{2\pi}\int_{-\infty}^{\infty} dt\ e^{-i\omega t}\sum_{n} p_n\langle n|\hat{\mu}(0)\hat{\mu}(t)|n\rangle, \end{aligned}\tag{2.11}$$

where in the last step we used the fact that the sum over m is a simple completeness identity and where we wrote the dipole operators in the interaction picture[a].

The sum over n represents the statistical thermal average[b] for the expectation value $\langle\hat{\mu}(0)\hat{\mu}(t)\rangle$. We can write shorthand $\langle ...\rangle$ for the thermal average and define the dipole quantum time correlation function (QTCF) by

$$C_\mu(t) = \big\langle\langle\hat{\mu}(0)\hat{\mu}(t)\rangle\big\rangle = \mathrm{Tr}\big[\hat{\rho}\hat{\mu}(0)\hat{\mu}(t)\big]. \tag{2.12}$$

We see that the line shape function equals the Fourier transform of the dipole QTCF, which is a quantum-mechanical formulation of the *Wiener-Khintchine theorem*:

$$\sigma(\omega) = \frac{1}{2\pi}\int_{-\infty}^{\infty} dt e^{-i\omega t}C_\mu(t). \tag{2.13}$$

Finally we would like to relate the complex line shape function to the real quantity for the absorption $\alpha(\omega)$. Combining Eq. 2.9 and Eq. 2.3 gives

$$\frac{\sigma(\omega_{ij})}{\sigma(\omega_{ji})} = \frac{p_j}{p_i} = e^{\beta\hbar\omega_{ij}}, \tag{2.14}$$

[a] We use $\langle m|e^{i\omega_m t} = \langle m|e^{iH_0 t/\hbar} = \langle m|U^\dagger(t)$ and $e^{-i\omega_n t}|n\rangle = e^{-iH_0 t/\hbar}|n\rangle = U(t)|n\rangle$ and the definition of the interaction picture operator $U^\dagger\hat{\mu}U = \hat{\mu}(t)$.

[b] For a system described by a wave function $|\Psi\rangle = \sum_n c_n|n\rangle$, one can define a density operator by $\rho \equiv |\Psi\rangle\langle\Psi| = \sum_{n,m} c_n^* c_m|n\rangle\langle m|$. The expectation value for an operator A is then given by $\langle A\rangle = \mathrm{Tr}(\rho A) = \sum_{n,m} c_n^* c_m\langle n|A|m\rangle$. We can show that this expression is equivalent to the summation in Eq. 2.11 by realising we are taking an ensemble average over N statistically independent molecules, written explicitly $\langle A\rangle = \frac{1}{N}\sum_{i=1}^{N}\sum_{n,m}\left(a_n^{(i)}\right)^* a_m^{(i)}\langle n|A|m\rangle = \sum_{n,m}\langle a_n^* a_m\rangle\langle n|A|m\rangle$. The equilibrium ensemble average of the expansion coefficients a_n is equivalent to phase averaging over these coefficients. Since at equilibrium all phases are equally probable $\langle a_n^* a_m\rangle = \frac{1}{2\pi}\int |a_n||a_m|e^{-i\phi_{nm}}d\phi_{nm} = |a_n||a_m|\delta_{nm}$, where we used $a_n = |a_n|e^{i\phi_n}$ and $\phi_{nm} = \phi_n - \phi_m$. This gives us for $\langle A\rangle = \sum_n |a_n|^2\langle n|A|n\rangle$, where at equilibrium $|a_n|^2 = p_n$ (Eq. 2.3). This also shows why the thermal equilibrium density matrix (Eq. 2.3) only has diagonal elements.

which since $\omega_{ij} = -\omega_{ji}$ is equivalent to

$$\sigma(-\omega) = \sigma(\omega)^* = e^{-\beta\hbar\omega}\sigma(\omega). \tag{2.15}$$

By use of this equation we can rewrite Eq. 2.8 as

$$\alpha(\omega) = \frac{\pi\omega}{3\hbar c\epsilon_0}\mathrm{Im}(\sigma(\omega)). \tag{2.16}$$

An additional averaging factor was introduced in the above equation because the cross section is a quantity that is averaged over all molecular orientations, and independent of the alignment with respect to the laser polarisation. Averaging out the $cos^2\theta$ dependence of Eq. 2.6 over a unit sphere results in an averaging factor of 1/3.

2.3 $C_\mu(t)$ for a two-level system in a classical bath

Certain systems may have two groups of characteristic frequencies, ω_H and ω_L, where the energy of the low frequencies modes $\hbar\omega_\mathrm{L}$ is much smaller than the thermal energy:

$$\hbar\omega_\mathrm{L} \ll k_B T \ll \hbar\omega_\mathrm{H}. \tag{2.17}$$

We can then treat the slow modes classically and the fast modes quantum-mechanically. The fact that $\omega_\mathrm{H} \gg \omega_\mathrm{L}$ suggests making an adiabatic approximation. Each system state $|i\rangle$ can be regarded to consist of a bath contribution and a molecular system contribution, as $|i\rangle = |\phi_b\rangle|\psi_s\rangle$, and the total density matrix describing the system state may be written as the combined density matrix for the system and the bath $\hat{\rho} = \hat{\rho}_s \otimes \hat{\rho}_b$.

We will focus on one transition from the vibrational ground state $|g\rangle$ to a certain excited state $|e\rangle$ of a high frequency mode. We may then write

$$\hat{H}_0 \simeq \hat{H}_g|g\rangle\langle g| + \hat{H}_e|e\rangle\langle e|, \tag{2.18}$$

$$\hat{\mu} = \hat{\epsilon}\cdot\hat{\vec{M}} \simeq \tilde{\mu}\big[|g\rangle\langle e| + |e\rangle\langle g|\big], \tag{2.19}$$

where the bra and kets equal the system part $|\psi_s\rangle$ of the wave function. Note that we neglect diagonal terms for the dipole moment, which in general is an approximation but exact for harmonic systems. Both $\tilde{\mu}$, $\hat{H}_g$ and $\hat{H}_e$ depend on the bath coordinates[c]. Since the excited state energy is much higher than the thermal energy we may assume all population is in the vibrational ground state, so that we may write for the system density matrix $\hat{\rho}_s$:

$$\hat{\rho}_s \simeq |g\rangle\langle g|, \quad \hat{\rho} = \hat{\rho}_s \otimes \hat{\rho}_b \simeq \hat{\rho}_b|g\rangle\langle g|. \tag{2.20}$$

[c]Additionally, the energy of a bath mode need not be equal in the ground and excited state, that is the energies $\langle\phi_b|\langle g|\hat{H}_0|g\rangle|\phi_b\rangle = \langle\phi_b|\hat{H}_g|\phi_b\rangle$ and $\langle\phi_b|\langle e|\hat{H}_0|e\rangle|\phi_b\rangle = \langle\phi_b|\hat{H}_e|\phi_b\rangle$ may differ more than just the energy difference between the system states $|e\rangle$ and $|g\rangle$.

The dipole QTCF can now be rewritten by tracing out the system coordinates only, according to

$$\begin{aligned} C_\mu(t) &= \mathrm{Tr}\big[\hat{\rho}\hat{\mu}(0)\hat{\mu}(t)\big] \\ &= \mathrm{Tr}_b\mathrm{Tr}_s\big[\hat{\rho}\hat{\mu}e^{i\hat{H}t/\hbar}\hat{\mu}e^{-i\hat{H}t/\hbar}\big] \\ &\simeq \mathrm{Tr}_b\big[\hat{\rho}_b\widetilde{\mu}e^{i\hat{H}_e t/\hbar}\widetilde{\mu}e^{-i\hat{H}_g t/\hbar}\big] \\ &= \mathrm{Tr}_b\big[\hat{\rho}_b\widetilde{\mu}(0)F(t)\widetilde{\mu}(t)\big], \end{aligned} \tag{2.21}$$

where we defined the bath density matrix $\hat{\rho}_b = e^{-\beta\hat{H}_g}/\mathrm{Tr}_b[e^{-\beta\hat{H}_g}]$, the time evolution of the dipole moment on the ground state $\widetilde{\mu}(t) = e^{i\hat{H}_g t/\hbar}\widetilde{\mu}e^{-i\hat{H}_g t/\hbar}$ and the dephasing function $F(t) = e^{i\hat{H}_e t/\hbar}e^{-i\hat{H}_g t/\hbar}$. Since the bath coordinates can be treated classically, the only remaining quantum-mechanical operator is the dephasing function. We can write for the time-evolution of the dephasing function

$$\begin{aligned} \frac{d}{dt}F(t) &= e^{i\hat{H}_e t/\hbar}\Big(\frac{i\hat{H}_e}{\hbar} - \frac{i\hat{H}_g}{\hbar}\Big)e^{-i\hat{H}_g t/\hbar} \\ &= F(t)\ i\omega_{eg}(t), \end{aligned} \tag{2.22}$$

where in the last equation we inserted the identity $e^{-i\hat{H}_g t/\hbar}e^{i\hat{H}_g t/\hbar}$ and we defined $\omega_{eg}(t) = e^{i\hat{H}_g t/\hbar}\hat{\omega}_{eg}e^{-i\hat{H}_g t/\hbar}$; $\hat{\omega}_{eg} = (\hat{H}_e - \hat{H}_g)/\hbar$. $F(t)$ is often approximated by

$$F_\mathrm{c}(t) = e^{i\int_0^t d\tau\ \omega_{eg}(\tau)}, \tag{2.23}$$

where $\omega_{eg} = (E_e - E_g)/\hbar$ equals the vertical transition frequency. This approximation is very useful practically since this also makes $F(t)$ a classical expression in the case of a classical bath.

Our final result is that when only one vibrational transition is considered and we assume a classical fluctuating bath, the dipole QTCF can be approximated by the classical correlation function

$$C_\mu(t) = \Big\langle \widetilde{\mu}(0)\widetilde{\mu}(t)\ F_\mathrm{c}(t)\Big\rangle. \tag{2.24}$$

If we write $m(t) = |\widetilde{\mu}(t)|$ as the magnitude of the transition dipole moment and $\mathrm{u(t)}{=}\hat{\epsilon}\cdot\hat{M}$ as the molecular orientation we find

$$C_\mu(t) = \Big\langle \underbrace{u(0)u(t)}_{\text{rotations}}\quad \underbrace{m(0)m(t)}_{\text{non-Condon effects}}\quad \underbrace{e^{i\int_0^\tau \omega_{eg}(\tau)d\tau}}_{\text{spec. diff.}}\Big\rangle. \tag{2.25}$$

Instead of averaging the dipole correlation operator over all states we can now average over a representative ensemble of trajectories for $u(t)$, $m(t)$ and $\omega_{eg}(t)$. The final line shape is determined by different physical mechanisms. The first are rotations, which can often be neglected since the rotational correlation function $u(t)u(0)$ decays usually much slower than the dephasing function. Another

contribution results from fluctuations in the magnitude of the transition dipole moment (non-Condon effects). The last term refers to dephasing between oscillators as a result of differences in transition frequency and as a result of spectral diffusion.

2.4 Lineshapes

From Eq. 2.25 we learn that the absorption lineshape for an ensemble of molecules depends intimately on the way in which the orientation, transition dipole moment and phase of each molecule evolves and fluctuates in time. Fluctuations are caused by the interaction of each molecule with its bath or environment. We discuss the resulting line shape for a single (vibrational) transition of an ensemble of molecules, for different types of such bath fluctuations. To simplify the discussion we will assume that reorientations are slow compared to the typical decay time of the correlation function (u(t)u(0)=1) and make the Condon approximation by assuming the transition dipole m(t) is constant and equal for all oscillators (m(0)m(t)=$\bar{\mu}^2$). We then have

$$\sigma(\omega) \sim \int_{-\infty}^{\infty} dt\ e^{-i\omega t} \Big\langle e^{i\int_0^t \omega(\tau)d\tau} \Big\rangle. \tag{2.26}$$

If the spectral diffusion is slow we can replace $\omega(\tau)$ by $\omega(0)$ and then we find by Eq. 2.10

$$\sigma(\omega) \sim \Big\langle \delta(\omega - \omega(0)) \Big\rangle, \tag{2.27}$$

which shows that the line shape is simply the distribution of frequencies. This is the *inhomogeneous broadening* limit. We may also suppose that each oscillator is randomly perturbed, so that its frequency is modulated in a random fashion around a mean frequency $\langle\omega\rangle$ within a standard deviation Δ.

$$\delta\omega(t) \equiv \omega(t) - \langle\omega\rangle, \quad \langle\delta\omega^2\rangle \equiv \Delta^2, \tag{2.28}$$

then

$$\sigma(\omega) \sim \int_{-\infty}^{\infty} dt\ e^{-i(\omega-\langle\omega\rangle)t} \bar{F}_{\rm c}(t), \tag{2.29}$$

$$\bar{F}_{\rm c}(t) = \Big\langle e^{i\int_0^t \delta\omega(\tau)d\tau} \Big\rangle. \tag{2.30}$$

In this way we removed the fast oscillating mean frequency factor from the ensemble averaged dephasing function $\bar{F}_{\rm c}(t)$. We may assume that the variation $\delta\omega(t)$ is a stochastic Gaussian process. In that case we can make the cumulant

approximation[d] and write:

$$\bar{F}_{\rm c}(t) = e^{-g(t)}, \quad g(t) = \int_0^t d\tau \int_0^\tau d\tau' C_\omega(\tau'), \tag{2.34}$$

$$C_\omega(t) = \big\langle \delta\omega(t)\delta\omega(0)\big\rangle, \tag{2.35}$$

where C_ω is the frequency time correlation function (FTCF). If we assume that $C_\omega(t)$ decays exponentially

$$C_\omega(t) = \Delta^2 e^{-t/\tau_{\rm c}}, \tag{2.36}$$

we find from Eq. 2.34

$$g(t) = (\Delta\tau_{\rm c})^2\Big(\frac{t}{\tau_{\rm c}} - 1 + e^{-t/\tau_{\rm c}}\Big). \tag{2.37}$$

It is instructive to discuss two limiting cases. If $\Delta\tau_{\rm c} \gg 1$ we find

$$g(t) \simeq \frac{\Delta^2 t^2}{2}, \tag{2.38}$$

$$\Rightarrow \sigma(\omega) \sim \exp\Big[-\frac{(\omega - \langle\omega\rangle)^2}{2\Delta^2}\Big] \equiv \sigma_{\rm inhom}(\omega), \tag{2.39}$$

by which we retrieve the *inhomogeneous broadening limit* of Eq. 2.27 for a normal distribution of frequencies for the oscillators of width Δ. If $\Delta\tau_{\rm c} \ll 1$ we find

$$g(t) \simeq \Delta^2\tau_{\rm c} t \equiv \frac{t}{T_2^*}, \tag{2.40}$$

$$\Rightarrow \sigma(\omega) \sim \frac{1}{(\omega - \langle\omega\rangle)^2 + (\frac{1}{T_2^*})^2} \equiv \sigma_{\rm hom}(\omega), \tag{2.41}$$

where $T_2^* = 1/(\Delta^2\tau_{\rm c})$ is the so-called "pure dephasing" time. This limit of frequency modulation is referred to as the *homogeneous broadening limit*. The

[d] According to the cumulant expression [71] the average $\langle\exp[ikx]\rangle$ of the stochastic variable x can be written as

$$\exp\Big[ikC_1 + \frac{(ik)^2}{2!}C_2 + \frac{(ik)^3}{3!}C_3 + \dots\Big], \tag{2.31}$$

where the cumulants C_i are given by

$$C_1 = \langle x\rangle, \quad C_2 = \langle x^2\rangle - \langle x\rangle^2, \quad C_3 = \langle x^3\rangle - 3\langle x^2\rangle\langle x\rangle + 2\langle x\rangle^3. \tag{2.32}$$

A stochastic process is Gaussian if the probability distribution of its observables are normal distributions. Under this assumption only the first two cumulants are nonzero, so that with $x = \int_0^t \delta\omega(t')dt'$, $k = 1$ and $\langle x\rangle = 0$ (Eq. 2.28) we obtain

$$\Big\langle e^{i\int_0^t \delta\omega(\tau)d\tau}\Big\rangle = e^{-g(t)}, \quad g(t) = \frac{1}{2}\int_0^t dt' \int_0^t dt''\langle\delta\omega(t')\delta\omega(t'')\rangle. \tag{2.33}$$

The function $g(t)$ can be written as Eq. 2.34 by a simple change of integration variable.

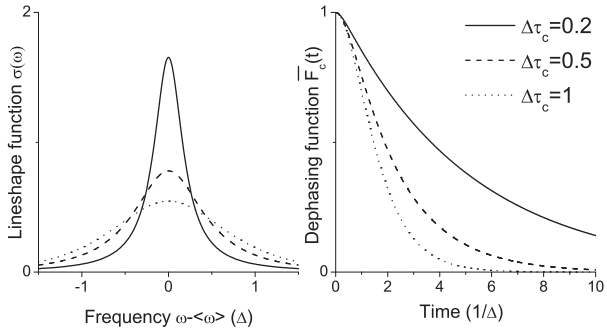

FIGURE 2.1. Line shape and dephasing function $\bar{F}_{\rm c}(t)$ for different values of $\Delta\tau_{\rm c}$ in the case of a Gaussian frequency modulation process and frequency distribution. $\Delta\tau_{\rm c}$ equals the width of the (instantaneous) frequency distribution times the decay time of the frequency time correlation function (FCTF). In the inhomogeneous limit ($\Delta\tau_{\rm c} \gg 1$) both the line shape and the dephasing function have a Gaussian shape. In the inhomogeneous limit ($\Delta\tau_{\rm c} \ll 1$) the line shape is Lorentzian and the dephasing function decays exponentially.

line shape is now a Lorentzian. For the line widths (Full width at half the maximum, FWHM) we find[e]

$$\begin{aligned} \mathrm{FWHM}_{\rm inhom} &= 2\sqrt{2\log 2}\Delta, \\ \mathrm{FWHM}_{\rm hom} &= \frac{2}{T_2^*} = 2\Delta^2\tau_{\rm c}, \end{aligned} \tag{2.42}$$

which shows that the homogeneous line is considerably narrowed with respect to the inhomogeneous line (by a factor $\Delta\tau_{\rm c}/\sqrt{2\log 2} \ll 1$, assuming equal widths Δ for the frequency distributions in both limits). The absorption line of a distribution of oscillators can be infinitely narrowed just by increasing the speed of the frequency fluctuations, which are characterised by the time $\tau_{\rm c}$. The homogeneous limit is therefore also referred to as the *motional narrowing limit*. In the next paragraph we will see that for real systems the finite lifetime of a transition (due to vibrational relaxation) causes additional line broadening. An absorption can therefore only be motionally narrowed up to the width dictated by this lifetime broadening.

For later reference we define the characteristic decay time T_2 of the dipole correlation function $C_\mu(t)$:

$$T_2 \equiv \int_0^\infty C_\mu(t)dt. \tag{2.43}$$

[e]Note that the adopted frequency unit is [rad/s]. The widths in SI units of [1/s] are obtained by dividing both expressions by 2π.

We find for T_2 in both limits

$$T^*_{2,\mathrm{inhom}} = \sqrt{\pi/2}/\Delta, \tag{2.44}$$

$$T^*_{2,\mathrm{hom}} = 1/(\Delta^2 \tau_\mathrm{c}). \tag{2.45}$$

In the formalism presented up to now the decay of $C_\mu(t)$ only results from dephasing of the dipoles (and not as a result of population relaxation, as discussed in the following section). In that case the decay time of $C_\mu(t)$ is referred to as a pure dephasing time. Pure dephasing times are often written as T_2^*, and we adopted the same notation in the above expression.

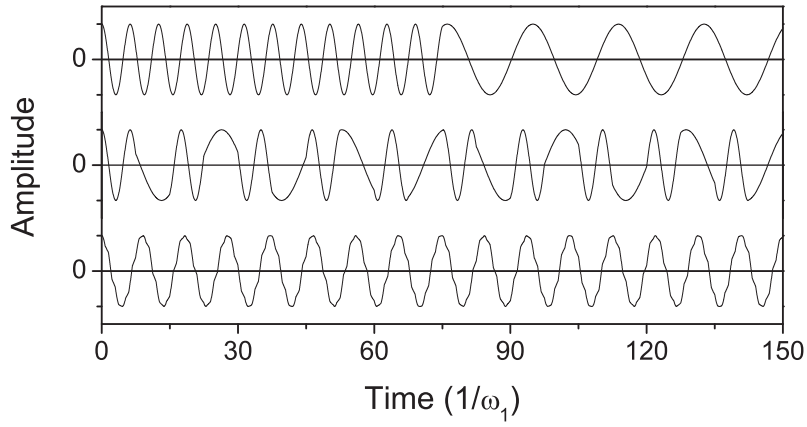

FIGURE 2.2. Amplitude of an oscillator that switches its oscillation frequency back and forth from ω_1 to $\omega_2 = \omega_1/3$ with a time constant of $150/\omega_1$, $15/\omega_1$ or $1.5/\omega_1$ (top to bottom). In the case of the slowest switching time (i.e. slow spectral diffusion) both frequency components are clearly discernable. In the case of the fastest switching time (i.e. fast spectral diffusion) the oscillator adopts a mean frequency $\langle\omega\rangle = (\omega_1 + \omega_2)/2$, and the power spectrum will contain a single peak at $\langle\omega\rangle$ instead of a broader spectrum with two peaks at ω_1 and ω_2. This is a manifestation of motional narrowing. A temporary switch of the frequency is only meaningful as a frequency change if it keeps the new value for at least an oscillation period ($T \approx 2\pi/\omega$). In case of a distribution of such oscillators, the situation is as follows: when all oscillators tend to the mean frequency of their frequency distribution as a result of a fast spectral diffusion process, they will remain in phase much longer than in the case where they would oscillate at distinct frequencies. The dephasing function $\bar{F}_\mathrm{c}(t)$ will decay much more slowly accordingly, and the line shape will be narrowed.

2.5 Vibrational relaxation

If we consider an isolated molecule, its instantaneous frequency will be continuously modulated by thermally induced variations in its environment. The frequency width Δ of sampled frequencies is however very narrow for a single molecule, which will bring the frequency modulations in the homogeneous limit ($\Delta\tau_c \ll 1$). The absorption profile of isolated molecules is therefore always Lorentzian.

We should realise that besides the population transfer that can be induced by a perturbing light-field (as given by Fermi's golden rule, Eq. 2.2), there are also intrinsic transition rates between all states. These intrinsic transition rates are such that in absence of any light field the system adopts the Boltzmann population of Eq. 2.3. When a two-level system is brought out of equilibrium by increasing the amount of excited state amplitude, this excited state population will decay back to the ground state until thermal equilibrium is recovered. T_1 is the characteristic decay time for this process of *(vibrational) population relaxation.*

The only observable determining the line shape is the dipole correlation function $C_\mu(t)$, which decays exponentially in the homogeneous limit. We will now show that a vibrational relaxation process leads to the exact same exponential decay of $C_\mu(t)$, which shows that fast frequency modulation and vibrational relaxation lead to an identical form of the observables. In order to do so we will look at the expectation value of the dipole moment itself (instead of at its auto-correlation). We may write for the wave function and system density matrix of a two-level system

$$|\psi_s\rangle = c_g|g\rangle + c_e|e\rangle, \quad \hat{\rho}_s = |\psi_s\rangle\langle\psi_s|. \tag{2.46}$$

With Eq. 2.19 we can calculate the expectation value for the dipole moment

$$\langle\mu\rangle = \mathrm{Tr}(\rho_s\mu) = \widetilde{\mu}(c_g c_e^* + c_e c_g^*). \tag{2.47}$$

Assuming a temperature where at equilibrium nearly all population will be in the vibrational ground state, we phenomenologically introduce population relaxation according to

$$p_g = |c_g|^2 \simeq 1, \quad p_e \simeq |c_e|^2 e^{-t/T_1}. \tag{2.48}$$

The introduction of vibrational relaxation is equivalent to the transformation $c_e \rightarrow c_e e^{-t/2T_1}$, which makes the system density operator ρ_s time dependent. By inspection of Eq. 2.47 we see that population relaxation also leads to a decay of the dipole moment amplitude:

$$\langle\mu\rangle \propto \widetilde{\mu} e^{-t/2T_1}. \tag{2.49}$$

We can incorporate vibrational relaxation in the dipole correlation function phenomenologically by rewriting Eq. 2.24 as

$$\widetilde{C}_\mu(t) = \left\langle \widetilde{\mu}(0)\widetilde{\mu}(t) e^{-t/2T_1} F_c(t) \right\rangle. \tag{2.50}$$

When taking vibrational relaxation into account, the total dipole dephasing is no longer only determined by the T_2^* time, but also by the vibrational relaxation time T_1. The effective dipole dephasing time T_2 is found by Eq. 2.43:

$$T_2 = \int_0^\infty \widetilde{C}_\mu(t) = \int_0^\infty C_\mu(t) e^{-t/2T_1} dt. \tag{2.51}$$

If $C_\mu(t)$ is an exponentially decaying function with decay time T_2^* (as it is in the homogeneous limit) we find

$$\frac{1}{T_2} = \frac{1}{2T_1} + \frac{1}{T_2^*}. \tag{2.52}$$

Motional narrowing only affects the T_2^* time, which can be brought to infinity in the case of very fast frequency fluctuations (very short τ_c). Nevertheless the dipole dephasing time T_2 can never be slower than twice the vibrational lifetime, which puts a lower limit to the FWHM line width of $1/T_1$ (see Eq. 2.42). The spectral broadening related to vibrational relaxation is referred to as *lifetime broadening*.

Chapter 3

Thermodynamics of reverse micellar systems

3.1 Introduction

Reverse micelles are isolated, surfactant-coated water droplets, which have emerged as a useful model for confined water in biological systems [79]. In this thesis we use reverse micelles as a model system for studying the effect of confinement on the dynamic properties of water. The interior dimensions of reverse micelles are similar to confined spaces found in cavities in biological systems. Reverse micelles form spontaneously when water, surfactants, and nonpolar solvents are mixed at the appropriate concentrations. The charge of the head group of the surfactant molecules may be either cationic, anionic or neutral [45] (See Fig. 3.1). By using different types of surfactants in preparing reverse micelles, we can vary the properties of the micellar interface, and study its effect on adjoining water molecules. In this chapter we will discuss the thermodynamic conditions for (reverse) micelle self-assembly. We will highlight the dominant forces stabilising the micellar structure, and discuss the distribution of solvated ions inside ionic reverse micelles. Further information can be found in references [2, 45, 61, 128].

3.2 Thermodynamic equations of self-assembly

Micelles and reverse micelles form spontaneously under the right conditions, which one may refer to as a process of self-assembly. To understand why certain systems exhibit (reverse) micelle formation, we will first provide a thermodynamic description of the aggregation behaviour of molecules in general. For the formation of aggregates B_N consisting of N molecules B_1 we can write down the reaction

$$NB_1 \underset{k_N}{\overset{k_1}{\rightleftharpoons}} B_N. \tag{3.1}$$

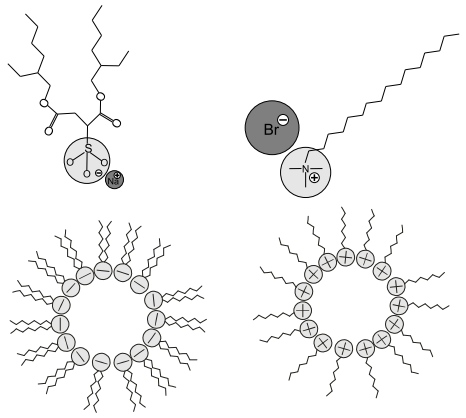

FIGURE 3.1. Schematic of water-in-oil reverse micelles. The water pool is coated with a mono-layer surfactant molecules. Left: Anionic surfactant salt AOT (Bis(2-ethylhexyl) sulfosuccinate). Right: Cationic surfactant salt CTAB (Cetyltrimethylammonium bromide)

For this reaction we can write down the equilibrium constant k_{eq} according to the familiar law of mass action

$$k_{eq} = k_1/k_N = \frac{[B_N]}{[B_1]^N} = \frac{X_N}{NX_1^N}, \tag{3.2}$$

where we defined X_N as the concentration[a] (as a dimensionless mole fraction) of molecules in aggregates of number N, so that $[B_N] = X_N/N$.

The reaction constant k_{eq} is related to the difference in standard Gibbs free energy of formation[b] between products and reactants.

$$k_{eq} = \exp(-\frac{\Delta G^0}{RT}) = \exp(-\frac{\Delta \mu^0}{k_B T}), \tag{3.3}$$

where we used in the last step $k_B = R/N_A$ and $\Delta\mu^0$ is the difference in standard chemical potential between the products and reactants. For an aggregation number of N this difference is

$$\Delta \mu^0 = N\mu_N^0 - N\mu_1^0, \tag{3.4}$$

where μ_i^0 is the chemical potential in Joules/particle for a molecule in an aggregate of size i.

[a] more strictly X_N is only identical to the solute concentration for ideal solutions; for non-ideal solutions it equals the activity.

[b] the standard Gibbs free energy of formation is defined as the change of Gibbs free energy that accompanies the formation of 1 mole of that substance (i.e. 1 mole of N-sized aggregates) from its component elements at their standard states.

Combining equations 3.2, 3.3 and 3.4 gives us for X_N

$$X_N = N\big(X_1 e^{(\mu_1^0 - \mu_N^0)/k_B T}\big)^N, \tag{3.5}$$

which together with the conservation relation for the total solute concentration C

$$C = \sum_{N=1}^{\infty} X_N \tag{3.6}$$

completely defines the system.

3.3 Conditions for self-assembly

Aggregates will form only when there is a difference in the free energies between the molecules in the aggregated and dispersed monomer states. In the case that all μ_N^0 are equal, Eq. 3.5 simplifies to

$$X_N = N X_1^N. \tag{3.7}$$

The concentrations C and X_N are expressed in dimensionless mole fraction units [$\sim M/(55.5$ Mole/l) in water, with the molarity M in Mole/l], which are all smaller than unity. The above equation therefore shows that $X_N \ll X_1$ and most molecules will be in the monomer state (N=1). Only when the Gibbs free energy in the aggregated states is *lower* than in the monomer state ($\mu_N^0 < \mu_1^0$), the occurrence of larger aggregates becomes more probable.

For all X_N to be smaller than 1, we see from Eq. 3.5 that it is a necessary condition for X_1 that

$$X_1 < e^{-(\mu_1^0 - \mu_N^0)/k_B T} \approx \text{CMC}. \tag{3.8}$$

If the total solute concentration C is increased, X_1 reaches a critical concentration above which it can increase no further. The conventional term for this concentration is the critical micelle concentration (CMC). Typical CMCs are on the order of 0.01-10 mM. Any solute added above this concentration will either aggregate in larger clusters of a finite size (N>1), or separate out into a distinct phase (N$\rightarrow\infty$).

Let us consider the special case that $\mu_N^0 = \mu_1^0$ for N$\neq$K and $\mu_K^0 < \mu_1^0$, as is the case for aggregates with a sizeable aggregation number K (this often applies to micelles, spherical aggregates of amphiphilic molecules in water). We will calculate how the monomer concentration X_1 varies with the total solute concentration C. Using Eq. 3.7 for aggregates with N$\neq$K we see that their concentrations X_N can be neglected compared to X_1, and we only need to consider X_1 and X_K. By Eq. 3.6 we have $X_K = C - X_1 \approx C$ when C $\gg$ CMC. Filling this out in Eq. 3.2 we find that

$$X_1 \simeq \text{constant} \times C^{1/K}. \tag{3.9}$$

This result shows that for large aggregation number K, the monomer concentration X_1 hardly grows with the total concentration C. Above the CMC the monomer concentration remains constant, while the concentration of aggregates increases approximately linearly with the total solute concentration C.

How μ_N^0 varies with aggregate size strongly depends on the type of solute molecule and the geometry of the aggregate. The largest (hydrophobic) part of amphiphilic molecules often consists of an alkyl tail. The chemical potentials of single solvated amphiphilic molecules and alkanes are therefore similar, while their aggregation behaviour is very different. Amphiphilic molecules tend to form micelles in water, while pure alkanes tend to phase separate from water. The important difference between alkanes and amphiphilic molecules lies not so much in their solubility or CMC values, but in the ability of amphiphiles to assemble into structures in which μ_N^0 reaches a minimum at some *finite* value of N. It is for this reason that also the aggregates are not infinite (phase separation) but of finite size (micellisation). In this terminology the formation of sheets of amphiphiles (e.g. in membrane self assembly) is also a form of phase separation.

3.4 Mixtures

Let us now discuss different mixtures of substances and consider the type of aggregation behaviour that is observed for each mixture.

Water in oil ($\mathbf{Min}(\mu_N^0) = \mu_\infty^0$)

When water is added as a solute to oil it keeps its integrity and does not mix appreciably. The free energy of the solute reaches its maximum at an infinite-sized aggregate and therefore separates out in a distinct phase. Macroscopically the absence of any mixing can be understood in terms of the large surface tension that exists between the water and the oil phase. Any attempt to mix the water and oil would strongly increase the water and oil contact surface, and thereby the surface energy. The entropic gain in free energy that would arise by mixing the water and oil does not outweigh the enthalpic loss in free energy that is associated with the increase in surface energy.

Surfactant in oil ($\mathbf{Min}(\mu_N^0) = \mu_K^0$)

Amphiphilic surfactant molecules dissolved in oils like alkanes often aggregate to form micelles. The amphiphilic molecules can lower their free energy by directing themselves away from the hydrophobic solvent to the hydrophilic head groups of other amphiphilic molecules, which results in aggregation. Spherical micelles often have a sizeable aggregation number K, dictated by constraints put by geometrical packing.

Water and surfactant in oil

Let us now consider a micellar solution of surfactant and oil to which we add a small amount of water as a second immiscible liquid. The water is transferred into the centres of the micelles, resulting in a thermodynamically stabilised dispersion of water in oil. Macroscopically the surfactant establishes a very low surface tension between the water and oil phases [77]. We do not see the formation of a single surfactant-coated water droplet in the oil phase, but the formation of many equally sized water droplets, so-called reverse micelles. Strong dispersion of the water phase is favoured because of the entropic gain in free energy that is achieved by increased mixing of the water and oil. There may also be enthalpic gains associated with mixing, since the free energy may be lowered by hydrating the hydrophillic head groups of the surfactant molecules. Also the energy associated with bending the surfactant layer is important, as will be discussed in section 3.6.

3.5 Reverse Micelles

Two parameters are used conventionally to denote the position in the phase diagram of a ternary water-oil-surfactant mixture. The size of the reverse micelles is usually proportional to the parameter w_0, which is defined as the ratio between the number of water and surfactant molecules.

$$w_0 = \frac{N_{\text{water}}}{N_{\text{surf}}}. \tag{3.10}$$

The amount of water in the system is usually expressed in terms of the water volume fraction α, defined as

$$\alpha = \frac{V_{\text{water}}}{V}, \tag{3.11}$$

where V_{water} is the added volume of water and V the total system volume.

Given the amount of surfactant, we will have a specific amount of interfacial area Σ equal to

$$\Sigma = N_{\text{surf}} \cdot a_0 = \frac{V a_0}{v_0} \frac{\alpha}{w_0}, \tag{3.12}$$

where a_0 is the average or optimal head group area taken per surfactant molecule and v_0 the effective volume of a water molecule (29.2 Å^3).

The optimal head group area is defined by two net opposing forces that we can identify between the surfactant molecules. First there is an attractive interaction from interfacial tension forces which act at the surfactant-water interface. This interaction may be represented by a positive interfacial free energy per unit area γ, which is typically 20-50 mJ m^{-2}. A second repulsive interaction is present due to steric hinderance, hydration force contributions, and an electrostatic double-layer contribution for charged surfactants. These

can be approximated to first order by a term inversely proportional to the surface area a occupied per head group. We then have

$$\left(\mu_N^0\right)_{\text{surf}} = \gamma a + B/a, \tag{3.13}$$

where B is a constant. The optimal head group area a_0 lies at the minimum of this potential at $a_0 = \sqrt{B/\gamma}$. Eliminating B in the above equation in terms a_0 we find

$$\left(\mu_N^0\right)_{\text{surf}} = 2\gamma a_0 + \frac{\gamma}{a}(a - a_0)^2. \tag{3.14}$$

For later reference it is useful to express the average micelle radius R, the number of micelles N_m and the surfactant aggregation number K in terms of the micelle water content w_0. From the surface to volume ratio of a sphere we find for the average micelle radius

$$R = \frac{3v_0}{a_0} w_0. \tag{3.15}$$

The total number of micelles N_m in the solution is found by dividing the total available interfacial area by the area of a single micelle of radius R.

$$N_m = \Sigma \,/4\pi R^2 = \frac{\Sigma a_0^2}{36\pi v_0^2} \cdot \frac{1}{w_0^2}. \tag{3.16}$$

The surfactant aggregation number K is given by

$$K = 4\pi R^2/a_0 = \frac{36\pi v_0^2}{a_0^3} \cdot w_0^2. \tag{3.17}$$

3.6 Reverse micelle stability

We will investigate what are the conditions for reverse micelles to take up water in their interiors. Let us consider the change in free energy ΔG as a result of increasing the volume of the interior water pool of the micelles. This is achieved by increasing the parameter w_0 while keeping the number of surfactant molecules and amount of apolar solvent constant (this will increase the parameter α by an equal factor). The resulting free energy change has both enthalpic and entropic contributions:

$$\Delta G = \Delta H - T\Delta S. \tag{3.18}$$

When keeping the amount of surfactant molecules constant, the total surfactant interfacial area is a constant (See Eq. 3.12). We assume the surface energy does not depend on the reverse micelle water content w_0 as soon as all surfactant headgroups are hydrated. Increasing the water content therefore does not affect the surface energy term.

A self-assembled surface of surfactant molecules usually has a preferred curvature. The curvature $c \equiv 1/R$ of the surfactant layer of a spherical micelle will in general be deformed from this spontaneous curvature c_0, which is by

definition the curvature where the energy for bending is at its minimum. The enthalpy of the surfactant layer can be described by a bending modulus κ in a harmonic approximation by

$$\left(h_N^0\right)_{\text{bend}} = 2\kappa a_0 (c - c_0)^2. \tag{3.19}$$

A surfactant layer within a reverse micelle usually has $c \gg c_0$ so that with Eq. 3.15 and Eq. 3.12 we find for the total bending enthalpy of the system

$$\begin{aligned} H_{\text{bend}}^0 &= N_{\text{surf}} \cdot \left(h_N^0\right)_{\text{bend}} \simeq 2\kappa\Sigma c^2 \\ &= A_\mu \cdot \kappa \cdot \frac{1}{w_0^2}, \end{aligned} \tag{3.20}$$

where the constant $A_\mu = 2\Sigma a_0^2/(9v_0^2)$. Another term contributing to the free energy involves the configurational entropy. By adding water the number of micelles is reduced, which reduces the degrees of freedom of the solution. Using Boltzmann's equation for the entropy[c] together with Eq. 3.16 we find

$$S_{\text{conf}} = -k_B N_m \log(\alpha) = -\frac{A_\mu}{8\pi} \log(\alpha) \cdot k_B \cdot \frac{1}{w_0^2}. \tag{3.21}$$

From this equation we see that addition of water to the micellar system decreases the configurational entropy. Although both α and w_0 increase linearly with the added water volume, since $\alpha \ll 1$, it is a good approximation in Eq. 3.21 to neglect the change in the factor $\log(\alpha)$ compared to the much larger change in the factor $\frac{1}{w_0^2}$. The total change in free energy can therefore be written as

$$\Delta G = \Delta H_{\text{bend}}^0 - T\Delta S_{\text{conf}} = A_{\Delta G} \cdot \Delta(\frac{1}{w_0^2}), \tag{3.22}$$

where $A_{\Delta G} = A_\mu(\kappa + k_B T \log(\alpha)/8\pi)$ is a near constant. As long as $A_{\Delta G}$ is positive the free energy decreases with water content. This is the case when

$$\kappa \geq -k_B T \log(\alpha)/8\pi. \tag{3.23}$$

For a typical water volume fraction $\alpha = 0.001$ this means $\kappa \geq k_B T/3.6$. The bending moduli of surfactant layers are usually much larger than the thermal energy $k_B T$, so that the reverse micelles have a strong tendency to take up water and swell.

If we continue to increase the water content of the micelles, at some point the entropic loss in free energy associated with the reduction of the number

[c] Boltzmann's equation relates the entropy to the number of microstates Ω contributing to a macroscopic state by $S = k_B \log \Omega$. We find Ω by counting the number of ways in which we can rearrange the positions of N_m micelles on N_S available sites by exchanging their volume with an equal volume of solvent elsewhere, i.e. $\Omega = \binom{N_S}{N_m}$. By using Boltzmann's equation and applying Stirling's approximation ($\log x! = x \log x - x$) we find $S \approx -k_B N_m \log \frac{N_m}{N_S}$. We now use $N_S = V_{\text{system}}/V_{\text{micelle}}$ to arrive at $S = -k_B N_m \log(\alpha)$, where α equals the water volume fraction $\alpha = N_m V_{\text{micelle}}/V_{\text{system}}$.

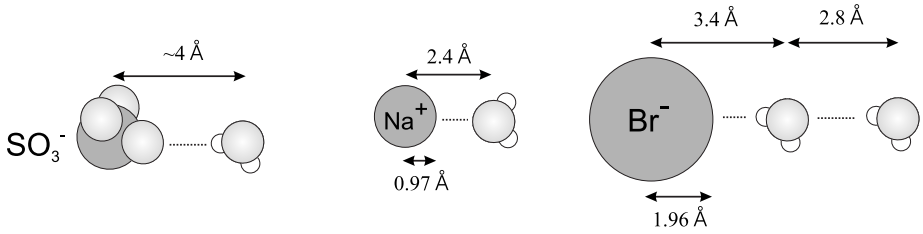

FIGURE 3.2. Ionic radii and hydrogen-bond lengths for hydrated Sulfonate [43] (the AOT anionic headgroup), Sodium, Bromine [88] and Water [74]. All dimensions are depicted to relative scale.

of micelles will start to be larger than the gain in free energy associated with relaxing the curvature of the micellar surface. This will be the case when the curvature c is no longer much larger than c_0. Then the approximation made in Eq. 3.20 breaks down, and the condition for swelling Eq. 3.23 is no longer sufficient.

Let us assume we bring into contact two solutions with equal α but different w_0. After mixing the new w_0 will be

$$w_0 = \frac{2w_{0,a}w_{0,b}}{w_{0,a} + w_{0,b}}. \tag{3.24}$$

It can be easily shown that the energy gain for making swell the smaller micelles (from $w_{0,b}$ to w_0) is much larger than the energy loss for shrinking the larger micelles (from $w_{0,a}$ to w_0). For $w_{0,a} \gg w_{0,b}$ we can show by Eq. 3.22 that $\Delta G \approx -3A_{\Delta G,b}/(4w_{0,b}^2)$, i.e. a net decrease in the free energy is achieved. This example shows that in a reverse micellar solution there is a net drive to obtain micelles of the same size.

Within the thermal energy k_BT there is freedom to vary the micellar shape and size. This gives rise to a certain degree of size polydispersity and spherical deformation for the reverse micelles.

3.7 Counter-ion concentration profile inside reverse micelles

In an ionic reverse micelle the charged lipid head groups are constrained to the outer radius of the micelle. Each lipid molecule has an associated counter-ion that is free to dissociate from the lipid (ions and surfactant groups encountered in this thesis are displayed in Fig. 3.2). The combined charge of the lipid head groups may be approximated by a net homogeneous surface charge σ, as illustrated in Fig. 3.3. From elementary electrostatics we know that the electrostatic field inside a charged sphere is zero. The head groups therefore do not contribute to the electrostatic potential inside the reverse micelle, and

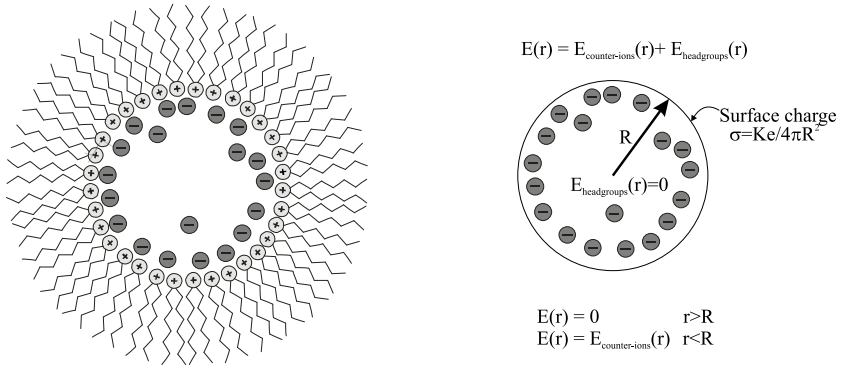

FIGURE 3.3. Schematic counter-ion distribution and static electric field inside a cationic reverse micelle.

therefore only the Coulombic repulsion between counter-ions and their entropy of mixing determine the counter-ion density profile.

In thermal equilibrium the chemical potential of the counter-ions may be written as

$$\mu(r) = ze\phi(r) + k_B T \log \rho(r), \tag{3.25}$$

where $\phi(r)$ is the electrostatic potential, $\rho(r)$ the number density of counter-ions and z the valency of the counter-ions. The first term is an enthalpic electrostatic energy, while the second term refers to entropy of mixing.

Because of the spherical symmetry of the micelle both the counter-ion density and the electrostatic potential will only depend on the distance r from the micelle centre. We may set $\phi(0) = \phi'(0) = 0$ at the centre of the micelle, where also $\rho(0) = \rho_0$. From the equilibrium requirement that the chemical potential is uniform throughout the micelle ($\mu(r) =$ constant), we find a Boltzmann distribution of counter-ions:

$$\rho(r) = \rho_0 e^{-ze\phi(r)/k_B T}. \tag{3.26}$$

The radial counter-ion density profile will be determined by the equilibrium electrostatic potential $\phi(r)$. The charge density and electrostatic potential are related according to Poisson's equation

$$\nabla^2 \phi = -\frac{ze\rho}{\epsilon\epsilon_0}, \tag{3.27}$$

where ϵ is the relative permittivity of the homogeneous medium in which the counter-ions are embedded. We will assume this medium to be water. Combining Eq. 3.26 and Eq. 3.27 gives us the Poisson-Boltzmann (PB) equation:

$$\nabla^2 \phi(r) = (-ze\rho_0/\epsilon\epsilon_0) e^{-e\phi(r)/k_B T)}. \tag{3.28}$$

The PB equation is a nonlinear differential equation that can be solved numerically. Within certain approximations[d] we can also derive an analytical solution. Using the PB equation we will derive some important characteristics of the counter-ion concentration profile inside reverse micelles. Using the fact that the total surface charge of the lipid head groups is opposite to the total charge Q of counter-ions we find

$$\begin{aligned}\sigma &= -Q/4\pi R^2 = -\frac{1}{4\pi R^2}\int_0^R ze\rho(r)4\pi r^2 dr \\ &= \frac{\epsilon\epsilon_0}{4\pi R^2}\int_0^R \frac{d^2\phi}{dr^2}4\pi r^2 dr \\ &\simeq \epsilon\epsilon_0\int_0^R \frac{d^2\phi}{dr^2}dr = \epsilon\epsilon_0 E(R),\end{aligned} \tag{3.30}$$

where we use that the electric field is given by $E(r) = \frac{d\phi(r')}{dr'}\big|_r$ which we defined to be zero at the center of the micelle. By differentiating Eq. 3.26 and substituting Eq. 3.27 we can derive a useful differential form of the PB equation, according to

$$\begin{aligned}\frac{d\rho(r)}{dr} &= -\frac{ze\rho_0}{k_BT}e^{-ze\phi/k_BT}\frac{d\phi}{dr} = \frac{\epsilon\epsilon_0}{k_BT}\frac{d\phi}{dr}\frac{d^2\phi}{dr^2} \\ &= \frac{\epsilon\epsilon_0}{2k_BT}\frac{d}{dr}E^2(r).\end{aligned} \tag{3.31}$$

By integrating this expression we find

$$\rho(r) = \rho_0 + \frac{\epsilon\epsilon_0}{2k_BT}E^2(r). \tag{3.32}$$

After substituting the result for $E(R)$ of Eq. 3.30 this equation shows that the counter-ion density at the micellar interface $\rho(R)$ depends only on the surface charge density σ and the counter-ion concentration at the center of the micelle:

$$\rho(R) \simeq \rho_0 + \sigma^2/2\epsilon\epsilon_0 k_BT. \tag{3.33}$$

More importantly the above equation illustrates that the counter-ion concentration at the interface never drops below $\sigma^2/2\epsilon\epsilon_0 k_BT$. Fig. 3.4 illustrates solutions to the PB equation for three sizes of reverse micelles. A remarkable result is that independent of the size of the micelle, the counter-ions concentrate close to the micellar surface, and very few counter-ions are found in the core of the

[d] We will approximate the Laplacian in spherical coordinates by

$$\nabla^2\phi(r) = \frac{1}{r^2}\frac{\partial}{\partial r}\Big(r^2\frac{\partial\phi(r)}{\partial r}\Big) \simeq \frac{\partial^2\phi(r)}{\partial r^2}. \tag{3.29}$$

This holds when $\phi(r)$ is small for $r \ll R$ and has primarily amplitude when $r \simeq R$; we may then replace the variable r^2 in the Laplacian by the constant R^2. The solutions we obtain will show to hold this requirement, thereby making it a valid approximation.

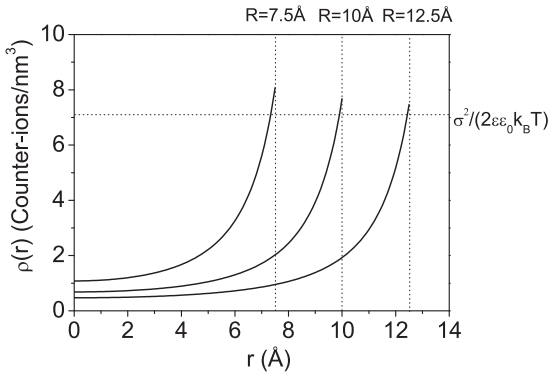

FIGURE 3.4. Solutions to the Poisson Boltzmann equation (within the approximation of Eq. 3.29) for a surface charge density σ=0.2 C m^{-2} (monovalent lipid with head group area a_0=0.8 nm^2; for AOT [137] the head group area a_0 varies from 0.3-0.6 nm^2) at 293 K, for three sizes of reverse micelles. When integrating the charge number density inwards from the surface over the first 0.2 nm, we find that a fraction of 0.5 of the total number of counter-ions is located in this thin layer, independent of the micelle radius R. This amounts to a counter-ion concentration of ∼8 M. This dense layer (approximately the width of a surfactant head group) is often referred to as the Stern layer. For lower surface charge densities σ the layer of counter-ions becomes more diffuse.

reverse micelle[e]. The counter-ions do not mix evenly over the aqueous core, which shows that the entropic free energy gain of mixing is much less important than the long-range electrostatic repulsion energy between the counter-ions. The electrostatic repulsion energy between two ions scales inversely with their relative distance. The total repulsion energy is therefore minimised when the average distance between the ions is maximised, which is achieved when the ions concentrate in the outer shell of the micelle.

Various studies have appeared describing different approaches for modelling ionic distributions at charged aqueous interfaces. The general consensus is that the interfacial region consists of a so-called Stern layer, which has about the width of the size of the surfactant head group [14, 119]. This layer contains a

[e]One has to be careful with intuitive predictions on the ion distribution in the limit of very large reverse micelles ($R \to \infty$). Since ions easily dissolve in water, there is no loss in free energy associated with the dissociation of a counter-ion–lipid headgroup ion pair. One may reason that all counter-ions will therefore be free to dissociate and distribute evenly over the aqueous core of the micelle, since this will lead to an entropic gain in free energy. This would only be true if the electrostatic repulsion energy between the counter-ions can be neglected. This is not the case in a reverse micelle. Although the average counter-ion concentration decreases inversely with the micelle radius, the number of ions increases quadratically, so that the total Coulombic repulsion energy per ion never becomes small compared to the thermal energy.

fraction of the counter-ions, the ionic head groups of the surfactant molecules and water [23]. Thermal motion creates a diffuse electrical double layer, called the Gouy-Chapman layer, which extends out into the aqueous phase and contains the remaining counter-ions [23,27,54]. The exact interplay between surfactant, its counter-ions and the nearby water will be important in understanding the structure and dynamics of the interfacial region.

Although the solutions to the PB equation give a good intuitive picture of the counter-ion density profile within a reverse micelle, there are numerous reasons why its applicability is limited. To name a few, the PB equation does not take into account attractive ion-ion-correlation effects, finite ion size (steric) effects, image forces, the discreteness of surface charges, and solvation forces. These effects become especially important when the micelles are small and the finite size of the particles becomes important. Obviously, the interactions can then no longer be described by a homogeneous model as given by the PB equation. The precise counter-ion distributions in reverse micellar systems is still not well understood and a topic of ongoing research.

Chapter 4

Inhomogeneous dynamics in confined water nanodroplets

The effect of confinement on the dynamical properties of liquid water was studied by mid-infrared ultrafast pump-probe spectroscopy on HDO:D_2O in reverse micelles. By preparing water-containing reverse micelles of different well-defined sizes, we varied the degree of geometric confinement in water nanodroplets with radii ranging from 0.2 to 4.5 nm. We find that water molecules located near the interface confining the droplet exhibit slower vibrational energy relaxation and have a different spectral absorption than those located in the droplet core. As a result, we can measure the orientational dynamics of these different types of water with high selectivity. We observe that the water molecules in the core show similar orientational dynamics as bulk water and that the water layer solvating the interface is highly immobile.

4.1 Introduction

There are many examples in the fields of biology [95, 96], geochemistry [116], tribology [16] and nanofluidics [102], where water molecules are not present as a bulk liquid, but in small numbers and confined geometries. The presence of an interface is known to influence the structure and dynamics of liquid water. By steady-state surface-sensitive techniques like x-ray diffraction it was shown that near a surface ordering of water molecules into layers occurs [28, 103, 124], which extends several molecular diameters into the liquid. In the case of small water droplets the confinement is three-dimensional, and the overall structure and dynamics of the water may be affected.

A suitable model system for studying confined water nanodroplets are reverse micelles [34, 79]. A solution of nanometre-sized droplets forms when preparing an emulsion of water in an apolar solvent by addition of a surfactant. We used the anionic lipid surfactant AOT (Sodium bis(2-ethylhexyl) sulfosuccinate, see Fig. 3.1), which is known to form micelles that are reasonably monodisperse (∼15%) [1, 112]. The size of the water droplets can be easily

varied by changing the molar water-to-AOT ratio, conventionally denoted by the parameter $w_0 = [H_2O]/[AOT]$.

An important question is whether micelle contained water can be regarded as a two-component system where the water molecules at the micellar surface show different properties from water molecules in the core of the micelles. In previous studies two-component models have been used successfully to describe both the linear absorption [49, 51] and the vibrational energy relaxation [30, 99] of confined water. As for the structural hydrogen bond rearrangements of liquid water, the effects of nanoconfinement are under much debate. So far, no inhomogeneities were observed in the molecular orientational motions of the water molecules throughout the droplets [99], while such inhomogeneities have been predicted by molecular dynamics simulations [43]. A decrease in the average mobility of water in nanodroplets has been observed by several techniques [56, 111, 122, 127], although so far no distinction could be made between water molecules at the surface layers of the droplets and those in the core. From these studies it therefore remained unclear whether the mobility of water in nanodroplets decreases overall, or that molecules located near the surface and in the core of the droplets show different dynamical behaviour. Here, we use spectrally resolved ultrafast mid-infrared pump-probe spectroscopy on the O–H stretch vibration of isotopically diluted water (HDO in D_2O) contained in reverse micelles. In these experiments we observe separately the contributions of core and interfacial water molecules, and find that the molecular mobilities are remarkably different.

4.2 Materials and Methods

Reverse micelle samples were studied with droplet radii of 0.2-4.5 nm, corresponding to clusters of 50-80,000 water molecules ($w_0 = 2, 4, 7, 12, 17, 20, 40$). These micelles were prepared by adding AOT and water at the appropriate concentrations to an apolar solvent of n-octane. We performed ultrafast mid-infrared pump-probe spectroscopy on the O–H stretch vibration of diluted HDO in D_2O. We use isotopically diluted water samples to prevent the signals to be affected by intermolecular resonant energy transfer of the O–H stretch vibrations. The transmitted probe beam is split into components polarised parallel ($\Delta\alpha_{\parallel}$) and perpendicular ($\Delta\alpha_{\perp}$) with respect to the pump polarisation, and both components are spectrally resolved simultaneously on a nitrogen-cooled HgCdTe detector array using a polychromator. We construct an isotropic absorbance change and anisotropy parameter (Eq. 1.5 and Eq. 1.6) from these polarisation components as described in chapter 1.

4.3 Results and Discussion

The structural dynamics of water can be studied through the dynamics of the O–H stretch vibrational frequencies of the molecules, because these frequencies strongly correlate with the strength of the hydrogen-bonds [78, 104]. Compared

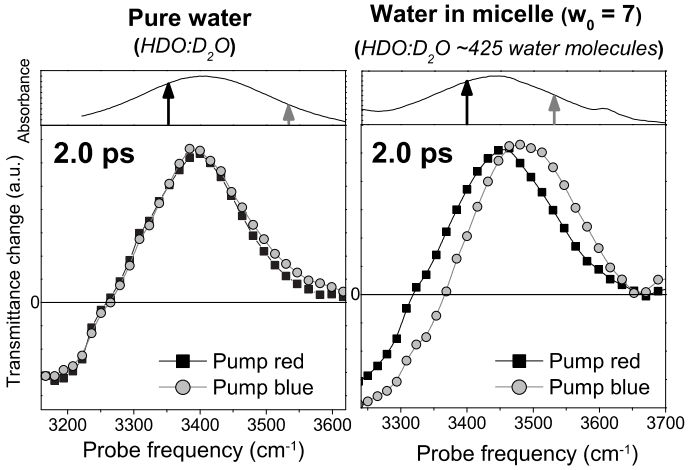

FIGURE 4.1. Comparison of the transient pump-probe spectrum at 2 ps of confined water in a reverse micelle and bulk water, when selectively pumping different spectral subsets (pump frequencies indicated by the vertical arrows in the conventional absorption spectra).

to bulk water, we find the hydrogen bond dynamics of confined water to be strikingly different. We measured the transient spectral response of both bulk water and a w_0=7 micelle ($n_{water} \approx 425$) when pumping at the blue wing of the O–H stretch spectrum (mainly exciting weakly hydrogen-bonded molecules), and at the red wing (mainly exciting strongly hydrogen-bonded molecules). The pump-induced transmission changes at 2 ps time-delay are shown in Fig. 4.1.

From the left panel of Fig. 4.1 we see that for bulk water, irrespective of which subset of water molecules was initially excited, the pump-probe spectra become identical very rapidly (within 1 ps). This fast spectral diffusion shows that rapid fluctuations within the hydrogen bond network cause a fast interconversion of strong and weak hydrogen bonds [52, 92]. As a result, the excited subset of molecules quickly reaches its spectral equilibrium distribution. This sharply contrasts with the case of water confined in a nanodroplet, as shown in the right panel of Fig. 4.1. Here, the pump-probe spectra obtained with different pump frequencies remain shifted with respect to each other, even at long delays (>10 ps). The confined liquid apparently contains spectrally separated subsets of OH oscillators that do not interchange their absorption frequencies on a picosecond timescale, which suggests that water molecules within the nanodroplets experience different local hydrogen bonding over long time scales.

The observed inhomogeneity in the dynamics of the confined water molecules can be further investigated by studying their vibrational relaxation, which is known to depend strongly on the local hydrogen bonding [78]. In studies on neat (not isotopically diluted) water, it is shown that the vibrational relaxation rate increases with micelle size [30, 37] (see chapter 6). This work can however

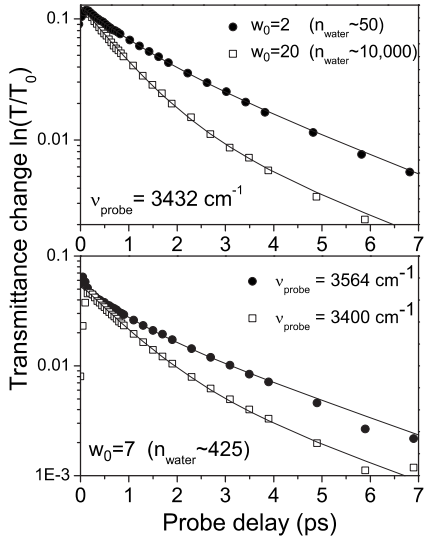

FIGURE 4.2. Pump-induced transmission change at the O–H stretch absorption, plotted as a function of probe delay for two droplet sizes at a single probe frequency (top panel) and at different probe frequencies for a single droplet size (bottom panel). The pump wavelength was kept constant at 3480 cm^{-1}.

only reveal the average dynamics of the water molecules, because of the rapid intermolecular energy transfer occurring in neat H_2O [29,37]. Fig. 4.2 shows the vibrational relaxation measured for isotopically diluted water in nanodroplets. The decay is clearly multi-exponential (as opposed to bulk HDO in D_2O) and dependent on micelle size. We find from a global fit to all delay curves of measurements on 7 samples of different micelle sizes (32 probe frequencies / sample), that the dynamics can be well described by a model of two components with different vibrational relaxation time-constants T_1. Although we observe a slight frequency dependence in the relaxation rate of the slow component, we did not include this frequency dependence to limit the number of fit-parameters. In the fit, the relative amplitudes of each component is allowed to vary both with absorption frequency and size of the reverse micelle. Fig. 4.3 shows the obtained spectral amplitudes for two sizes of micelles. The blue-shifted component has T_1=2.8 ps for all droplet sizes. For the red-shifted component T_1 decreases from 1.0 ps for the smallest droplet to 0.7 ps for the largest droplet. The obtained results for the fit parameters are give in Table 4.1 of the Appendix.

As we lower the surface-to-volume ratio of the water droplets by increasing their size, the amplitude of the slow component in the vibrational relaxation strongly decreases, as illustrated in the top right panel of Fig. 4.3. For micelles having $w_0 > 10$ we find a decrease of the relative fraction of the slow component f_{slow} consistent with a $1/w_0$ dependence ($\propto w_0^{-\alpha}$, $\alpha = 0.85 \pm 0.25$). Since the micelle radius varies linearly with w_0 in this size regime [112], the fraction of the

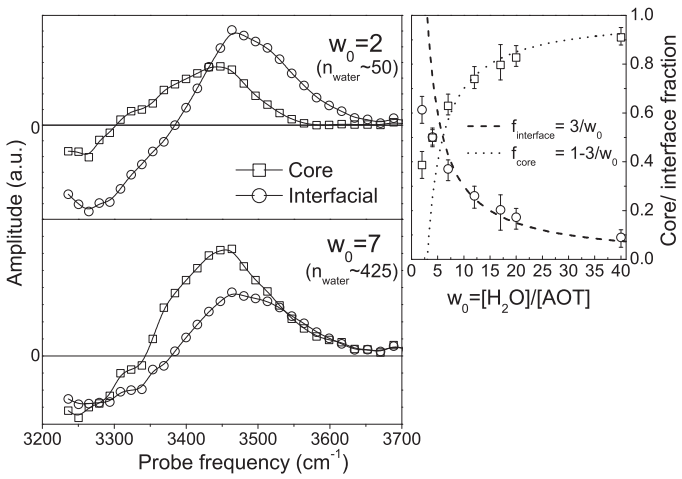

FIGURE 4.3. Spectral amplitudes of the core (fast) and interfacial (slow) components in the vibrational relaxation for water in two sizes of reverse micelles, obtained from a global fit to the data. The top right panel shows the relative core and interfacial fractions, which are obtained by spectrally integrating the positive (bleaching) part of the spectrum for each of the two components. Error bars are put at those fractions where the χ^2-value of the global fit doubles its minimised value (keeping the interfacial vibrational lifetime fixed). In the Appendix we give the spectral amplitudes for core and interfacial components of all studied samples (Fig. 4.5).

slow component is in fact inversely proportional to the radius of the droplet, just like the surface-to-volume ratio of a sphere. This strongly suggests that the slow component is associated with water molecules at the droplet interface. Assuming a dependence of the slow-component proportional to $1/w_0$, we find a prefactor to this term of 3.3 ± 0.3. If we neglect differences in the absorption cross-section of the core and interfacial molecules, this factor suggests a surface coordination of 6-7 hydrogen-bonds per surfactant molecule. This number of hydrogen bonds is consistent with the fact that there are the six lone electron pairs located at the oxygens of the sulfonate anion of the AOT surfactant molecule, which can accept one hydrogen bond each. We thus assign the slow component to interfacial water and the fast component to core water.

For the smaller micelles ($w_0 < 10$) we observe that the amplitude of the interfacial component does not follow a $1/w_0$ proportionality, but increases more slowly with decreasing w_0. This deviation is also found in molecular dynamics simulations [43]. In fact, for all micelles studied, the dependence on w_0 of the interfacial component agrees well with the calculated number of molecules

within the first solvation layer of the micelle cavity [a]. The simulations show that for the smallest micelles the interface is strongly curved, the surfactant molecules are less hydrated and pack more closely. Therefore the density of water molecules located at the interface decreases, explaining the deviation from the approximate $3/w_0$-dependence for the smaller micelles ($w_0 < 10$).

The spectrum of the interfacial component is blue-shifted with respect to the core component, as seen in Fig. 4.3, which points to a weakening of the hydrogen bonds of these molecules [37]. The OH$\cdots$O hydrogen bond is known to weaken if it is not parallel to the OH-bond [104, 126], and this configuration is likely to occur at a micellar interface. The local binding structure of the interfacial water depends on the hydrophilic interactions with the surfactant molecules and their counter-ions [57], and on packing constraints. The near-tetrahedral hydrogen-bond network that exists for bulk water will be disrupted at the interface, and non-directional and possibly bifurcated hydrogen bonds may form here.

The core water molecules have an average hydrogen-bonding that is slightly weaker compared to bulk water, as can be concluded from the missing red wing in the spectrum of the core component. This red wing recovers in going from w_0=12 to 40 and the vibrational relaxation rate approaches the bulk value only at about w_0=40. Therefore, water with full bulk-like character only starts to appear in a cluster of at least 2000 water molecules (w_0=12) and bulk-like molecules fully dominate the dynamics over molecules with interfacial character at clusters larger than 80,000 molecules (w_0=40). Note that the sodium counter-ions of the AOT surfactant molecules are not expected to have a large influence on the dynamics of the core component, since they mainly associate with the anionic head groups and are only partly solvated [57] (see also chapter 3.7). In addition, it is has been found that the effect of sodium cations on the dynamics of bulk water is very small [94].

In order to obtain information on the molecular motions of the core and interfacial water, we measured the decay of the anisotropy in the orientation of the pump-excited OH-groups. Preferentially O–H stretch oscillators parallel to the pump polarisation will absorb, causing different transmissions for probe light polarised parallel and perpendicular to the pump polarisation. The decay of the relative difference of these two signals gives direct information on the angular motions of the OH-groups of the water molecules.

Fig. 4.4 shows four anisotropy decay curves for different absorption frequencies and two different micelle sizes (anisotropy decay curves for all studied samples are displayed in Fig. 4.6 in the Appendix). When the interfacial component dominates, which is the case at the blue absorption frequencies of especially the smallest nanodroplets, the anisotropy parameter decays very slowly over time scales larger than 20 ps. The water layer solvating the interface is apparently highly immobile, despite the fact that these molecules are more weakly hydro-

[a] Faeder et al. define the interfacial fraction as those molecules located within 0.5 nm distance from the reverse micelle cavity boundary. The present work shows the same micelle size-dependence for this fraction, but by an absolute fraction 20 percent lower, likely because it does not include any OH-groups forming hydrogen bonds to other water molecules.

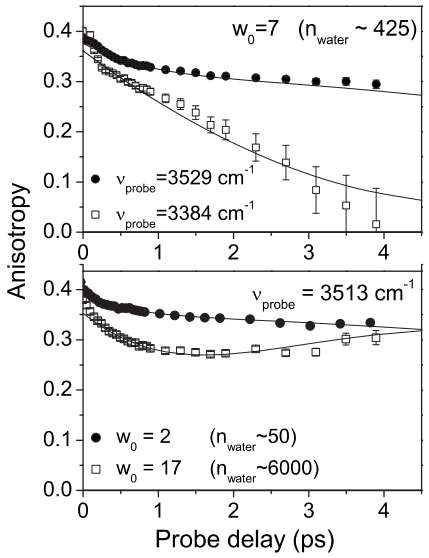

FIGURE 4.4. Comparison of the anisotropy decay of the O–H stretch vibration at two different probe frequencies for an intermediate size micelle of w_0=7 (top panel), and a comparison of the orientational relaxation for two different reverse micelles sizes (w_0=2,17) at a single probe wavelength of 3513 cm^{-1} (bottom panel).

gen bonded than those located in the micelle centre. At frequencies where the core component dominates, the anisotropy decays rapidly on a time scale of a few picoseconds. This is for example the case for the decay curve shown in Fig. 4.4 for a w_0=7 micelle at 3384 cm^{-1}, which is the absorption frequency at the zero-crossing of the pump-probe signal of the interfacial water molecules (see Fig. 4.3).

A quite peculiar anisotropy decay can be observed at frequencies where we find both core and interfacial water, as illustrated by the decay curve for the w_0=17 micelle in Fig. 4.4 Directly after excitation we observe an anisotropy decay with an associated time constant close to that of bulk water, but the decay quickly levels off and even rises from about 2 ps onwards. This effect can be understood in terms of the different vibrational relaxation time-constants associated with core and interfacial water. Since only excited molecules contribute to the observed anisotropy and the vibrations of the interfacial water decay more slowly, the relative contribution of interfacial water to the signal will increase in time. As time progresses the anisotropy parameter increasingly reflects the slowly decaying anisotropy of the interfacial molecules. This explains the recovery of the value of the anisotropy parameter at later delays.

The observed anisotropy curves can be well described by a model in which the previously determined core and interfacial water fractions have different reorientational time-constants τ, as shown by the curves in Fig. 4.4 obtained from

a global fit. We find that the core water reorients on a time scale close to that of bulk water [48, 92] ($\tau_{\text{core}} = 2 - 4$ ps), while the interfacial water is immobile on our experimentally accessible time scales ($\tau_{\text{interface}} > 15$ ps).

In recent anisotropy relaxation measurements on the OD hydroxyl stretch of water by Piletic et al. it was also found that the orientational mobility of the molecules strongly changes when the micelle size decreases [99, 122]. The authors of this work however do not observe an inhomogeneity in the orientational relaxation throughout the droplet, and conclude that the hydrogen bond structural rearrangements of confined water are best described within a framework in which all molecules are treated equivalently. These conclusions contrast our observations presented above. A possible reason that the orientational motions of the two sorts of water can be distinguished in this study is the experimental advantage that we measure the dynamics spectrally resolved over the entire frequency range of the O–H stretch absorption band. The competition between the core and interfacial contributions to the anisotropy is most obvious in larger micelles at relatively blue absorption frequencies. In these cases one can observe most clearly the transition from a case in which the anisotropy is dominated by a large amount of core molecules, to a case in which the interfacial molecules dominate at later delays in view of their longer vibrational lifetime and blue absorption frequency (see Fig. 4.4). In addition, the OH band is more strongly inhomogeneously broadened than the OD band, which allows for a better spectral distinction of different species, i.e. the water in the core and at the interface of the micelle.

The observation of slow orientational dynamics for the interfacial water molecules is supported by recent molecular dynamics simulations on micellar systems [9, 43]. These studies have suggested that water molecules can remain bound to micellar surfaces for more than 100 ps. Other calculations show that the ionic-dipole interaction between the surfactant and its solvating water molecules is strong [35], leading to a local ordering and density increase of water molecules close to the surfactant molecules [43]. Also the sodium counter-ions, which mainly associate with the sulfonate anionic head groups at the interface, will influence the dynamical properties of neighbouring water [57].

Core and interfacial water molecules show strongly different orientational mobilities, which has to be explained from their different intermolecular interactions and very different geometric arrangements. Molecular reorientation involves the subsequent breaking and formation of hydrogen bonds. Interestingly, the activation energy for this process is not the same as the hydrogen bond binding energy, as is apparent from the fact that interfacial water has a smaller hydrogen bond binding energy, yet shows a slower molecular reorientation. For core water molecules (as for bulk water) the activation energy for reorientation is substantially lowered, because these molecules can break a hydrogen bond while simultaneously forming a new bond with another water molecule [74]. For interfacial water this process appears to be sterically hindered because these molecules are hydrogen bonded to a heavy immobile surfactant molecule. Because of this geometric effect, weakly hydrogen bonded molecules can experience a slow reorientation and slow hydrogen bond dynamics, even

though their hydrogen bond binding energy is relatively small.

In conclusion, we studied the vibrational and rotational dynamics of water molecules contained in water nanodroplets using femtosecond transient vibrational spectroscopy. We find that we can distinguish core and interfacial water on the basis of their different vibrational lifetimes. The orientational motions of the water molecules turn out to be strongly inhomogeneous in the droplet. Even for small micelles, the water molecules in the core reorient on a similar time-scale as bulk liquid water. Therefore, nano-confinement has a negligible effect on the orientational mobility of water molecules in the core of the droplets. We find the water at the interface to be highly immobile, in spite of the fact that their hydrogen bonding is weaker compared to molecules in the core of the droplets.

4.4 Appendix

4.4.1 Kinetic Modeling

In describing the vibrational relaxation, we perform a global fit to the delay curves of the rotation free signal of measurements on seven samples of different micelle sizes (32 probe frequencies/sample). The dynamics is well described by a model of two components with different time-constants. The slow component, assigned to interfacial water molecules, is assumed to have an associated vibrational relaxation time constant that is equal for all sizes of micelles. The fast component, assigned to core water molecules, may vary its time constant with micelle size. We thus separate the rotation free signal into two contributions from core and interfacial OH-oscillators:

$$\begin{aligned} \Delta\alpha_{\mathrm{RF}}(\omega,t) &= \Delta\alpha_{\mathrm{RF,core}}(\omega,t) + \Delta\alpha_{\mathrm{RF,interface}}(\omega,t), \\ \Delta\alpha_{\mathrm{RF,core}}(\omega,t) &= \sigma_{\mathrm{PP,core}}(\omega)\ e^{-t/T_{\mathrm{core}}}\ , \\ \Delta\alpha_{\mathrm{RF,interface}}(\omega,t) &= \sigma_{\mathrm{PP,interface}}(\omega)\ e^{-t/T_{\mathrm{interface}}}. \end{aligned} \tag{4.1}$$

Because of heating of the sample caused by the intense pump pulse, we measure a small thermal signal (0.1-5 percent of the total transmission change, depending on frequency and micelle size) in the pump-induced absorbance changes. This signal is modelled to grow in at the vibrational relaxation rate to the level of absorption change that is measured at ∼10 times the average vibrational relaxation time constant for each micelle (i.e. at 20, 15, 12, 10, 10, 9, 9 ps for w_0=2, 4, 7, 12, 17, 20, 40, resp.) At these delay times the population induced transmission changes are negligible and only the thermal signal is present. The thermal signal is subsequently subtracted from the original signals $\Delta\alpha_{RF}$, $\Delta\alpha_{\parallel}$ and $\Delta\alpha_{\perp}$. We do not take into account the slow decay of the thermal signal due to cooling of the micelle to its surroundings [112]. For this approximation to be valid, we performed experiments on highly diluted samples of HDO in D_2O (H_2O:D_2O=1:40). In this case the heating of the micelles is very limited and the subsequent cooling very slow, making the thermal signal effectively constant

TABLE 4.1. O–H stretch vibrational lifetimes (in ps), fractions, and reorientational time-constants (in ps) of core and interfacial water.

w_0	n_{water}	$T_{1,\text{core}}$	$T_{1,\text{interf.}}$	f_{core}	$f_{\text{interf.}}$	τ_{core}	$\tau_{\text{interf.}}$
2	50	1.0±0.2	2.8±0.2	0.39	0.61	3±1	>20
4	150	0.9±0.2	2.8±0.2	0.50	0.50	3±1	>15
7	425	0.9±0.2	2.8±0.2	0.63	0.37	3±1	>15
12	2150	0.9±0.1	2.8±0.2	0.74	0.26	3±1	>15
17	6200	0.9±0.1	2.8±0.2	0.8	0.20	3±1	>15
20	10,000	0.8±0.1	2.8±0.2	0.83	0.17	3±1	>15
40	80,000	0.8±0.1	2.8±0.2	0.91	0.09	3±1	>15
bulk	∞	0.7±0.1	-	1	0	3±0.5	-

The vibrational lifetime of the interfacial water was a global fit parameter. The bulk vibration relaxation and reorientation time constant for HDO in D_2O were taken from reference [106].

over the time-window considered; subtracting the thermal signal at 15 times the average vibrational relaxation time instead of 10 did not lead to any significant change of the fit parameters. Note that the parallel and perpendicular signals experience the same thermal effect since rapid heat diffusion makes heating highly isotropic.

In the fit, the relative amplitudes $\sigma_{\text{PP,core}}$ and $\sigma_{\text{PP,interface}}$ may vary both with probe absorption frequency and size of the reverse micelle. Fig. 4.5 shows the obtained spectral amplitudes for all considered sizes of micelles. Table 4.1 lists the obtained time constants.

The orientational relaxation can be well described by assuming different anisotropy decays for the previously determined core and interfacial water fractions. By use of Eq. 4.1 we can write for the anisotropy parameter (analogous to Eq. 1.11):

$$R(\omega,t) = f_{\text{core}}(\omega,t)R_{\text{core}}(t) + f_{\text{interface}}(\omega,t)R_{\text{interface}}(t), \qquad (4.2)$$

$$f_{\text{core}}(\omega,t) = \frac{\Delta\alpha_{\text{RF,core}}(\omega,t)}{\Delta\alpha_{\text{RF}}(\omega,t)}, \quad f_{\text{interface}}(\omega,t) = \frac{\Delta\alpha_{\text{RF,interface}}(\omega,t)}{\Delta\alpha_{\text{RF}}(\omega,t)}.$$

The time-dependent fractions f_{core} and $f_{\text{interface}}$ are obtained from the fit to the rotation free signal. $R_{\text{core}}(t)$ and $R_{\text{interface}}(t)$ are the anisotropy parameters for the core and interfacial water sub-ensembles, which we assume to show an exponential decay. These two reorientational time constants are obtained from a global fit to the anisotropy curves at all spectral frequencies for each micelle size. The core water is found to reorient on a timescale of 2-4 ps, similar to bulk water. The reorientational time constant of the interfacial water is >15 ps. Fig. 4.6 shows the orientational relaxation for six different sizes of nanodroplets at two probe absorption frequencies each.

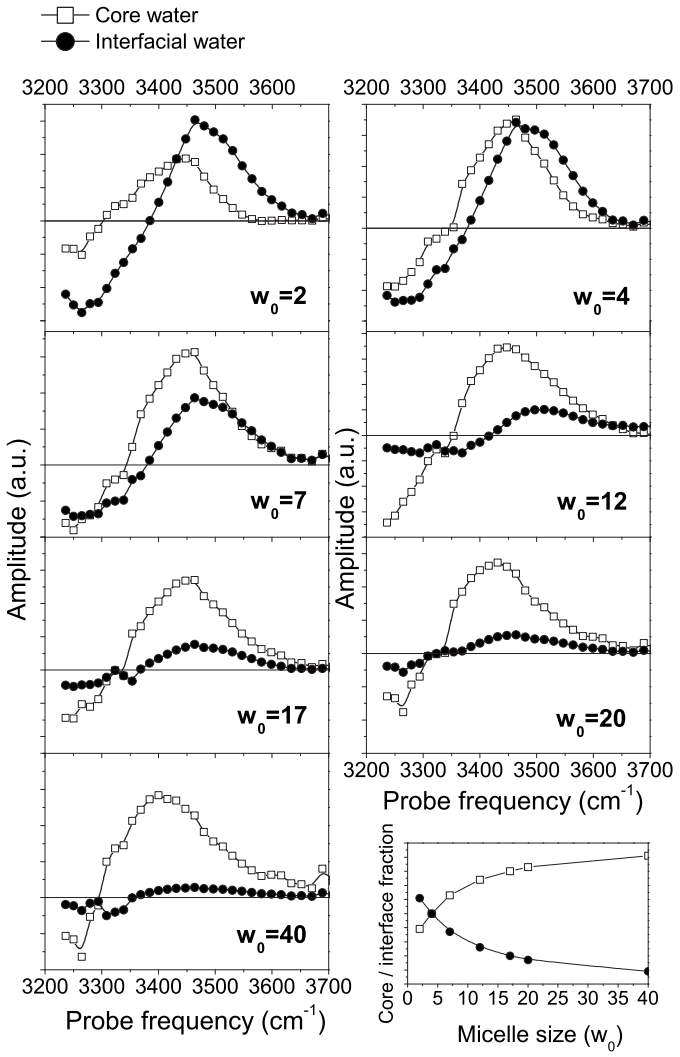

FIGURE 4.5. Spectral amplitudes of the core (fast) and interfacial (slow) components in the vibrational relaxation for all studied sizes of reverse micelles, obtained from a global fit to the vibrational relaxation curves, obtained by measuring the rotation free pump-probe signal $\Delta\alpha_{RF}$. The bottom right panel shows the relative core and interfacial fractions, which are obtained by spectrally integrating the positive (bleaching) part of the spectrum for each of the two components (see Table 4.1).

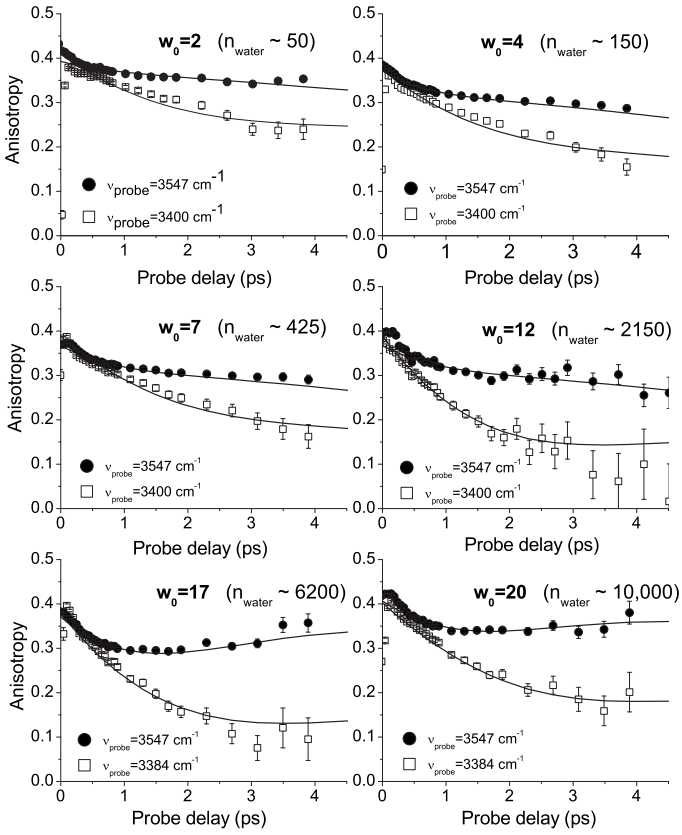

FIGURE 4.6. Orientational relaxation of the O–H stretch vibration of water in different sizes of reverse micelles. For six samples of different w_0 we compare the anisotropy decay at 3550 and 3390 cm^{-1}.

Chapter 5

Ultrafast dynamics of water in cationic micelles

The effect of confinement on the dynamical properties of liquid water is investigated for water enclosed in cationic reverse micelles. We performed mid-infrared ultrafast pump-probe spectroscopy on the O–H stretch vibration of isotopically diluted HDO in D_2O in CTAB reverse micelles of various sizes. We observe that the surfactant counterions are inhomogenously distributed throughout the reverse micelle, and that regions of extreme salinity occur near the interfacial Stern layer. We find that the water molecules in the core of the micelles show similar orientational dynamics as bulk water, and that water molecules in the counterion-rich interfacial region are much less mobile. An explicit comparison is made with the dynamics of water confined in anionic AOT reverse micelles.

5.1 Introduction

The development of ultrafast optical techniques has enabled studies on water dynamics in which the time-scales of molecular motions and vibrational relaxation can be resolved. Several ultrafast experiments were recently reported in literature, aimed at a better understanding of the ultrafast dynamics of strongly confined water [30, 34, 37, 38, 46, 99, 109, 111, 112, 122]. Almost all studies have focussed on micellar systems containing the anionic surfactant AOT (Sodium bis(2-ethylhexyl) sulfosuccinate). This system has been well characterised and is known to form mono-disperse reverse micelles in a wide range of sizes. Because specific interface-water interactions are expected to be very important in explaining the different behaviour of interfacial water compared to bulk water, it is interesting to see how other surfactants than AOT affect water dynamics within reverse micelles. The work presented in this chapter aims at studying ultrafast water dynamics confined in cationic micelles using the surfactant salt CTAB (cetyltrimethylammonium bromide). We will explicitly compare these results to earlier results obtained for anionic reverse micelle systems, in partic-

ular AOT reverse micelles.

5.2 Materials and Methods

CTAB is one of the most widely used surfactant salts for making cationic reverse micelles. The microstructure of CTAB reverse micelles has been relatively well investigated by Time-Resolved Fluorescence Quenching (TRFQ), Dynamic Light Scattering (DLS) and Conductivity and Self-Diffusion Measurements [32, 53, 75]. In all studies, the water content of the micelles was shown to increase monotonically with the parameter w_0=[water]/[CTAB].

We used both surfactant salt CTAB and CTAC in preparing cationic micelles. For CTAB, a hexadecyltrimethylammonium cation (CTA^+) acts as the surfactant molecule, of which the hexadecyl group points towards the apolar solvent and the ammonium group towards the water pool. Bromide anions (Br^-) are present as the surfactant counter-ions. The surfactant salt CTAC consists of the same CTA^+ cation, however the bromide ions have been exchanged for chloride ions. Dichloromethane was used as the apolar solvent. The micelle water content for these mixtures can be varied from w_0=2–8 for CTAB and from w_0=1–4 for CTAC. At lower water content the surfactant salt will not dissolve and at higher water content phase separation takes place into a turbid phase (the introduction of a co-surfactant can extend the region in which thermodynamically stable reverse micelles form [31, 32, 53], but since co-surfactants usually contain hydroxyl groups of which the vibrational absorptions spectrally overlap with those of the studied water, their use is not desirable in this study). We also studied larger reverse micelles at an elevated temperature of 315K, using a 1:2 mixture of isooctane and chloroform as a solvent [75]. For this quaternary mixture, the radius of the water pool was found to increase almost linearly with w_0=[water]/[CTAB], according to $r = 2.1 \times w_0$ for $w_0 > 10$, as shown by TRFQ experiments [75].

CTAB and CTAC surfactant salts and apolar solvents were obtained from Aldrich and used without further purification. CTAB micelles in dichloromethane were prepared for w_0=2,4 and 8. CTAC micelles were prepared for w_0=1,2 and 4. We used a sample cell of 1 mm optical path-length, and the water volume fraction was kept at 1%. CTAB micelles in 1:2 mixtures of isooctane and chloroform were prepared for w_0=15,30. These samples were studied using a variable-temperature cell of 500μm optical path-length at 315K. The water volume fraction for these samples was 3%. All micelle samples contained isotopically diluted water in a volume ratio of 1:30 of H_2O and D_2O. The protons and deuterons of the water molecules will exchange almost instantaneously to form a system of diluted HDO in D_2O. Bulk halogenic solutions of NaBr (Aldrich, SigmaUltra grade) of molality 2 and 6 were studied using a cell of 200 μm optical path-length, using a 1:500 isotopic mixture of H_2O and D_2O.

We performed ultrafast mid-infrared pump-probe spectroscopy on the O–H stretch vibration of diluted HDO in D_2O confined in the cationic micelles. Iso-

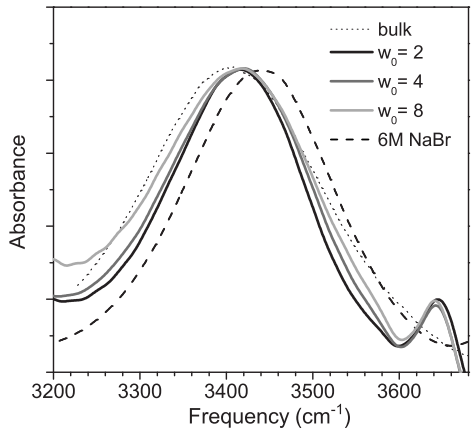

FIGURE 5.1. The O–H stretch absorption of liquid HDO:D_2O in CTAB micelles of various sizes, after subtraction of the CH_2Cl_2 solvent background. The 6M NaBr spectrum is an absorption spectrum for a solution of NaBr in 1:500 H_2O:D_2O of Molality 6. The bulk spectrum is an absorption spectrum for 1:1000 H_2O:D_2O.

topically diluted water samples are used to prevent the signals to be affected by intermolecular resonant energy transfer of the O–H stretch vibrations, and to limit heating of the sample. Pump-induced transmission changes are recorded consecutively for both the probe component polarised parallel ($\Delta\alpha_{\parallel}$) and perpendicular ($\Delta\alpha_{\perp}$) with respect to the pump polarisation. The two polarisation components are used to construct the rotation-free signal $\Delta\alpha_{\mathrm{RF}}(\omega, t)$ and the anisotropy parameter $R(\omega, t)$ (depending both on the probe frequency ω and the probe time delay t) (See Eq. 1.5 and Eq. 1.6 in chapter 1).

5.3 Results and Discussion

5.3.1 Linear Absorption

The O–H stretch absorption spectra of water in CTAB reverse micelles of three different sizes, are shown in Fig. 5.1. Since CTAB micelles contain bromide counterions, we compare these spectra with a 6M NaBr bulk solution, which contains about the same concentration of bromide ions as a w_0=8 CTAB reverse micelle. Anions are known to have an effect on the O–H stretch absorption spectrum of water [12]. Water in the hydration shell of the bromide ion has an absorption centred at 3475±11 cm^{-1}, which is blue-shifted with respect to the bulk water absorption centred at 3410 cm^{-1}.

The O–H stretch absorption of water in CTAB micelles peaks near 3415 cm^{-1} for all sizes of micelles (a smaller absorption is observed near

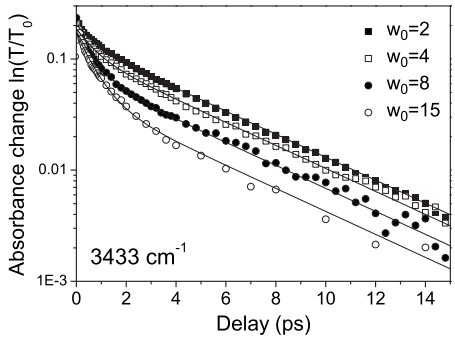

FIGURE 5.2. Pump induced absorbance change plotted as a function of probe delay at 3443 cm^{-1}at various micelle sizes. The vibrational relaxation has bi-exponential character. The absorbance change is defined as $\ln(T/T_0)$ where T is the time-dependent transmittance after excitation by the pump, and T_0 the time-independent transmittance in the absence of pump excitation.

3650 cm^{-1}, which arises from small amounts of HDO dissolved in the dichloromethane solvent). Quite remarkably, only a narrowing of the O–H stretch absorption spectrum is observed with respect to bulk water, and no blue-shift due to the bromide counterions. This indicates that the hydration shell of the bromide ion has different properties in reverse micelles than in bulk water.

5.3.2 Vibrational relaxation

Distinguishing anion-bound and bulk-like water by T_1

Fig. 5.2 shows the rotation free signal recorded for 4 sizes of micelles at a single absorption frequency in the O–H stretch band. The vibrational relaxation contains a short- and a long-lived component, the short-lived component becoming more pronounced with increasing micelle size. After 3 ps the dynamics becomes dominated by the slower decay, and we will discuss these dynamics first.

The slower vibrational relaxation component has an associated exponential T_1 time-constant of >4 ps. Vibrational relaxation on such a long time-scale does not occur in bulk HDO:D_2O. To identify what causes this slower decay, we performed measurements on the same micellar system as CTAB, but with the bromide counter-ions exchanged for chloride ions. This can be accomplished by preparing micelles using the surfactant salt CTAC instead of CTAB. Fig. 5.3 compares the transient absorption change for the O–H stretch vibration of water in CTAC and CTAB reverse micelles of equal size (w_0=2). Clearly, the vibrational relaxation of water in CTAC micelles is faster than in CTAB mi-

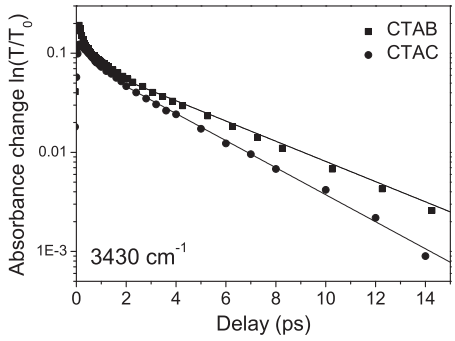

FIGURE 5.3. Pump induced absorbance change plotted as a function of probe delay at 3430 cm^{-1}, comparing CTAB (■), and CTAC (●) micelles of w_0=2. The slower component in the vibrational relaxation is associated with the surfactant counter-ion, which is bromide for CTAB and chloride for CTAC. Water in the first solvation shell of chloride has a faster vibrational relaxation than the solvation shell water of bromide [69].

celles. Studies on bulk ionic solutions have shown a similar dependence of the vibrational relaxation on the nature of the halogenic anion [68]. In these studies it was found that water coordinating chloride ions shows a significantly faster vibrational relaxation than water coordinating bromide ions, just as we observe for water in CTAC and CTAB micelles. Therefore we assign the long-lived component to water solvating the surfactant counter-ions.

From Fig. 5.2 we see that within the first 3 ps an initial fast vibrational decay is observed in the transient absorption change. To determine its time-constant, we describe the rotation free signal at each frequency with a fast and a slow contribution. We also measure small absorption changes due to heating of the sample by the intense pump-pulse. In a kinetic model we account for the precise dynamics of this thermal signal $\Delta\alpha_{\mathrm{T}}$, which is subtracted from the measured parallel and perpendicular transmission changes to obtain the pure pump-probe signals $\Delta\alpha_{\parallel}(\omega,t)$ and $\Delta\alpha_{\perp}(\omega,t)$ (see Appendix). We describe the rotation-free signal at each frequency with a fast and a slow contribution:

$$\begin{aligned} \Delta\alpha_{\mathrm{RF}}(\omega,t) &= \Delta\alpha_{\mathrm{RF,fast}}(\omega,t) + \Delta\alpha_{\mathrm{RF,slow}}(\omega,t), \\ \Delta\alpha_{\mathrm{RF,fast}}(\omega,t) &= \sigma_{\mathrm{PP,fast}}(\omega)\ e^{-t/T_{\mathrm{fast}}}, \\ \Delta\alpha_{\mathrm{RF,slow}}(\omega,t) &= \sigma_{\mathrm{PP,slow}}(\omega)\ e^{-t/T_{\mathrm{slow}}}. \end{aligned} \tag{5.1}$$

We find a fast component of 0.7±0.2 ps and a slower anion solvation shell component of 4.1±0.2 ps (3.4±0.2 ps for CTAC) for all sizes of micelle. The obtained spectra $\sigma_{\mathrm{PP,fast}}(\omega)$ and $\sigma_{\mathrm{PP,slow}}(\omega)$ are shown in Fig. 5.4. The time-scale of the fast component is very similar to the vibrational relaxation rate

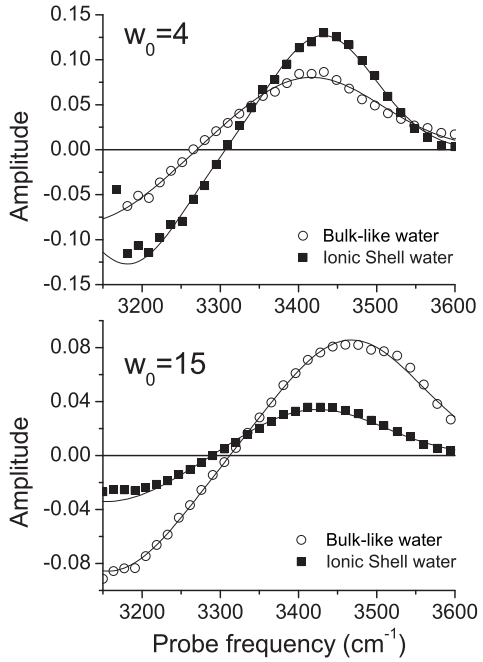

FIGURE 5.4. Spectral pump-probe amplitudes for anion-bound and bulk-like OH-groups as a function of probe frequency ω. Following the definitions in eq. 5.1, the bulk-like water spectrum (■) equals $\sigma_{\mathrm{PP,fast}}(\omega)$ and the anion-bound water spectrum (○) equals $\sigma_{\mathrm{PP,slow}}(\omega)$.

observed for bulk HDO:D_2O, indicating that this component corresponds to OH-oscillators hydrogen-bonded to other water molecules. The relative fraction of the fast component increases as we increase the size of the micelle, as displayed in Fig. 5.5. This trend can be well understood, since larger micelles contain less bromide ions, and therefore more water outside the bromide solvation shells.

Absorption line shapes anion-bound and bulk-like water

For each micelle both the spectrum $\sigma_{\mathrm{PP,slow}}(\omega)$ and $\sigma_{\mathrm{PP,fast}}(\omega)$ were fitted using two gaussian line shapes, one positive gaussian of centre frequency ν and width Δ to represent the $\nu_{OH} = 0 \rightarrow 1$ bleaching part of the pump-probe spectrum, and one negative gaussian of equal shape but red-shifted in frequency by an anharmonicity α, to represent the $\nu_{OH} = 1 \rightarrow 2$ induced absorption. The line shape parameters are listed in Table 5.2. In Fig. 5.6 the obtained absorption line shapes are shown for two sizes of micelles and for a 6 M NaBr solution.

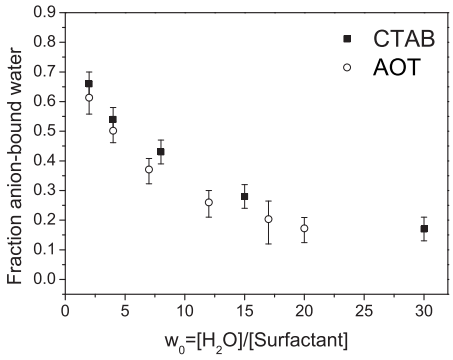

FIGURE 5.5. Relative fraction anion-bound water A_{anion} (see Tab. 5.2) obtained by spectrally integrating the peak areas of bulk-like and anion-bound water (see Fig. 5.6). For comparison, the interfacial water fractions for anionic AOT micelles (see chapter 4) are shown as well.

As seen from the right panel in Fig. 5.6, the hydration shell of Br^- absorbs more to the red in CTAB micelles than in bulk water. This may result from a different solvating structure of bromide ions in micelles. The absorption line shape for bulk-like water in micelles is also different compared to bulk water. For micelles of $w_0 \geq 8$, the bulk-like water shows a blue-shifted absorption. This points to weakened hydrogen-bonding in the core of the micelles, as observed earlier for water in anionic micelles in the previous chapter [38]. For the smallest micelles (w_0=2,4) the bulk-like water absorption is also slightly blue-shifted with respect to bulk-water, however much less than for the larger micelles. The water molecules corresponding to this absorption likely coordinate the cationic head groups of the CTA^+ surfactant, resulting in an increase of the hydrogen-bonding to other water molecules. As a result, the absorption is less blue-shifted than that of water molecules in the core of larger micelles.

Inhomogeneous distribution of counter-ions

For bulk ionic solutions it was found that the relaxation rate of anion-bound water increases with anion concentration [69]. Using these previous results as a reference, we can use the measured vibrational relaxation rates in the reverse micelles to determine the local concentration of bromide ions. The relaxation of anion-bound water in the micelles is remarkably slow (4.1 ps), which implies that a very high local concentrations of Br^- must be present. To compare, a nearly saturated solution of 10 M NaBr in water gives rise to a vibrational relaxation rate of anion-bound water of only 3.6 ps. In reverse micelles even denser regions of bromide ions must occur, at molarities that cannot be reached in bulk solutions.

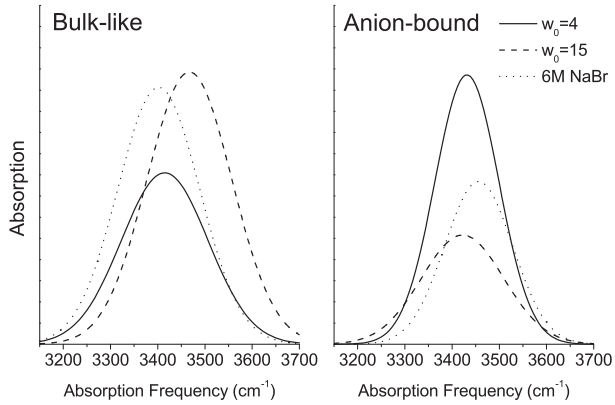

FIGURE 5.6. Gaussian absorption line-shapes for bulk-like and anion-bound water, extracted from pump-probe spectra. The data are scaled relatively to the sum of the spectrally integrated peak area of bulk-like and anion-bound water.

Interestingly, the vibrational relaxation of anion-bound water is anomalously slow for all studied sizes of micelles, as shown in Fig. 5.2. For all micelles the T_1 times are > 3.6 ps, showing that the local bromide concentration must be higher than 10 M in all cases. This is quite remarkable, as the average bromide concentration per micelle decreases from 18–3.5 M when increasing the micelle size from w_0=2 to w_0=15. The data thus show that the bromide-ions are strongly inhomogeneously distributed over the micelles. The large value of T_1 found for all micelles indicates that a very high density of ions must be present in a restricted region at the micellar interface. We thereby show that most anions are located inside or directly adjacent to the Stern layer.

These observations are consistent with a considerable amount of experimental [13,14,31,130,134] and theoretical [23,42,57,120] work which has been done on ion binding at charged aqueous interfaces of normal and reversed micelles. The degree of counter-ion binding at the interface is often expressed by the parameter β, giving the number of counter-ions that are bound per surfactant molecule. Experimental estimates of β exist for normal micelles dispersed in water [13, 23, 134] and for large water-in-oil microemulsions [31, 130], obtained by Small Angle Neutron Scattering (SANS) [13], Small Angle X-ray Scattering (SAXS) [134], NMR [130] and chemical trapping techniques [31]. For most surfactant salts, including CTAB [13, 31], β is in the range of 0.6-0.9. This means that for normal micelles and large reverse micelles ($w_0 \rightarrow \infty$), the majority of the counter-ions remain associated with the surfactant molecules within the Stern-layer, and do not enter the bulk aqueous phase. Experimental data on the counter-ion distributions within small reverse micelles is however very limited.

Our results show that also in small cationic reverse micelles, the counter-ion distribution is very inhomogenous over the micelle, with most bromide ions concentrated at the micelle interface. For small anionic (AOT) reverse micelles extensive MD-simulations exist [42,57], which also suggest the counter-ions mainly associate with the surfactant head groups. We may conclude that the anion-bound water component observed in the relaxation is mainly due to interfacial water, located in or near the Stern layer of the CTAB reverse micelle.

Degree of counter-ion solvation

By spectrally integrating the obtained line shapes for bulk-like and anion-bound water (see Fig. 5.6), we obtain the relative fractions A_{bulk} and A_{anion} for bulk-like and anion-bound water within the reverse micelles. Since we know the molar ratio between water and counter-ions, from these fractions we can deduce the average counter-ion hydration number. Note that no significant absorption cross-section difference is expected between anion-bound and bulk-like water [12].

While the bromide solvation shell contains 6 water molecules in bulk water [12, 101], the average hydration number in micelles turns out lower for the smallest micelles w_0=2 and 4, for which we find a hydration number of only 2.6±0.2 and 4.3±0.4, respectively, which means the bromide anions are only partly hydrated. The hydration number increases up to 7±2 for w_0>15, which is close to the bulk anion hydration number of 6. Since the Br^- anions reside predominantly at the interface, it can thus be concluded that the interface hydration increases as soon as the water content of the micelles is increased, as was shown previously for anionic reverse micelles [38, 43, 130]. The increased hydration of the interfacial region implies a lowering of the local concentration of Br^- anions. This lowering in concentration does not lead to a significant decrease of T_1, probably because in this concentration regime all donated hydrogen bonds are to Br^-, and not to other water molecules. It was shown previously, that the concentration dependence of T_1 of the solvating water molecules can be well explained from the increasing fraction of donated hydrogen bonds to other water molecules when the anion concentration is lowered [69].

The relative amplitude of the Br^- hydration shell component matches quite well with the interfacial water fraction of anionic AOT micelles, as shown in Fig. 5.5. Water molecules that solvate the sulfonate anionic head group of the AOT surfactant show a longer vibrational lifetime (2.8 ps) than water molecules coordinating other water molecules. On the basis of this long lifetime, such interfacial molecules can be distinguished from water in the core of the micelles, just as we can distinguish water inside and outside the bromide hydration shells in the CTAB system. As opposed to CTAB reverse micelles, which contain free bromide anions, the anionic group of the AOT is covalently bonded to the hydrophobic tail that forms the interface with the apolar solvent outside the micelle. The anionic head group is thereby geometrically confined to the outer shell of the micelle. Both the sulfonate head group [35] and the bromide anion [12, 101] can hydrogen bond 6 OH-groups, and no large cross-sectional

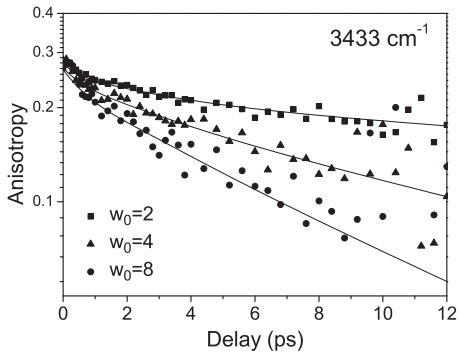

FIGURE 5.7. Anisotropy decay of the O–H stretch vibration at 3433 cm^{-1} for three sizes of CTAB reverse micelles (w_0=2,4 and 8). The mobility of anion-bound water increases when the micelle water content is increased.

difference exist for various anionic groups [12]. The degree of hydration of Br^- in CTAB reverse micelles shows therefore the same dependence on the water content w_0 as does the degree of hydration of sulfonate in AOT micelles.

5.3.3 Orientational Relaxation

Fig. 5.7 shows anisotropy decay curves for three sizes of micelles. The initial anisotropy $R(\omega, 0)$ equals .29±.02 at all probe frequencies ω, below the limiting value of 0.4. This indicates that our measurement does not capture all of the molecular reorientational dynamics, and a fast anisotropy decay occurs within the 100 fs time resolution of our experiment. A fast orientational relaxation within the first 150 fs has been experimentally resolved for bulk HDO:D_2O [47, 48]. This decay has been assigned to nondiffusive librational motions of water, which are equally present in the aqueous interior of reverse micelles [122].

From 0-2 ps an initial fast decay is observed in the anisotropy curves. Within this time-window, the short-lived signal of bulk-like water molecules contributes to the anisotropy. The fast decay is on the order of 2.5 ps, similar to the orientational relaxation found for bulk water. The fast component in the anisotropy decay becomes more pronounced for larger micelles, where the bulk-like water fraction is also larger. This suggests that bulk-like water is at least partially responsible for the fast anisotropy decay.

After ∼2 ps only bromide solvation shell water contributes to the signal, because of its much longer vibrational lifetime than bulk-like water. We observe a mono-exponential decay which is much faster for micelles with a high water content than for micelles with a low water content. This shows that the mobility of the anion-bound water gets considerably lowered when the confinement is

increased.

In analogy with the description of the vibrational relaxation, we will allow for different orientational mobilities for bulk-like and anion-bound water in describing the anisotropy decay. By use of Eq. 5.1, we can rewrite the expression for the anisotropy in Eq. 1.6 as follows:

$$R(\omega,t) = C_{\text{bulk}}(\omega,t)R_{\text{bulk}}(t) + C_{\text{anion}}(\omega,t)R_{\text{anion}}(t) \tag{5.2}$$
$$C_{\text{bulk}}(\omega,t) = \frac{\Delta\alpha_{\text{RF,fast}}(\omega,t)}{\Delta\alpha_{\text{RF}}(\omega,t)},\ C_{\text{anion}}(\omega,t) = \frac{\Delta\alpha_{\text{RF,slow}}(\omega,t)}{\Delta\alpha_{\text{RF}}(\omega,t)}.$$

$R_{\text{bulk}}(t)$ and $R_{\text{anion}}(t)$ are the anisotropy parameters for the bulk and anion-bound water sub-ensembles. The time-dependent fractions C_{bulk} and C_{anion} follow directly from the fit to the rotation free signal. We model R_{bulk} to decay single exponentially with an associated decay-constant of τ_{bulk}. R_{anion} is modelled to decay bi-exponentially, one fraction having a relative amplitude Q^2 and an associated decay-constant τ_{anion}, a second fraction having a faster associated decay-constant τ'.

$$R_{\text{bulk}}(t) = R_0\left(e^{-t/\tau_{\text{bulk}}}\right), \tag{5.3}$$

$$R_{\text{anion}}(t) = R_0\left(Q^2 e^{-t/\tau_{\text{anion}}} + (1-Q^2)e^{-t/\tau'}\right). \tag{5.4}$$

This model corresponds to the physical situation in which slowly reorienting anion-bound water - mostly located at the micelle interface - can undergo a second faster reorientation within a cone of semi-angle θ on a timescale τ_{cone} [81,122]. The relative amplitude Q^2 of the slow decay in the anion-bound water reorientation can be related to the cone semi-angle by

$$Q^2 = \left[\frac{1}{2}\cos\theta(1+\cos\theta)\right]^2. \tag{5.5}$$

Note that the case Q^2=1 corresponds to the case of a cone angle of 0°, in which the faster reorientation component for the anion-bound water is effectively put to zero. Values of Q^2 smaller than 1 imply a larger contribution of fast reorientation for the anion-bound water. The fast component in the anion orientational relaxation τ' is related to the time-constant τ_{cone} by

$$\tau' = 1/(\tau_{\text{cone}}^{-1} + \tau_{\text{anion}}^{-1}). \tag{5.6}$$

This time-constant will in practice be nearly equal to τ_{cone} because for the cases considered $\tau_{\text{anion}} \gg \tau_{\text{cone}}$.

Having determined the time-dependent fractions C_{bulk} and C_{anion} from the vibrational relaxation data, the model contains 5 adjustable parameters: Q^2, $R(\omega,0)\equiv R_0$, τ_{cone}, τ_{bulk} and τ_{anion}, of which only τ_{anion} is allowed to vary with micelle size. The values for these parameters are obtained from a global fit to the anisotropy curves at all spectral frequencies between 3350 and 3500 cm^{-1} for all micelles, simultaneously. The obtained fitting parameters are summarised in Table 5.1.

From the obtained value for τ_{bulk} of 3 ps, we conclude that within our experimental accuracy, the reorientation of water outside the anion solvation shells is equally fast as the reorientation known for bulk HDO:D_2O (3 ps [106]). This water is mainly located in the core of the droplets, and its dynamics does not seem to be strongly affected by the confinement, as was observed for anionic reverse micelles in chapter 4.

The reorientation rate of anion-bound water is observed to strongly decrease upon confinement, as seen from the values determined for τ_{anion}. An increasing hydration of the Stern layer of the reverse micelle, apparently increases the mobility of the interfacial water. At a water content of w_0=8, the reorientation of anion-bound water becomes equal to that of the anion solvation shell in bulk NaBr solutions, for which the reorientation of bromide solvation shells was shown to occur on a timescale of 11 ps [70]. The average bromide hydration number then equals nearly 6, just like the bulk hydration number, as seen from Table 5.2.

The time-scale of the faster motion of the anion-bound water turns out to be similar to that of the bulk-like water. From the fit we find that τ_{cone} and τ_{bulk} are both in the range 2.5-3.5 ps. In fact, the quality of the fit is not affected by taking the cone reorientation time-constant equal to the bulk reorientation time-constant, and within our experimental accuracy we can therefore assume

$$\tau_{\text{cone}} \equiv \tau_{\text{bulk}}. \tag{5.7}$$

The relative amplitude Q^2 of the slow anisotropy decay is determined to be 0.75± 0.05, which can be related by Eq. 5.5 to the average semi-angle of a cone in which this restricted motion takes place. We find a cone with a semi-angle of 25°. Water at the interfacial Stern layer thus undergoes a restricted reorientation over 50 degrees at the same rate as adjoining bulk-like molecules. Reorientation over larger angles in which the solvating structure of bromide needs to rearrange dramatically or break up, occurs on a slower timescale given by τ_{anion}. For bulk ionic solutions of NaBr, similar Q^2 values need to be assumed as well.

In the previous chapter, a recovery of the anisotropy (occurring if $Q^2 \sim 1$, see Fig. 5.8), was observed for water in anionic AOT reverse micelles. Such a dynamic signature is a good indicator of inhomogeneous reorientation of water inside reverse micelles [38, 99]. In the most simple case of a bimodal system, such behaviour should be observed when the more slowly reorienting species also has a longer vibrational lifetime than the faster reorienting species, as is the case for water in CTAB micelles. Fig. 5.8 illustrates however, that a certain degree of faster motion for the slowly reorienting species, can strongly suppress this characteristic dynamics for inhomogeneous reorientation, even though the water reorientation throughout the droplet remains strongly inhomogeneous.

The fact that an anisotropy recovery is observed in AOT reverse micelles and not in CTAB reverse micelles, can be explained by differences between the anion-bound water found in CTAB micelles, and the interfacial water found in AOT micelles. Interfacial water in AOT micelles consists of water molecules hydrogen-bonding to the anionic sulfonate head groups of the AOT.

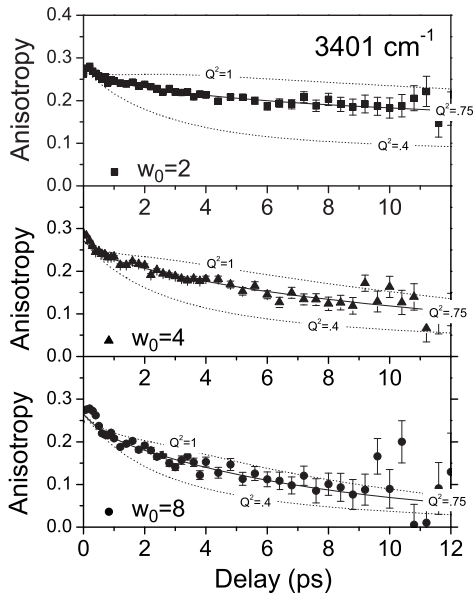

FIGURE 5.8. Anisotropy decay curves and their fits on a linear scale for three sizes of micelles. For each graph, additional curves for Q^2=1 and Q^2=.4 have been added for comparison, corresponding to cone-angles of θ=0°and 43°, respectively. For Q^2 very near to 1, the anisotropy decay is slowed down at early delays, in specific cases leading even to a recovery of the anisotropy.

The hydrogen-bonding of water to sulfonate and bromide is strikingly different, as illustrated in Fig. 5.9. The bromide ion is much larger than the oxygens of sulfonate that can accept hydrogen bonds from water. Because of the large polarizable electron cloud of the bromide ion, its hydrogen bonding will be much less directional than in the case of sulfonate. A less directional hydrogen bond will allow for a higher orientational mobility of the neighbouring water molecules. This can explain a Q^2 value closer to unity for water hydrogen bonding to AOT, as compared to water hydrogen bonding to halogenic ions.

5.4 Conclusions

We studied the ultrafast dynamics of isotopically diluted water confined in cationic CTAB reverse micelles. Based on differences in the vibrational relaxation rate, we can distinguish between OH-groups that are hydrogen-bonded to surfactant counterions and OH-groups that are not. We find an anomalously slow vibrational relaxation rate for water hydrogen-bonded to the counteri-

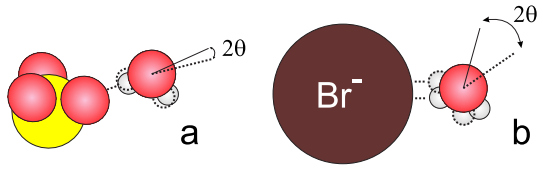

FIGURE 5.9. Directionality of the hydrogen-bond between water and sulfonate (a) and between water and bromide (b). The angle θ refers to the cone semi-angle given in Eq. 5.5.

ons. This observation implies that very high local concentrations of Br^- anions (>10M) must be present, and that the Br^- anions are not homogenously distributed over the micelle. Together with the observation that the vibrational relaxation rate of anion-bound water does not vary significantly with the micelle water content (and therefore neither does the local Br^- concentration), we conclude that most of the counterions reside at the micellar interface in or near the Stern layer. Anion-bound water therefore has strong interfacial character.

Within our experimental accuracy, bulk-like water in the core of the micelles is found to have an orientational mobility similar to bulk liquid water, as was found previously for anionic AOT micelles. Water bound to Br^-, found predominantly at the micellar interface, has a much lower orientational mobility. Its associated reorientational time constant strongly decreases with micelle size from 55 to ∼8 ps. This decrease shows that water molecules in the bromide-rich interfacial region of the micelle become more mobile when the micelle water content is increased.

Besides a slow reorientational motion, anion-bound water molecules also undergo a faster but restricted reorientation on the same timescale as the bulk-like molecules. This motion can on average be described by diffusional motion in a cone with a semi-angle of 25°. The size of the cone is independent of the micelle size. This fast reorientational motion was not observed for interfacial water in AOT micelles (see chapter 4). For AOT micelles, the interfacial water is characterised by its hydrogen-bonding to the anionic sulfonate head groups of the AOT surfactant molecules. We explain these different mobilities from a lower directionality of the water–bromide hydrogen bond compared to the water–sulfonate hydrogen bond. A hydrogen-bond of low directionality allows for a higher mobility of the water molecule while leaving its hydrogen bond intact. Interfacial water in CTAB micelles therefore shows a larger cone angle for fast reorientational motion than interfacial water in AOT reverse micelles.

5.5 Appendix: Kinetic Modelling

We describe our system by two sub-ensembles of water molecules, denoted by the index $i \in \{\text{fast}, \text{slow}\}$. One group of molecules hydrogen-bonds to other water molecules, and has a vibrational lifetime T_{fast}. A second group of molecules

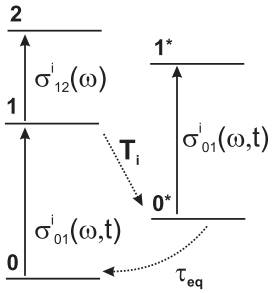

FIGURE 5.10. Schematic overview of the model that describes the population dynamics for both types i of excited HDO molecules ($i \in \{\text{fast}, \text{slow}\}$). Relaxation from the excited 1 state proceeds via an intermediate level 0^*. The cross section of the intermediate level is taken to be equal to that of the ground state. The cross section of the 1→2 transition is assumed to be time independent.

hydrogen-bonds to Br^- ions, and has a vibrational lifetime T_{slow}. The population dynamics of excited molecules of each of these types is schematically depicted in Fig. 5.10. As was found previously for bulk HDO:D_2O [106], we assume that the vibrational relaxation of the OH vibration proceeds via an intermediate level 0^*.[a] The excitation subsequently relaxes back to the ground state 0, thereby thermally populating low frequency modes. The following equations describe the dynamics of the molecules that were excited by the pump pulse.

$$\begin{aligned}
\frac{dN_{1,i}}{dt} &= -\frac{1}{T_i}N_{1,i} \qquad\qquad i \in \{\text{fast}, \text{slow}\},\\
\frac{dN^*_{0,i}}{dt} &= \frac{1}{T_i}N_{1,i} - \frac{1}{\tau_{\text{eq}}}N^*_{0,i},\\
\frac{dN_{0,i}}{dt} &= \frac{1}{\tau_{\text{eq}}}N^*_{0,i}.
\end{aligned} \tag{5.8}$$

$N_{1,i}$, $N^*_{0,i}$ and $N_{0,i}$ refer to the populations of the levels depicted in Fig. 5.10, for each sub-ensemble i (the populations $N_{0,i}$ are defined as the population difference with respect to the steady-state population). τ_{eq} equals the lifetime of the intermediate state. As a boundary condition we assume that on t=0 the number of molecules in the excited state equals the number of molecules removed from the ground state:

$$N_{0,i}(0) = -N_{1,i}(0). \tag{5.9}$$

[a]The intermediate state accounts for a slightly delayed ingrowth (by 0.6 ps) of thermal effects observed in bulk HDO:D_2O. For water in CTAB micelles it is unclear from the data whether this intermediate state is present or not. We find no significant change in any of the obtained fit parameters when leaving out the intermediate state, but it was taken into account on the basis of the earlier work on bulk water. Note that in the previous chapter 4 we did not include this intermediate state, and also in this case subsequent inclusion does not lead to a significant change of any obtained parameters.

When the excited molecules relax to the ground state, the reverse micelles in the sample are gradually heated. Heating affects all water molecules in the reverse micelles, including those molecules that were not excited by the pump pulse. The micelles subsequently cool to the surrounding solvent on a picosecond timescale [112]. Because of heating, the two cross-section spectra ($\sigma^i_{01}(\omega,t),\ i \in \{\text{fast}, \text{slow}\}$) slightly blue-shift and decrease amplitude, resulting in thermal absorption changes $\Delta\alpha_{\mathrm{T}}(\omega,t)$ observed in the experiments.

We assume the change of each spectrum $\sigma^i_{01}(\omega,t)$ upon heating to be proportional to the total number of molecules $\sum_i N_{\mathrm{rel},i}$ that have decayed to the ground state (where $N_{\mathrm{rel},i}$ is the number of relaxed molecules of type i), multiplied by an exponential factor to account for the cooling of the micelles to their surroundings:

$$\begin{aligned} N_{\mathrm{rel},i}(t) = &\quad \textstyle\int_{t'=0}^{t} \frac{1}{\tau_{\mathrm{eq}}} N^*_{0,i}(t')dt', \\ \Delta\sigma^i_{01}(\omega,t) = &\quad \sigma^i_{01}(\omega,t) - \sigma^i_{01}(\omega,0) \\ \propto &\quad \textstyle\sum_i N_{\mathrm{rel},i}(t) \times e^{-t/\tau_{\mathrm{cool}}}. \end{aligned} \tag{5.10}$$

Although heated micelles in general show non-exponential cooling behavior [112], single-exponential cooling is a good approximation for the time-window (0-40 ps) considered in our experiments.

The total rotation-free pump-probe signal can be written in terms of the populations of the levels in Fig. 5.10, the absorption cross-sections σ between these levels, and the total concentration of absorbing molecules C.

$$\begin{aligned} \Delta\alpha(\omega,t) = \sum_i \Big[& C\Delta\sigma^i_{01}(\omega,t) + N_{1,i}(t)\sigma^i_{12}(\omega) \\ & + \Big(N_{0,i}(t) - N_{1,i}(t) + N^*_{0,i}(t)\Big)\sigma^i_{01}(\omega,t)\Big]. \end{aligned} \tag{5.11}$$

By solving for the rate-equations (5.8) and assuming that the fraction of excited molecules $\sum_i N_{1,i}(0)/C$ is a small number, we find

$$\begin{aligned} \Delta\alpha(\omega,t) = \sum_i \Big[& C\Delta\sigma^i_{01}(\omega,t) \\ & + N_{1,i}(0)\big[\sigma^i_{12}(\omega) - 2\sigma^i_{01}(\omega,0)\big]e^{-t/T_i}\Big]. \end{aligned} \tag{5.12}$$

By direct comparison with Eq. 5.1 we find for the pump-probe spectrum of each component i

$$\sigma_{\mathrm{PP},i}(\omega) = N_{1,i}(0)\big[\sigma^i_{12}(\omega) - 2\sigma^i_{01}(\omega,0)\big], \tag{5.13}$$

and for the functional form of the thermal signal:

$$\Delta\alpha_{\mathrm{T}}(\omega,t) = C\sum_i \Delta\sigma^i_{01}(\omega,t). \tag{5.14}$$

The number of relaxed molecules $N_{\mathrm{rel},i}(t)$ determines the dynamics of the thermal signal and has a solution

$$\begin{aligned} N_{\mathrm{rel},i}(t) &= N_{0,i}(t) - N_{0,i}(0) \\ &= N_{1,i}(0)\left(\frac{\tau_{\mathrm{eq}}}{T_i - \tau_{\mathrm{eq}}} e^{-t/\tau_{\mathrm{eq}}} - \frac{T_i}{T_i - \tau_{eq}} e^{-t/T_i} + 1\right). \end{aligned} \quad (5.15)$$

From this equation we see, that the dynamics of the total heating signal depends on the initial populations $N_{1,i}(0)$. In our fitting procedure we assume that the area of the positive bleaching part of the spectra $\sigma_{\mathrm{PP},i}(\omega)$ is proportional to these initial populations:

$$N_{1,i}(0) \propto \int_{\mathrm{bleach}} \sigma_{\mathrm{PP},i}(\omega) d\omega. \quad (5.16)$$

In terms of the lineshape functions defined in section 5.3.2 we can write for this integral

$$\int_{\mathrm{bleach}} \sigma_{\mathrm{PP},i}(\omega) d\omega = N_{1,i}(0)\ \sigma_{01}^{i}(\omega_{\max}, 0)\mathrm{Erf}\left(\frac{\alpha_i}{2\sqrt{2}\Delta_i}\right), \quad (5.17)$$

showing that the proportionality in Eq. 5.16 holds when the line widths Δ, cross-sections and anharmonicities α of the two subensembles i are similar. Considering the O–H stretch line shape for pure HDO:D_2O and Br^--bound water [12], this is a reasonable assumption. We define

$$f_i \equiv N_{1,i}(0) / \sum_i N_{1,i}(0) \quad (5.18)$$

as the normalised fraction of molecules of type i contributing to the pump-probe signal.

By use of Eq. 5.10 and 5.15, we can then rewrite Eq. 5.12 for the total pump-probe signal:

$$\begin{aligned} \Delta\alpha(\omega, t) = &\sum_i \sigma_{\mathrm{PP},i}(\omega) e^{-t/T_i} + \Delta\alpha_{\mathrm{T}}(\omega)\ e^{-t/T_{\mathrm{cool}}} \times \\ &\sum_i f_i \left(\frac{\tau_{\mathrm{eq}}}{T_i - \tau_{\mathrm{eq}}} e^{-t/\tau_{\mathrm{eq}}} - \frac{T_i}{T_i - \tau_{\mathrm{eq}}} e^{-t/T_i} + 1\right). \end{aligned} \quad (5.19)$$

In this equation $\Delta\alpha_{\mathrm{T}}(\omega)$ is the proportionality constant between $\Delta\alpha_{\mathrm{T}}(\omega, t)$ and $\sum_i N'_{0,i}(t)$. This factor equals the thermal spectrum found at large delays when all population dynamics on the timescales T_i and τ_{eq} is complete. The $\sigma_{\mathrm{PP},i}(\omega)$ are the pure pump probe spectra of Eq. 5.13.

Our experimental data are fitted to Eq. 5.19, for which fractions f_i are calculated in each optimisation step. The lifetime τ_{eq} of the intermediate state is taken to be 0.6 ps for both components, according to the previously determined value for bulk HDO:D_2O [106]. We should note that the quality of the fit, the

time-constants T_i and the shape of the determined pump-probe spectra $A_i(\omega)$ are hardly affected by the precise value of τ_{eq}, because the heating signal is in general small compared to the pump-probe signal. After optimisation, the fitted heating signal is subtracted from $\Delta\alpha(\omega,t)$ to obtain the pure rotation-free pump-probe signal $\Delta\alpha_{\mathrm{RF}}(\omega,t)$:

$$\Delta\alpha_{\mathrm{RF}}(\omega,t) = \Delta\alpha(\omega,t) - \Delta\alpha_{\mathrm{T}}(\omega,t). \tag{5.20}$$

The heating signal is assumed to be isotropic, and the same functional form is subtracted from both the parallel and perpendicular absorption changes to obtain the pure pump-probe signals $\Delta\alpha_{\parallel}(\omega,t)$ and $\Delta\alpha_{\perp}(\omega,t)$. These signals are used to construct the anisotropy $R(\omega,t)$ using Eq. 1.6.

Only data points after 0.4 ps are considered in order not to exclude any coherent artifacts arising during time-overlap between the pump and probe pulses. Since the O–H stretch absorption was pumped at its centre, and the spectral width of the pump-pulse was about as broad as the absorption line width, no significant spectral diffusion was observed. When pumping the O–H stretch absorption at its flanks, we do observe spectral diffusion.

No heating signal is observed for micelles of $w_0 \leqslant 4$. For larger micelles, the heating signal is observed to increase with w_0. Its amplitude $\Delta\alpha_{\mathrm{T}}(\omega,t)$ becomes of similar amplitude as the pump-probe signal $\Delta\alpha_{\mathrm{RF}}(\omega,t)$ at t=5 ps for w_0=8, at 3.5 ps for w_0=15 and at 2 ps for w_0=30. The decay of the thermal signal due to cooling of the micelles is well described up to 40 ps. We find τ_{cool}=50, 80 and 150 ps for w_0=8, 15, 30, respectively.

TABLE 5.1. O–H stretch vibrational and reorientational lifetimes (in ps) and parameters of bulk-like and anion-bound water in CTAB reverse micelles.

w_0	$T_{1,\mathrm{bulk}}$(ps)	$T_{1,\mathrm{anion}}$(ps)	τ_{bulk}(ps)	τ_{anion}(ps)	R_0	Q^2	θ
2	1.2 (0.2)	4.4 (0.2)	3 (1)	55 (10)	0.28 (0.02)	0.8 (0.1)	25°(5)
4	0.7 (0.2)	4.2 (0.2)	3 (1)	17 (2)	0.29 (0.02)	0.8 (0.1)	25°(5)
8	0.7 (0.1)	4.3 (0.3)	3 (1)	9 (2)	0.28 (0.02)	0.8 (0.1)	25°(5)
15	0.7 (0.1)	4.0 (0.3)	3 (1)	8 (2)	0.28 (0.02)	0.8 (0.2)	25°(10)
bulk[a]	0.7 (0.1)	-	2.5 (0.2)	-	0.3 (0.02)	-	-
2M NaBr	0.6 (0.1)	2.5 (0.2)	3 (1)	9 (2)	0.26 (0.02)	0.8 (0.2)	25°(10)
6M NaBr	0.7 (0.1)	3.0 (0.2)	3 (1)	9 (2)	0.26 (0.02)	0.8 (0.1)	25°(5)

TABLE 5.2. Relative Fractions and line shape parameters of bulk-like and anion-bound water in CTAB reverse micelles.

w_0	solv[b]	T (K)	A_{bulk}	A_{anion}	n_{Br^-} [c]	ν_{bulk} (cm^{-1})	ν_{anion} (cm^{-1})	Δ_{bulk} (cm^{-1})	Δ_{anion} (cm^{-1})
2	I	295 (2)	0.34 (0.05)	0.66 (0.05)	2.6 (0.2)	3409 (5)	3433 (5)	69 (8)	61 (8)
4	I	295 (2)	0.46 (0.05)	0.54 (0.05)	4.3 (0.4)	3415 (5)	3431 (5)	92 (8)	68 (8)
8	I	295 (2)	0.57 (0.05)	0.43 (0.05)	6.9 (0.8)	3463 (5)	3426 (5)	80 (8)	68 (8)
15	II	315 (5)	0.7 (0.1)	0.3 (0.1)	7 (2)	3467 (5)	3422 (5)	90 (8)	87 (8)
30	II	315 (5)	0.8 (0.1)	0.2 (0.1)	7 (2)	3501 (5)	3437 (5)	81 (8)	64 (8)
bulk	III	298 (2)	1	0	-	3419 (5)	-		
2M NaBr	IV	298 (2)	0.82 (0.05)	0.18 (0.05)	6 (1)	3400 (5)	3450 (5)	102 (8)	73 (8)
6M NaBr	IV	298 (2)	0.65 (0.05)	0.35 (0.05)	4.9 (0.6)	3402 (5)	3456 (5)	86 (8)	72 (8)

[a] values taken from Rezus et al. [106].
[b] Solvents used: I dichloromethane, II 1:2 isooctane:chloroform, III 1:1000 H_2O:D_2O, IV 1:500 H_2O:D_2O.
[c] Bromide coordination number has been determined using a 1:1 cross-sectional ratio between bulk and anion-bound water.

Chapter 6

Vibrational relaxation of confined neat water

We study the vibrational dynamics of nanodroplets of neat liquid water (H_2O) with femtosecond two-color mid-infrared pump-probe spectroscopy. For the smallest nanodroplet, containing 10-15 water molecules, the lifetime T_1 of the O–H stretch vibrations is equal to 0.85±0.1 ps, which is more than three times as long as in bulk liquid water. We find that the truncation of the hydrogen-bond network of water leads to a dramatic change of the relaxation mechanism.

6.1 Introduction

In a study of the vibrational dynamics of pseudohalide ions (N_3^-, NCO^- and NCS^-) in aqueous solution [135, 136], it was found that the vibrational lifetime time changes when such ions are confined in reverse micelles. The vibrational lifetime was found to increase when the size of the micelle was decreased. Here we present a systematic study of the effect of nanoconfinement on the vibrational dynamics of neat water itself. We find that the confinement to the nanometre scale leads to an increase of the lifetime of the O–H stretch vibrations of the water molecules that is much stronger than can be expected from the change in vibrational frequency.

6.2 Experimental

The investigated samples were mixtures of the surfactant AOT (sodium di-2-ethylhexylsulfosuccinate, Aldrich, 99%), *n*-octane (Aldrich, anhydrous grade 99+%) and water H_2O (Aldrich, HPLC grade). The molar water-to-AOT ratio w_0 was set to $1, 2, 4, 7$ and 12 respectively, creating reverse micelles containing a water pool consisting of ∼10 to ∼10.000 water molecules. The radius R in nm

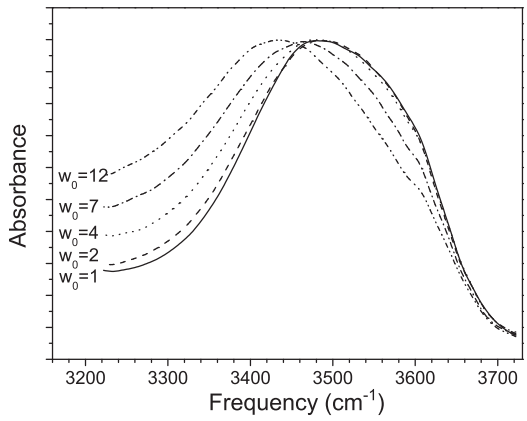

FIGURE 6.1. Linear infrared absorption spectra of the O–H stretch vibrations of water in AOT/water/octane reverse micelles of various sizes: $w_0 = 1, 2, 4, 7$ and 12. The spectra are normalised for comparison. The absorption at the low-frequency side contains a strong contribution of the high-frequency wing of the absorption of the C–H stretch vibrations of AOT and *n*-octane.

of the micelle can be approximated from $R = 0.15 \times w_0$, with w_0=[H_2O]/[AOT] [112].

In the pump-probe experiment we monitor the time-dependent absorption changes that result from the pump excitation by a probe pulse with a polarisation at the magic angle (54.7°) with respect to the polarisation of the pump. At this polarisation angle all absorption changes related to molecular reorientation are averaged out, and we only record the isotropic absorbance change ($\Delta\alpha(\omega, t) = \Delta\alpha_{RF}(\omega, t)$).

6.3 Results and Discussion

Fig. 6.1 shows the linear absorption spectrum of the OH-stretching band of water confined in reverse micelles of various sizes. The amplitude of the low-frequency part of the OH absorption band strongly decreases as the water content is reduced. Fig. 6.2 displays transient spectra for a reverse micelle with $w_0 = 4$. At early delays the transient spectra reveal a bleaching at the $v = 0 \rightarrow 1$ transition around 3500 cm^{-1} and an induced absorption at the $v = 1 \rightarrow 2$ transition extending from 3300 cm^{-1} to below 3000 cm^{-1}. The measurable spectral range was limited on the low-frequency side by the strong C-H absorption of AOT and the octane solvent. At longer delays the transient spectrum takes the form of a thermal difference spectrum: upon heating the OH-stretch band shifts slightly to the blue and its area is reduced.

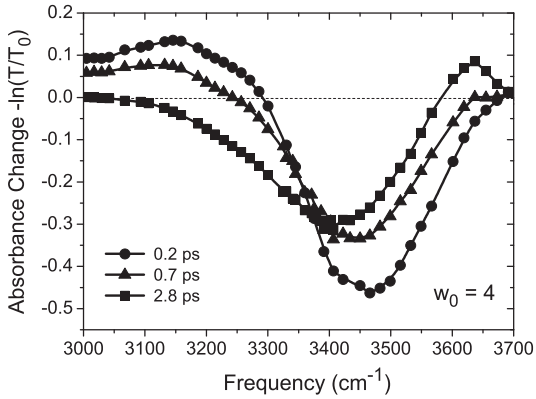

FIGURE 6.2. Transient spectra measured for reverse micelles with $w_0 = 4$ at three different delays. The spectra are measured with a pump frequency of 3450 cm^{-1}.

The delay curves in the top of Fig. 6.3a,b show an induced absorption corresponding to the $v = 1 \rightarrow 2$ transition of the O–H stretch vibration. The comparison of the decay rates measured for micelles with $w_0 = 2$ and $w_0 = 7$ shows that the lifetime of the $v = 1$ state increases when the micelle becomes smaller. The vibrational relaxation leads eventually to heating of the micelle, leading to an increase of the transmission at the red side of the O–H absorption band. This heating effect is also clearly present in the middle traces of Fig. 6.3a,b. The heating of the micelles is followed by a cooling process in which energy is transferred to the surrounding solvent. The lower traces of Fig. 6.3a,b show an initial transmission increase due to the bleaching of the fundamental $v = 0 \rightarrow 1$ transition of the O–H stretch vibration. In the lower curve of Fig. 6.3b it is clearly seen that the thermalisation is delayed with respect to the vibrational relaxation. This implies that the relaxation of the $v = 1$ state of the O–H stretch vibration first leads to population of a non-thermal intermediate state. Only after the subsequent relaxation of this intermediate state, the energy becomes thermalised over the micelle. This relaxation mechanism is only observed for micelles with $w_0 \geq 4$.

We use a simple kinetic model to extract the vibrational relaxation time constants from the data. We do not observe any effect of spectral hole burning in the experiments which shows that the spectral diffusion in the O–H stretch vibrational band is much faster than the vibrational relaxation, in agreement with previous results obtained for bulk liquid water [131]. For micelles with $w_0 = 4, 7, 12$, the population $N_1(t)$ of the excited $v = 1$ state first relaxes to a non-thermal combination of accepting modes 0^* with time constant T_1. The relaxation of 0^* with time constant τ_{eq} leads to an equilibration of the energy

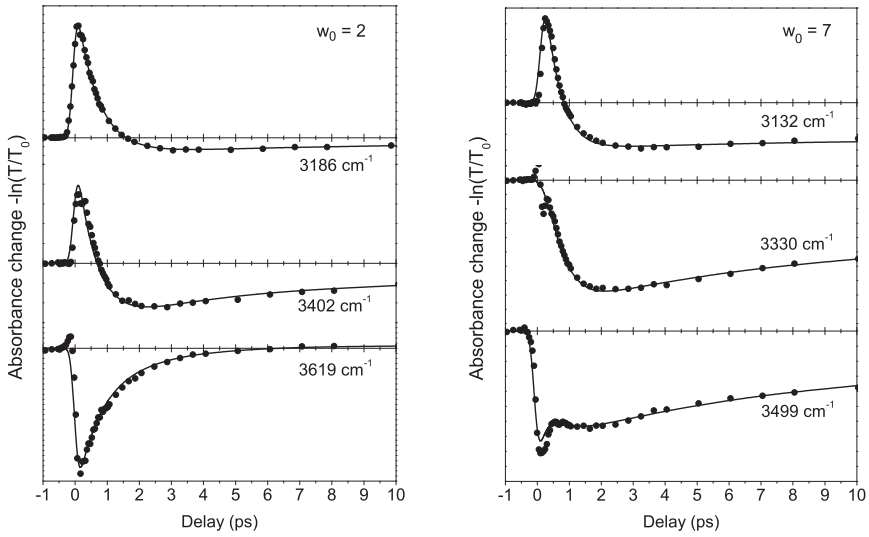

FIGURE 6.3. Delay time scans measured at three different probe frequencies for reverse micelles with $w_0 = 2$ (Fig. a) and $w_0 = 7$ (Fig. b). The solid curves are obtained from a fit to the kinetic model described in the text.

over the full water pool of the reverse micelle, which brings the micelle at an elevated temperature. As a result of this higher temperature the absorption spectrum of the water molecules changes, which leads to a thermal absorbance change $\Delta\alpha_{\mathrm{T}}(\omega, t)$ observed in the pump probe experiment. For the smallest micelles with $w_0 = 1$ and $w_0 = 2$ we did not observe a non-thermal intermediate state 0^*. Hence, in the modelling of these micelles the population N_1 is directly thermalised with time constant T_1.

The heating effect $\Delta\alpha_{\mathrm{T}}(\omega, t)$ decays due to cooling of the micelle. This cooling is a thermal diffusion process, which implies that its dynamics are non-exponential [112]. We do not pursue to investigate the cooling process in detail, and we describe this process with a single or bi-exponential function. This gives an accurate description of the cooling up to a delay of 10 ps. For all micelles the cooling time constants are much longer than T_1 and τ_{eq}.

The time-dependent absorption change $\Delta\alpha\,(\omega, t)$ resulting from the relaxation dynamics is given by:

$$\Delta\alpha\,(\omega, t) = \sigma_{\mathrm{PP}}(\omega) N_1\,(t) + \Delta\alpha_{\mathrm{T}}(\omega, t), \tag{6.1}$$

where

$$\sigma_{\mathrm{PP}}(\omega) \quad = \quad [\sigma_{12}(\omega) - 2\sigma_{01}(\omega)]\,. \tag{6.2}$$

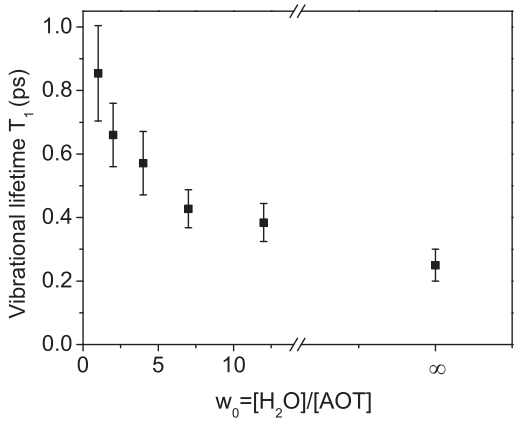

FIGURE 6.4. Vibrational lifetime T_1 of the O–H stretch vibrations as a function of the value of w_0 of the reverse micelle. Also shown is the value of T_1 measured for bulk liquid water [83].

The population $N_1(t)$ and the time evolution of the heating effect are obtained from solving the appropriate differential equations, fully analogous to the treatment in the appendix of chapter 5.

The delay-dependent absorption change $\Delta\alpha\,(\omega,\tau)$ is obtained by convoluting $\Delta\alpha\,(\omega,t)$ with a gaussian function representing the cross-correlation trace of the pump and probe pulses. In fitting $\Delta\alpha\,(\omega,\tau)$ to the data, we only considered delays >0.2 ps, when coherent coupling effects have become negligibly small.

For each micelle size all (∼50) recorded time traces are simultaneously fitted, yielding T_1, $\tau_{\rm eq}$, $\sigma_{\rm PP}(\omega)$, and the spectrum of the heating effect $\Delta\alpha_{\rm T}(\omega)$. The values of T_1 are shown as a function of w_0 in Fig. 6.4. The value of $\tau_{\rm eq}$ (for micelles with $w_0 = 4, 7, 12$) equals 0.3±0.1 ps. The resulting cross-section difference spectrum $\sigma_{\rm PP}(\omega)$ is very similar to the pump-probe spectrum at 0.2 ps shown in Fig. 6.2. These spectra are dominated by the bleaching of the $v = 0 \rightarrow 1$ transition and the induced absorption of $v = 1 \rightarrow 2$ transition. The cross-section spectrum of the heating effect $\Delta\alpha_{\rm T}(\omega)$ is very similar in shape to the pump-probe spectrum measured at 2.8 ps shown in Fig. 6.2. This spectrum represents the difference of the spectrum of the micelle at an elevated temperature with that at room temperature.

For all micelle sizes, we observe that the vibrational relaxation is not completely single exponential. This behaviour hints at the presence of inhomogeneity in the studied samples. It should be noted here that the inhomogeneity of the water in the micelles, although most certainly present, cannot be observed in this experiment. In liquid water an excitation of the O–H stretch

vibration rapidly hops from one molecule to another, which implies that the excitation samples all different types of local O–H oscillators on a very short time scale (<100 fs) [29,131]. As a result, the observed relaxation is not a multi-component process containing for instance a component of interfacial water and components of core water, but instead a single component with a time constant that is a weighted average of the T_1 values of all O–H oscillators within the micelle. Hence, the slight deviation from single-exponential character that we observe in our experiment most likely results from the variation in the size of the micelles. The size of the reverse micelles has a polydispersity with a width that ranges from ∼30% for small w_0 to ∼15% for large w_0 [97].

Fig. 6.4 shows that the vibrational lifetime of the O–H stretch vibrations of water strongly increases with decreasing size of the reverse micelles. With decreasing micelle size also the fraction of interface water increases, for which T_1 can differ from that of the water in the core. However, the increase of the experimentally observed average value of T_1 cannot be just explained from an increased contribution of interfacial water. The relative amount of the interfacial water increases from ∼10% for the largest micelle with $w_0 = 12$, to near 100% for a micelle with $w_0 = 1$. Hence, if the increase of T_1 of a micelle with $w_0 = 12$ with respect to bulk water would only result from an increased contribution of interfacial water, the observed T_1 would increase by only a few percent in comparison to bulk liquid water. Instead, T_1 increases by ∼50%. Hence, the confinement affects the vibrational relaxation rate of *all* water molecules in the micelle. This notion agrees with the observation that even for micelles with $w_0 > 20$ the vibrational spectrum differs from that of bulk liquid water [49,125].

The increase of T_1 is much stronger than is usually observed for hydrogen-bonded systems. For many hydrogen-bonded systems T_1 is related to the O–H stretch frequency ω_{OH} by [89]:

$$T_1(\omega) = a(\omega_{\mathrm{OH}} - \omega_{\mathrm{OH,g}})^{-1.8}, \tag{6.3}$$

with a a constant and $\omega_{\mathrm{OH,g}}$ the vibrational frequency of the O–H group in the gas phase. Using $\omega_{\mathrm{OH,g}} = 3706$ cm^{-1} (average of the symmetric and asymmetric O–H stretch vibrations), $\omega_{\mathrm{OH,hb}} = 3420$ cm^{-1} for bulk liquid water, and $\omega_{\mathrm{OH,hb}} = 3480$ cm^{-1} for a micelle with $w_0 = 1$, the value of T_1 is expected to increase from ∼260 fs [83] to ∼400 fs, going from bulk to $w_0 = 1$. The latter value of T_1 is more than two times shorter than the measured value of 0.85±0.1 ps, which is surprising since for bulk HDO:D_2O equation (6.3) is closely followed when the frequency of the O–H stretch vibration is varied by changing the temperature [133].

A striking observation is that the nanoconfinement leads to a drastic change of the relaxation mechanism. For micelles with $w_0 \geq 4$, the relaxation of the O–H stretch vibration leads to population of a non-thermal intermediate state, whereas for micelles with $w_0 = 1$ and $w_0 = 2$ such a state is not observed. The non-thermal intermediate state that can no longer be reached for small micelles is likely formed by the overtone of the H–O–H bending mode. This overtone has a frequency of ∼3300 cm^{-1}, and is thus in resonance with the red wing of the O–H stretch absorption band of bulk liquid water. The truncation

of the hydrogen-bonded network leads to a weakening of the hydrogen-bond interactions between the water molecules. As a result, the red wing of the absorption spectrum of the O–H stretch vibrations vanishes (Fig. 6.1), which implies that the overlap with the overtone of the H–O–H bending mode strongly decreases. The nanoconfinement also leads to a small red shift of a few cm^{-1} of the H–O–H bending mode, thus contributing to the loss of overlap with the O–H stretch vibration.

The assignment of the non-thermal intermediate state to the overtone of the bending mode is supported by the observation that the relaxation of the O–H stretch vibrations leads to excitation of the bending mode for bulk liquid water [33], but not for $w_0 = 2$ micelles [34]. The relaxation time constant τ_{eq} thus likely represents the vibrational lifetime of the first and/or second excited state of the H–O–H bending mode. Recently, the lifetime of the first excited state of the bending mode was measured to be ∼0.2 ps [59], which agrees quite well with the value of τ_{eq} of 0.3±0.1 ps. The bending mode itself can only relax to intermolecular modes of which the librations have the highest frequencies (∼800 cm^{-1}). The librational frequencies show a decrease of ∼25% when liquid water is confined in a micelle with $w_0 = 1$ [125], which probably will affect τ_{eq}. Unfortunately, we could determine τ_{eq} only in the interval from $w_0 = 12$ to $w_0 = 4$, and we did not find a statistically significant change.

The Fermi resonance of the O–H stretch vibrations with the overtone of the H–O–H bending mode is a special property of H_2O water. For most other systems, including HDO and alcohols, the overtone of the bending mode is far out of resonance with the stretch vibration. This difference in resonance explains why the value of T_1 of bulk liquid H_2O is ∼3 times shorter than that of bulk liquid HDO:D_2O [133]. Nanoconfinement of water leads to a vanishing of the low-frequency O–H stretch vibrations, and thus to a closing of the relaxation channel to the overtone of the H–O–H bending mode. As a result, for small micelles with $w_0 = 1$, the value of T_1 is similar to that of HDO:D_2O at the same frequency of the O–H stretch vibration [133] (attained at an elevated temperature), and to that of ethanol clusters at the same frequency [132]. We conclude that the confinement of liquid water to the nanometre scale leads to a loss of its special vibrational relaxation properties, thus making this liquid much more similar to other hydrogen-bonded liquids. This effect of nanoconfinement explains why the increase of T_1 with decreasing micelle size is anomalously strong, and cannot be described with equation (6.3).

Chapter 7

Transient absorption of vibrationally excited ice *Ih*

The ultrafast dynamics of HDO:D_2O ice *Ih* at 180 K is studied by mid-infrared ultrafast pump-probe spectroscopy. The vibrational relaxation of HDO:D_2O ice is observed to proceed via an intermediate state, which has a blue-shifted absorption spectrum. Polarisation resolved measurements reveal that the interediate state is part of the intramolecular relaxation pathway of the HDO molecule. In addition, slow dynamics on a time scale of the order of 10-100 ps is observed, related to thermally induced collective reorganisations of the ice lattice. The transient absorption line shape is analysed within a Lippincott-Schröder model for the O–H stretch potential. This analysis identifies the main mechanism behind the strong spectral broadening of the $v_{\mathrm{OH}} = 1 \rightarrow 2$ transition.

7.1 Introduction

While the ultrafast dynamics of liquid water has been studied in great detail, time-resolved studies on the properties of ice have so far been limited. In the study of water, vibrational spectroscopies have proven to be very useful, in particular because of the sensitivity of vibrations to local hydrogen bonding. The phase transition associated with freezing HDO:D_2O water leads to a strong narrowing of the O–H stretch absorption, from a width of 200 cm^{-1} in water at 298 K to only 50 cm^{-1} in ice at 180 K. This narrowing results from the transition from a disordered liquid phase to an ordered crystalline phase. The water molecules in ice are positioned on a regular hexagonal lattice, hydrogen bonded to four nearest neighbours. This ordering leads to a strong reduction of the spread in hydrogen bond lengths. Since there exists a strong correlation between the O–H stretch absorption frequency and the hydrogen bond length, the narrowing of the hydrogen bond distribution also leads to a narrowing of the OH vibrational spectrum.

Despite the relative uniformity in the OH$\cdots$O hydrogen bonds, the structure

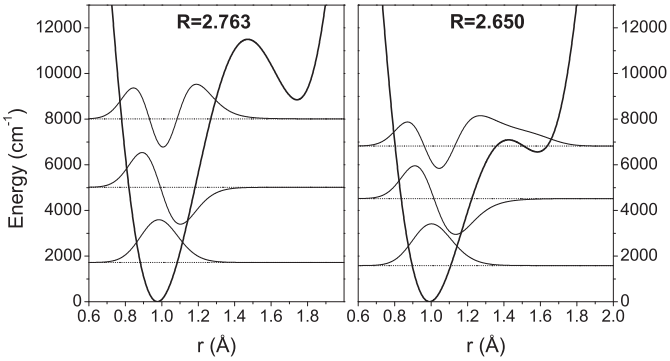

FIGURE 7.1. Lippincott-Schröder potential and wave functions for the O–H stretch coordinate r. The potential has the form of an asymmetric double well, for which the high energy minimum refers to a proton transferred state by formation of a hydronium-hydroxide ion pair. The left panel shows the potential for the equilibrium O···O hydrogen bond length of an ice crystal at 180 K (R=2.763Å). The right panel shows the potential for a shortened hydrogen bond (R=2.650Å), for which the wave function is delocalised over the two wells.

and hydrogen bonding properties of ice-Ih are only seemingly simple topics, and have been puzzling physicists and chemists for a long time. Although a proton or deuteron is found along every O···O line in an ice crystal, the individual hydrogen bonds and covalent bonds are positioned randomly under constraints known as "ice-rules" [98]. The ice lattice is therefore said to be proton disordered. Combined theoretical and experimental scattering studies on ice *Ih* show that, as a result of proton disorder, individual water molecules deviate from their lattice sites by static displacements of the oxygen positions [72, 73, 107]. From a spectroscopic point of view, it was suggested that proton disorder should lead to inhomogeneous broadening of the linear O–H stretch spectrum in HDO:D_2O [15].

The inhomogeneous broadening of the O–H stretch absorption in HDO:D_2O ice was confirmed by the first ultrafast spectroscopic study on ice, using ps-IR pump probe spectroscopy [113]. This work also showed that the $v_{\mathrm{OH}} = 1 \rightarrow 2$ transition of ice is strongly broadened compared the narrow $v_{\mathrm{OH}} = 0 \rightarrow 1$ transition. While the $v_{\mathrm{OH}} = 0 \rightarrow 1$ transition has a full width at half maximum (FWHM) of only 50 cm^{-1} at 180 K, the $v_{\mathrm{OH}} = 1 \rightarrow 2$ transition has a width of 350 cm^{-1}. Theoretical modelling of the (linear) $v_{\mathrm{OH}} = 0 \rightarrow 1$ absorption spectrum of ice still is an ongoing field of research [22, 129]. To understand the non-linear pump-probe spectrum, we need additional understanding of the $v_{\mathrm{OH}} = 1 \rightarrow 2$ absorption spectrum.

The line shape of the $v_{\mathrm{OH}} = 1 \rightarrow 2$ transition is of importance, since it

may contain information on the O–H stretch potential of a hydrogen-bonded water molecule. This potential is usually described as an asymmetric double well potential with a barrier height being dependent on the precise length of the hydrogen bond R [6, 15, 55, 82], as illustrated in Fig. 7.1. The high energy minimum in the potential refers to the state in which a water molecule has undergone auto-dissociation forming a hydronium-hydroxide ion pair. The precise barrier height between the two states is strongly dependent on the hydrogen-bond coordinate R. As will be discussed, the $v_{\mathrm{OH}} = 1 \rightarrow 2$ transition can strongly broaden as soon as the $v_{\mathrm{OH}} = 2$ state becomes close in energy to the dissociation barrier.

In this chapter we report on spectrally resolved sub-ps mid-infrared experiments on HDO:D_2O ice *Ih*. The experiments characterise the vibrational relaxation pathway and the transient absorption line shape. The transient line shape is analysed within a Lippincott-Schröder model (LS-model), which allows us to identify the main broadening mechanism for the $v_{\mathrm{OH}} = 1 \rightarrow 2$ transition.

7.2 Materials and Methods

We performed ultrafast mid-infrared pump-probe spectroscopy on the O–H stretch vibration of diluted HDO in D_2O at 180 K. Isotopically diluted water samples (1:40 H_2O:D_2O) are used to prevent the signals to be affected by intermolecular resonant energy transfer of the O–H stretch vibrations, and to limit heating of the sample. Water was inserted between two CaF_2 windows without spacer and inserted into a closed cycle cryostat (CTI-Cryogenics). The sample was cooled to 180 K. The linear absorption is found to be isotropic for all polarisation angles, which shows that the sample is polycrystalline with crystalline domains much smaller than the laser focus. No local order or dipole alignment is present in the sample.

In the pump-probe experiment the pump and probe beams are overlapped and focussed at the sample inside the cryostat. The transmitted probe beam is sent through a polariser and spectrally resolved on a nitrogen-cooled HgCdTe detector array using a polychromator. Using an automated rotatable mount, the polariser can be set either parallel or perpendicular with respect to the pump polarisation, and at each delay point both probe components are detected consecutively. In this way, pump-induced transmission changes for both the probe component polarised parallel ($\Delta\alpha_{\parallel}$) and perpendicular ($\Delta\alpha_{\perp}$) with respect to the pump polarisation are measured, from which we construct the rotation-free signal $\Delta\alpha_{RF}(\omega, t)$ and the anisotropy parameter $R(\omega, t)$ as described in chapter 1.

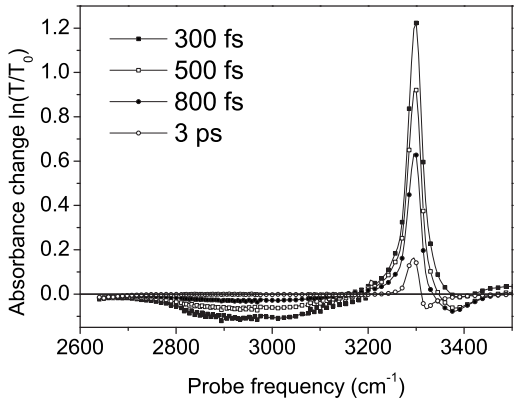

FIGURE 7.2. Pump induced absorbance change plotted as a function of probe frequency at probe delay t of 0.3, 0.5, 0.8 and 3 ps. The negative induced absorption signal is strongly broadened compared to the positive bleaching signal.

7.3 Relaxation dynamics of vibrationally excited ice

Fig. 7.2 shows the transient absorption of HDO ice (H_2O:D_2O=1:40) at several delays after vibrational excitation by the pump pulse. The transient line shape consists mainly of a narrow bleaching peak at the O–H stretch absorption around 3300 cm^{-1}, and a very broad induced absorption around 3000 cm^{-1}. This large difference in line width was previously observed by ps ir hole-burning spectroscopy [113], the induced absorption peak being over a factor of 5 broader than the bleaching contribution.

We determine the O–H stretch vibrational relaxation rate by measuring the decay of the induced absorption in time. The spectral region of the induced absorption (2800-3200 cm^{-1}) contains no other absorbing species, making the signal solely proportional to the population of the $v_{OH} = 1$ vibrational state. In agreement with previous work [133], we find that at all frequencies the induced absorption decays mono-exponentially with a time constant of 420±20 fs.

Interestingly, the induced bleaching around 3300 cm^{-1} decays differently than the induced absorption around 3000 cm^{-1}. This is illustrated in Fig. 7.3, in which the transient absorbance change at the peak of the bleaching is compared with the decay of the induced absorption. Both curves are scaled to equal amplitude and sign to facilitate easy comparison of the dynamics. The figure clearly shows that the sharp bleaching feature around 3300 cm^{-1} decays at about half the rate of the induced absorption.

A more careful examination of the transients shown in Fig. 7.2 shows addi-

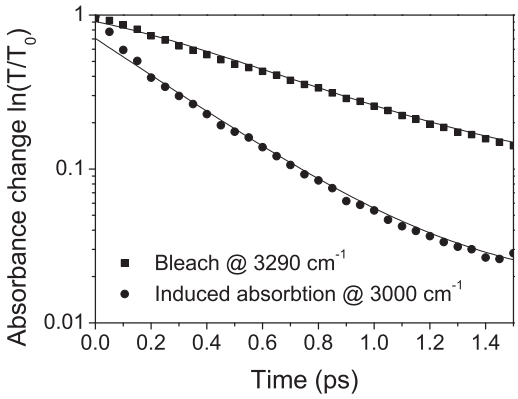

FIGURE 7.3. Pump induced absorbance change plotted as a function of probe delay at 3290 cm^{-1} (centre frequency bleaching) and 3000 cm^{-1} (centre frequency induced absorption). Both curves are scaled to equal amplitude and sign to facilitate comparison of the dynamics. The relaxation is faster for the induced absorption than for the bleaching.

tional spectral dynamics, namely the appearance at about 400 fs of an induced absorption around 3380 cm^{-1}. At later delays, the transient spectrum takes the form of a thermal difference spectrum, which also results in induced absorption, however at 3320 cm^{-1}. This thermal signal $\Delta\alpha_{\mathrm{T}}(\omega, t)$ arises from effects of heating of the sample due to the intense pump pulse, i.e. the effect on the O–H stretch absorption of population of low-frequency modes after vibrational relaxation [105].

We find that the induced absorption at 3380 cm^{-1} grows in at a rate that equals the vibrational relaxation, and disappears when also the relatively slow decay of the bleaching at 3300 cm^{-1} is complete. These corresponding timescales suggest that both the absorption at 3380 cm^{-1} and the longer lifetime of the bleaching at 3300 cm^{-1} arise from the same effect, namely that the vibrational relaxation proceeds via an intermediate state.

To determine the spectral signature of this intermediate state we fit the data to a simple kinetic model, as illustrated in Fig. 7.4. State 0 comprises the thermal ground state of the water molecules, state 1 represents the thermal ground state 0 plus one quantum in the O–H stretch coordinate. Vibrational relaxation from the initially populated state 1 proceeds via a non-thermal intermediate level 0^* with a different associated cross-section [a]. The total rotation-free

[a]For ice the transition from the non-thermal intermediate level has a *different* associated cross-section than the fundamental transition ($\sigma^*_{01}(\omega, t) \neq \sigma_{01}(\omega, t)$). This is different from the case of HDO:D_2O water [106] and water in micelles (see chapter 5) where these transitions have equal associated cross-sections ($\sigma^*_{01}(\omega, t) = \sigma_{01}(\omega, t)$).

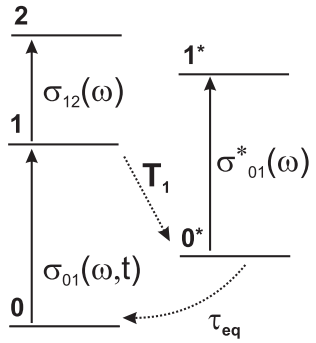

FIGURE 7.4. Schematic overview of the model that describes the population dynamics of excited HDO molecules. Relaxation from the excited $v_{\mathrm{OH}} = 1$ state proceeds via an intermediate level 0^* with associated O–H stretch cross section $\sigma^*_{01}(\omega)$ that is different from the cross section $\sigma_{01}(\omega, t)$ in the ground state.

pump-probe signal $\Delta\alpha(\omega, t)$ can be written in terms of the populations N_1, N_0^* of the levels in Fig. 7.4 of the initially excited molecules only, the absorption cross-sections σ between these levels, and the total concentration of absorbing molecules C [105]:

$$\Delta\alpha(\omega, t) \propto \Delta\sigma_{\mathrm{PP}}(\omega)N_1(t) + \Delta\sigma_{01^*}(\omega)N_{0^*}(t) + \Delta\alpha_{\mathrm{T}}(\omega, t), \tag{7.1}$$

$$\begin{aligned} \Delta\sigma_{\mathrm{PP}}(\omega) &= \big[\sigma_{12}(\omega) - 2\sigma_{01}(\omega, 0)\big], \\ \Delta\sigma_{01^*}(\omega) &= \big[\sigma^*_{01}(\omega) - \sigma_{01}(\omega, 0)\big], \\ \Delta\alpha_{\mathrm{T}}(\omega, t) &= C\big[\sigma_{01}(\omega, t) - \sigma_{01}(\omega, 0)\big]. \end{aligned} \tag{7.2}$$

The time dependencies of the populations and $\Delta\alpha_{\mathrm{T}}$ are described in Appendix A. Fitting our data to the kinetic model gives the spectra $\Delta\sigma_{\mathrm{PP}}(\omega)$ and $\Delta\sigma_{01^*}(\omega)$ and the lifetime of the intermediate level τ_{eq}, which is found to be 390±40 fs. Fig. 7.5 shows the fitted curves overlayed with the measured data for five frequencies up to 3 ps.

In Fig. 7.6 the spectra $\Delta\sigma_{\mathrm{PP}}(\omega)$ and $\Delta\sigma_{01^*}(\omega)$ are shown. $\Delta\sigma_{\mathrm{PP}}(\omega)$ equals the pure pump-probe line shape at time $t = 0$, before any vibrational relaxation has occurred. We find a FWHM of the bleaching line of 44 cm^{-1}, and 300 cm^{-1} for the induced absorption. $\Delta\sigma_{01^*}(\omega)$ is the pump-probe spectrum associated with the intermediate level.

An important question regarding the nature of the intermediate level, is whether the intermediate state absorption is solely due to molecules that were excited, or that also non-excited molecules contribute to the intermediate state absorption. In the first case vibrational relaxation leads to population of modes localised near the excited OH-group that change its O–H stretch absorption frequency, in the latter case vibrational relaxation populates delocalised modes

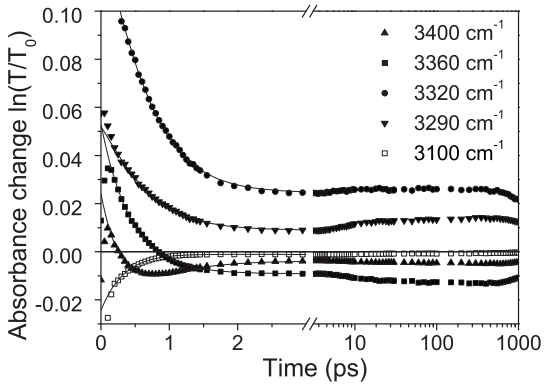

FIGURE 7.5. Pump induced absorbance change plotted as a function of probe delay at various probe frequencies. From 3 ps onwards absorbance changes are observed related to slow collective rearrangements of the hydrogen bonded crystal lattice. Note that the probe delay is plotted on a linear scale up to 3 ps and on a logarithmic scale after 3 ps.

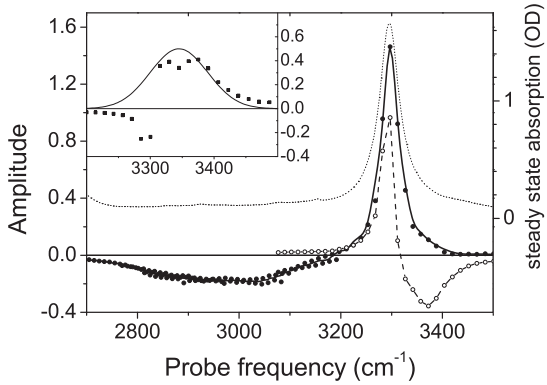

FIGURE 7.6. Pure pump-probe spectrum $\Delta\sigma_{\mathrm{PP}}(\omega)$ (●, solid line), intermediate state pump-probe spectrum $\Delta\sigma_{0^*}(\omega)$ (○, dashed line). For comparison, the linear O–H stretch absorption spectrum of isotopically diluted (1:40) ice at 180 K is shown (dotted line). Since the probe spectrum is not broad enough to cover the full spectral range of interest, the displayed data result from merging three spectra measured separately with the probe-wavelength centred at 2800, 3000 and 3300 cm^{-1}. The inset shows the extracted linear absorption of the intermediate state σ_{0^*}.

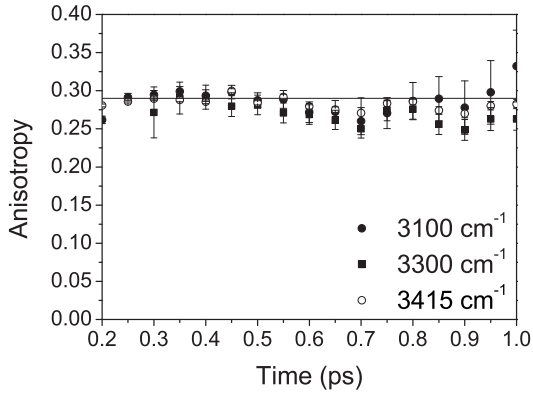

FIGURE 7.7. Anisotropy decay at various probe frequencies. We observe no significant decay of the anisotropy within the first 1 ps. At the probe frequency of 3415 cm^{-1} (○) only the intermediate state absorbs. The intermediate state anisotropy equals that of the bleaching (■) and induced absorption (●) contributions.

that affect the O–H stretch absorption frequencies of several molecules, including molecules that were not excited.

We can distinguish between these two cases by examining the anisotropic signal, as displayed in Fig. 7.7. In the spectral region of the broad induced absorption the intermediate state has no cross-section, and we measure only the anisotropy value of the molecules of which the O–H stretch vibration is excited. Within the accuracy of our experiment, this anisotropy is shown to retain a constant value of 0.3. This value is somewhat lower than the expected value of 0.4, probably because of scattering of the pump and probe light. The constant value shows that during vibrational excitation the O–H stretch transition dipole in the first excited state does not change orientation, as expected for a rigid crystalline structure as ice. In spectral regions where also the intermediate state has significant cross-section, we measure the exact same anisotropy, even when most population has been transferred to the intermediate level from 500 fs onwards. The transition dipole of the intermediate state absorption therefore has to be parallel to the transition dipole of the initial state, since otherwise the anisotropy of the intermediate state would have been lower. This demonstrates that the intermediate state absorption originates from spectral changes of the excited molecules only, following their vibrational relaxation, and is likely related to intramolecular relaxation. To obtain the linear absorption spectrum of molecules in the intermediate state $\sigma^*_{01}(\omega)$, we add the linear absorption spectrum of molecules in the ground state $\sigma_{01}(\omega)$ to the intermediate state pump-probe spectrum $\Delta\sigma_{01^*}(\omega)$ with the correct proportionality constant (see Eq. 7.1). If we assume that $\sigma_{12}(\omega)$ has little absorption above 3200 cm^{-1} we

can write $\sigma^*_{01}(\omega) = \Delta\sigma_{01^*}(\omega) - \frac{1}{2}\Delta\sigma_{\mathrm{PP}}(\omega)$ for $\omega > 3200$ cm^{-1}. The intermediate state spectrum obtained in this way is shown in the inset of Fig. 7.6.

Compared to the initial state, the intermediate state absorption is broader with a FWHM of 100±20 cm^{-1} and blue shifted to 3350±20 cm^{-1}. This blue shift can result both from intramolecular relaxation to the bending mode and from relaxation to local hydrogen bond modes. Excitation of the bending vibration dynamically decouples the O–H stretch motion from the hydrogen bond, resulting in hydrogen bond weakening and a blue shift of the O–H stretch frequency. Recently, a blue shifted intermediate state associated with the excitation of a bending quantum was also reported for liquid water [80]. The vibrational lifetime of the HDO bend vibration for liquid HDO:D_2O was recently measured to be 390±50 fs [17]. This life time agrees very well with the intermediate state life time τ_{eq}, which supports the assignment of the intermediate state to the O–H stretch absorption of water molecules of which the H–O–D bending vibration is excited. The O–H stretch absorption spectrum is also known to blue-shift as a result of an increasing temperature, which is predominantly caused by the weakening of the hydrogen bonds. A local temperature rise by about 200 K can be achieved by the energy of one relaxed vibrational quantum (calculated from molecular density and specific heat, in the limit where the energy is shared by one HDO molecule and its four next neighbours only) [113].

As a final point of interest, the thermal pump-probe spectrum $\Delta\alpha_T(\omega, t)$ shows some remarkable dynamics over longer timescales, as displayed in Fig. 7.5. The dynamics has multi-exponential character, as is often observed for processes involving heat diffusion. The strongest increase in the thermal signal is observed from 3-40 ps (exponential time constant 5±1 ps). Further small signal increases are observed up to 100-400 ps, after which the thermal signal starts to decay as a result of cooling.

In the context of super-heating experiments of ice reported in literature, it has been suggested that these slow dynamics are related to partial melting of the ice-lattice [60]. In our experiment a melting process is however not likely to occur. The amount of heat dumped in the sample is very limited in view of the low concentration of O–H stretch absorbers, causing the sample to be heated by a few degrees Kelvin only after completion of the vibrational relaxation of the intermediate state. The longer time scale dynamics are likely caused by collective reorganisation of the ice lattice (e.g. thermal expansion). Since these dynamics involve very low frequency modes in the hydrogen bond coordinates, the thermal equilibrium positions for these coordinates are reached fairly slowly. Cooling of the focal region to the surrounding temperature will cause the thermal signal to decay entirely eventually, as seen from 400 ps onwards.

7.4 Absorption line shape of vibrationally excited ice

7.4.1 O–H stretch frequency dependence of the hydrogen bond

A striking feature of the pure pump-probe spectrum $\Delta\sigma_{\mathrm{PP}}(\omega)$ of ice, is the huge difference in line width between the $v_{\mathrm{OH}} = 1 \rightarrow 2$ and $v_{\mathrm{OH}} = 0 \rightarrow 1$ transitions. A possible explanation for the huge width of the $v_{\mathrm{OH}} = 1 \rightarrow 2$ can be found from the effect of the hydrogen bond on the O–H stretch vibrational potential. This O–H stretch vibrational potential is usually described as an asymmetric double well potential with a barrier height being dependent on the precise length of the hydrogen bond R [15, 55, 82].

We describe the relation between O–H stretch frequency and hydrogen bond length by a Lippincott-Schröder model [82], which has been applied successfully in the description of the transient spectrum of liquid water [6,7]. The Lippincott-Schröder (LS) potential for the O–H coordinate of the water molecule is given by

$$V_{\mathrm{LS}}(r,R) = D_a[1 - e^{-n_a(r-r_0)^2/2r}] + D_b[1 - e^{-n_b(R-r-r_0)^2/2(R-r)}] + V_0(r,R), \tag{7.3}$$

where $V_0(r,R)$ is a potential term that puts the absolute minimum of the full potential at 0 for all (r,R). The energy D_a equals the O–H binding energy of water of 38750 cm^{-1}(4.8 eV). r_0 represents the O–H bond length in the gas phase in the absence of a hydrogen bond (0.97 Å). Parameters n_b (16.5$\mathrm{Å}^{-1}$) and D_b (25000 cm^{-1}) are determined by the relations between the O–H bond length r, the O–H stretch vibrational frequency and the oxygen–oxygen distance R [7,82]. The values of the parameters of $V_{\mathrm{LS}}(r,R)$ are equal to those used previously in the description of the transient spectrum of liquid water [7], except for the parameter n_a (10.0 $\mathrm{Å}^{-1}$), which was slightly upscaled to yield the correct central O–H stretch absorption frequency at 180 K (3290 cm^{-1}) at the experimentally determined equilibrium hydrogen-bond length of 2.76 Å [73].

The LS-potential is illustrated in Fig. 7.1. The low energy minimum refers to the normal hydrogen bonded configuration of the water molecule. The high energy minimum refers to the configuration in which the hydrogen bond donating water molecule has undergone autodissociation, forming a hydroxide and hydronium ion pair by a proton transfer event to the neighbouring water molecule. For strong (short) hydrogen bonds, the energy barrier between these two configurations gets substantially lowered. When the barrier height is of the order of the energy of the $v_{\mathrm{OH}} = 2$ state of the O–H stretching vibration, the vibrational wave function gets delocalised over the two wells, reflecting the possibility of proton transfer. The precise energy of the vibrational state will be highly sensitive to the precise height of the energy barrier and thus to the hydrogen-bond coordinate. In other words, small variations in R can give a large spread in $v_{\mathrm{OH}} = 2$ vibrational energies, and therefore lead to a significant

broadening of the $v_{\mathrm{OH}} = 1 \rightarrow 2$ absorption. This mechanism has been shown to adequately explain the line shape of vibrationally excited liquid water [6, 7]. We will test whether a similar mechanism can explain the huge broadening of the $v_{\mathrm{OH}} = 1 \rightarrow 2$ transition in ice.

We will estimate the distribution in hydrogen bond lengths of an ice *Ih* crystal at 180 K, and how these hydrogen bonds will be partly modulated in time by the presence of low-frequency phonons (sec. 7.4.2). With these ingredients we can calculate the dipole time correlation functions (sec. 7.4.3) that determine the ground state and excited state absorptions. Finally we discuss the transient absorption line shapes resulting from these calculations (sec. 7.4.4).

7.4.2 Hydrogen bond distribution and dynamics

The line width of the $v_{\mathrm{OH}} = 0 \rightarrow 1$ transition equals 50 cm^{-1} at 180 K. This line width cannot be explained from the lifetime of the $v_{\mathrm{OH}} = 1$ state ($T_1^{v=1} = 0.42$ ps). Lifetime broadening leads to a Lorentzian absorption profile for each oscillator, the FWHM line width being only 13 cm^{-1} ($1/(2\pi T_1^{v=1})$). The O–H stretch line width must therefore be additionally broadened by the dynamics and the spread in length of the hydrogen bonds that occur in the ice crystal. To calculate the transient line shape, we need to know this hydrogen bond dynamics and length distribution. We can then relate these to O–H stretch frequencies and cross-sections by the LS-model as shown in the previous paragraph.

Proton disorder in the ice crystal leads to a static spread in oxygen positions in the ice lattice, even at low temperatures. Therefore a static spread $\Delta_{R,\mathrm{stat}}$ in the O$\cdots$O hydrogen bond lengths R exists in the ice lattice, which is unfortunately very difficult to deduce from experimental scattering studies [73]. This static distribution in hydrogen bond lengths will determine the inhomogeneous broadening of the ice O–H stretch absorption. Picosecond IR hole-burning experiments reported some inhomogeneous broadening of the O–H stretch band, however only with a very narrow distribution (spectral holes were separated by at most 15 cm^{-1}, corresponding to a standard deviation in hydrogen bond lengths of $\sim$0.4 pm in our LS-model [113], which is small compared to the standard deviation of 1.5 pm of room temperature liquid water [7]). A recent theoretical study [73] also shows a very small standard deviation of 0.7 pm. We therefore assume in our calculation a gaussian hydrogen bond distribution $f_{\mathrm{stat}}(R)$ of fixed standard deviation $\Delta_{R,\mathrm{stat}}$=0.4 pm around equilibrium bond length R_0=2.76 Å. Within the LS-model, this hydrogen bond distribution leads to a FWHM O–H stretch $v_{\mathrm{OH}} = 0 \rightarrow 1$ line width of only 20 cm^{-1}. This is much narrower than the experimentally measured line width of 50 cm^{-1} at 180 K, for which proton disorder alone can therefore not account.

Another line broadening mechanism results from lattice dynamics that modulate the O$\cdots$O hydrogen bond [110], and thereby the O–H stretch frequency. Thermally excited phonons will modulate the hydrogen bond coordinate by a certain amplitude and at a characteristic timescale. In our model we will assume that the presence of phonons will lead to a diffusional modulation of the hydrogen bond coordinate (See Appendix B). As a result we do not model cer-

tain phonon satellite band progressions that are observed in the O–H stretch spectrum of isotopically dilute ice [44]. These are associated with combined transitions to higher energy underdamped non-thermal phonons.

We need to make assumptions about the amplitude and rate of the hydrogen bond fluctuations. The amplitude of the fluctuations are related to phonon amplitudes, which are typically smaller than 2 pm [20]. This puts an upper limit to the width $\Delta_{R,\mathrm{dyn}}$ of the hydrogen bond distribution that is dynamically sampled by the hydrogen bond length fluctuations. The rate of the fluctuations is set by a diffusional constant for the hydrogen bond length modulation process. This diffusional constant D is directly related to the decay constant τ_c of the frequency correlations (see Eq. 7.19). We assume that $\tau_\mathrm{c} \gtrsim h/(k_B T) = 0.27$ ps, i.e. the frequency correlations cannot decay faster than the oscillation period of the average occupied thermal mode. We choose $\Delta_{R,\mathrm{dyn}}$=1 pm, and adjust the diffusion constant D by a fit of the calculated line shape to the experimental spectrum (see Sec. 7.4.4). This results in D=30 pm^2/ps and τ_c=0.3 ps.

7.4.3 Line shape calculation

Following the Wiener–Khintchine theorem (Eq. 2.13), the absorption spectrum for a transition from state $i \rightarrow j$ is the Fourier transform of the dipole time correlation function:

$$S_{ij}(\omega) = \frac{1}{2\pi} \int_{-\infty}^{\infty} dt \cdot e^{-i\omega t} C_{ij}(t). \tag{7.4}$$

We use Eq. 2.24 to calculate of the dipole time correlation function so that $C_{ij}(t) = \left\langle \widetilde{\mu}_{ij}(0) \widetilde{\mu}_{ij}(t) F_\mathrm{c}(t) \right\rangle$, where $\widetilde{\mu}_{ij}(t)$ is the amplitude of the transition dipole, $F_\mathrm{c}(t)$ is the dephasing function and $\langle \ \ \rangle$ denotes ensemble averaging over all oscillators [71].

The correlation function is determined by the time-evolution of the dipole moments, which is given by the transition frequencies, transitions dipole moments and the vibrational lifetimes of the involved states. The transition frequencies and transition dipole moments depend on the hydrogen bond coordinate R as calculated in Appendix B. The spread and dynamics of the hydrogen bond coordinate R was discussed in the previous section.

We assume that the pump and probe pulses are short compared to the system dynamics (impulsive pump-probe (IPP) limit [90]), and take the excited state and ground state dynamics fully uncorrelated and in thermal equilibrium. We treat the vibrational state spectrum of water as a near-harmonic three-level system. In that case only $\widetilde{\mu}_{01}$ and $\widetilde{\mu}_{12}$ have significant amplitude. The pump probe signal at zero probe delay $S_\mathrm{IPP}(\omega, 0)$ can then be related to the linear response of Eq. 7.4 by

$$S_\mathrm{IPP}(\omega, 0) \propto 2S_{01}(\omega) - S_{12}(\omega), \tag{7.5}$$

referring to the bleaching and induced absorption contributions, respectively. The line shape calculation is described in detail in Appendix B.

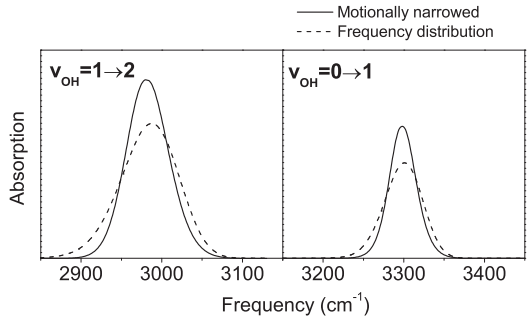

FIGURE 7.8. Absorption line shapes for the $v_{\rm OH} = 1 \rightarrow 2$ and the $v_{\rm OH} = 0 \rightarrow 1$ transition (solid lines) calculated when assuming a frequency distribution (dotted lines) for a Gaussian hydrogen bond length distribution of standard deviation $\Delta_{R,\rm dyn}$=1 pm (i.e. excluding inhomogeneous and lifetime broadening).

7.4.4 Discussion of the calculated transient lineshapes

In Fig. 7.8 the calculated line shapes for the $v_{\rm OH} = 1 \rightarrow 2$ and the $v_{\rm OH} = 0 \rightarrow 1$ transition (solid lines) are shown when assuming a frequency distribution for a Gaussian hydrogen bond length distribution of standard deviation $\Delta_{R,\rm dyn}$=1 pm and a mean of R_0=2.76 Å (dotted lines). The hydrogen bonds diffuse with a diffusional constant D=30 pm^2/ps (see Appendix B), and lifetime broadening is not included by taking the vibrational lifetimes infinite.

The frequency modulations due to phonons clearly result in motional narrowing of the spectral lines. The degree of motional narrowing is similar for the $v_{\rm OH} = 0 \rightarrow 1$ and $v_{\rm OH} = 1 \rightarrow 2$ absorptions.

By including inhomogeneous broadening and life-time broadening in the calculation, we can calculate the full transient absorption line shape according to Eq. 7.5. The only remaining adjustable parameter is the vibrational lifetime $T_1^{v=2}$ of the $v_{\rm OH} = 2$ state. In Fig. 7.9 (dotted line) the line shape is calculated when $T_1^{v=2}$=$T_1^{v=1}/2$ (as would be expected for a harmonic oscillator, based on the larger dipole coupling matrix element between the $v_{\rm OH}$=1,2 states compared to the $v_{\rm OH}$=0,1 states). While the calculated line shape is reasonable for the $v_{\rm OH} = 0 \rightarrow 1$ transition, it gives a poor description of the experimentally measured $v_{\rm OH} = 1 \rightarrow 2$ absorption line shape.

We conclude that under the assumption that $T_1^{v=2} = T_1^{v=1}/2$, the LS-model cannot give a proper description of the $v_{\rm OH} = 1 \rightarrow 2$ absorption line shape. The LS-model can only give rise to strong line broadening for this transition, when the $v_{\rm OH} = 2$ energy is close to the top of the water autodissociation barrier. We find however that this is only the case for relatively short hydrogen bonds (R$\sim$2.65Å), that do not occur in ice (R$\sim$2.76$\pm$0.1Å).

We have tried to find different parameterisations of the LS-potential (Eq. 7.3)

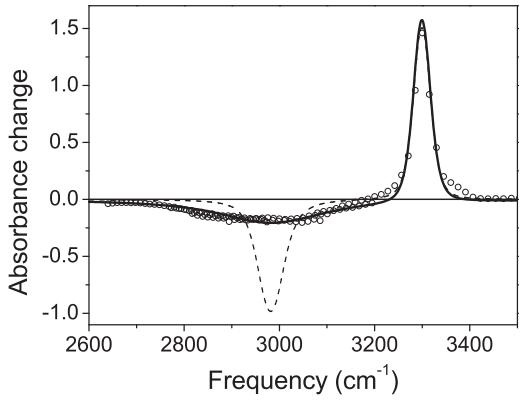

FIGURE 7.9. Experimental (○) and calculated transient line shapes. Dashed line: calculated transient line shape when the vibrational lifetime of the $v_{\mathrm{OH}} = 2$ state $T_1^{v=2}$=$T_1^{v=1}/2$=210 fs (as would be expected for an approximately harmonic oscillator). Solid line: Best fit between experiment and calculation, obtained by assuming a vibrational lifetime of the $v_{\mathrm{OH}} = 2$ state of $T_1^{v=2}$=20 fs.

that would lower the top of the water autodissociation barrier, and bring it closer to the $v_{\mathrm{OH}} = 2$ energy of longer hydrogen bonds. We found however that lowering the barrier unavoidably implies a strong increase of the anharmonicity of the O–H stretch vibration. This results in $v_{\mathrm{OH}} = 1 \rightarrow 2$ transition frequencies that are far too red-shifted compared to the experimental observations. A low anharmonicity of the O–H stretch potential of ice is also in line with the value for the O–H stretch overtone absorption (6300 cm^{-1}) [55].

This leaves us with the remaining possibility that the broad $v_{\mathrm{OH}} = 1 \rightarrow 2$ line shape is determined primarily by a very short lifetime of the $v_{\mathrm{OH}} = 2$ vibrational state, i.e. $T_1^{v=2} \ll T_1^{v=1}/2$. We find good agreement between the experimental and calculated transient spectrum when $T_1^{v=2} \approx T_1^{v=1}/20$, making $T_1^{v=2}$ only 20±4 fs, as illustrated in Fig. 7.9. An explanation for this very short lifetime of the $v_{\mathrm{OH}} = 2$ vibrational state can be found in the resonance of the $v_{\mathrm{OH}} = 1 \rightarrow 2$ transition with the overtone of the bending vibration. This allows for very fast energy redistribution from the $v_{\mathrm{OH}} = 2$ vibrational state.

7.5 Comparison with liquid water

We have shown that the relaxation of the O–H stretch vibration of HDO:D_2O ice proceeds via an intermediate state with a blue-shifted absorption. A similar intermediate state is present in the vibrational relaxation pathway of liquid water [80]. For liquid H_2O the full spectrum of the intermediate state is hard to

observe, because it is dominated by the pure pump-probe and heating signals ($\Delta\sigma_{\mathrm{PP}}$ and $\Delta\alpha_{\mathrm{T}}$, resp.). For HDO:$D_2O$ ice the intermediate state absorption can be observed more clearly, because it appears spectrally separated, and because the heating effect is less pronounced.

We would like to comment on why proton delocalisation can explain the broadening of the induced absorption in the case of liquid water, but not in the case of ice. This relates mainly to the very different hydrogen-bond distributions that occur in ice and water. Ice is highly ordered and a hydrogen-bond length variation of only 2.759-2.767Å is present [73]. The liquid phase of water contains much more disorder, showing a spread of 2.6-2.9Å [7]. Therefore, very short hydrogen bonds occur in water, for which the LS-potential allows the proton to delocalise in the $v_{\mathrm{OH}} = 2$ state. This qualitative difference in short and long hydrogen bonds makes the induced absorption of water very asymmetric. In the case of ice, the induced absorption line shape is determined by the lifetime, and its absorption is therefore very symmetric. For several reasons the $v_{\mathrm{OH}} = 1 \rightarrow 2$ transition line width in water is expected to be less dominated by lifetime broadening. The lifetime of the $\nu_{\mathrm{OH}} = 1$ state in water is much longer than in ice (740 fs). Therefore the lifetime of the $v_{\mathrm{OH}} = 2$ state in water will likely be longer as well. Most importantly, a longer $v_{\mathrm{OH}} = 2$ lifetime is expected for HDO:D_2O water than for HDO:D_2O ice, since the H–O–D bending overtone is no longer in complete Fermi resonance with the O–H stretch vibration.

It is remarkable that very slow (>100 ps) thermal dynamics is observed in ice but not in liquid water. The O–H stretch absorption in ice is much sharper than in water, which makes thermal signals (usually related to small frequency shifts and cross-section changes) relatively stronger. The amplitude of a signal resulting from a thermally induced frequency shift δ of a gaussian band of width μ scales as δ/μ^2, thus quadratically decreasing with the line width. Because the fundamental water O–H stretch absorption is 4-5 times broader than the fundamental ice O–H stretch absorption, thermal effects are 20 times weaker (assuming similar thermally induced frequency shifts). Absorption lines in the liquid phase that are equally narrow as the O–H stretch line in HDO:D_2O ice, have also been found to show long-timescale thermal dynamics [18], similar to the slow dynamics reported here for ice.

7.6 Conclusions

We find that the vibrational relaxation of ice proceeds via an intermediate state, which has a blue-shifted absorption by 50±20 cm^{-1}. The intermediate likely corresponds to the O–H stretch absorption of water molecules of which the H–O–D bending vibration is excited, as a result of vibrational relaxation. By fitting the data to a kinetic model, we can separate the pure pump-probe spectrum from the response of the intermediate state. We find the vibrational lifetime of ice to be 420±30 fs, in accordance with earlier studies [133], and the lifetime of the intermediate state to be 390±40 fs.

We observe thermally induced absorption changes of the O–H stretch mode,

that evolve on a timescale of tens to hundreds of ps. These transmission changes likely relate to collective reorganisations of the ice lattice in response to heating.

A striking feature of the pure pump-probe spectrum of ice is the strongly broadened $v_{\mathrm{OH}} = 1 \rightarrow 2$ transition. Such broadening was also observed for liquid water, and could be explained from proton delocalisation in the $v_{\mathrm{OH}} = 2$ state [6, 7]. We modelled the $v_{\mathrm{OH}} = 0 \rightarrow 1$ and $v_{\mathrm{OH}} = 1 \rightarrow 2$ line shapes of ice using the Lippincott-Schröder model for the O–H stretch potential. Using this model, we find that proton delocalisation cannot occur in the $v_{\mathrm{OH}} = 2$ vibrational state of ice. Delocalisation occurs only for fairly short (strong) hydrogen bonds that are not present in the ice crystal. Proton delocalisation therefore does not contribute to the observed broadening of the induced absorption.

We find that the strong broadening of the induced absorption follows from a very short vibrational lifetime of the $v_{\mathrm{OH}} = 2$ state ($T_1^{v=2}$=20±4 fs). This short lifetime can be explained from the resonance of the $v_{\mathrm{OH}} = 1 \rightarrow 2$ transition with the overtone of the H–O–D bending vibration.

7.7 Appendix A: Kinetic Modelling

The following equations describe the dynamics of the molecules that were excited by the pump pulse:

$$\begin{aligned} \frac{dN_1}{dt} &= -\frac{1}{T_1} N_1, \\ \frac{dN_0^*}{dt} &= \frac{1}{T_1} N_1 - \frac{1}{\tau_{\mathrm{eq}}} N_0^*, \\ \frac{dN_0}{dt} &= \frac{1}{\tau_{\mathrm{eq}}} N_0^*. \end{aligned} \tag{7.6}$$

N_1, N_0^* and N_0 refer to the populations of the levels depicted in Fig. 7.4 (the population N_0 is defined as the population difference with respect to the steady-state population of this state). As boundary conditions we assume that at t=0 the number of molecules in the excited state equals the number of molecules removed from the ground state, $N_0(0) = -N_1(0)$, and $N_0^*(0) = 0$. We then find

$$\begin{aligned} N_1(t) &= N_1(0) e^{-t/T_1}, \\ N_{0^*}(t) &= N_1(0) \frac{\tau_{\mathrm{eq}}}{T_1 - \tau_{\mathrm{eq}}} (e^{-t/T_1} - e^{-t/\tau_{\mathrm{eq}}}). \end{aligned} \tag{7.7}$$

When the excited molecules relax to the ground state, the entire ice crystal gets gradually heated. Because of this heating, the O–H stretch cross-section spectrum ($\sigma_{01}(\omega, t)$) slightly blue-shifts, resulting in thermal absorption changes $\Delta\alpha_{\mathrm{T}}(\omega, t)$ observed in the experiments. We assume the change of the spectrum $\sigma_{01}(\omega, t)$ upon heating to be proportional to the total number of molecules N_{rel}

that have decayed to the ground state:

$$\begin{aligned}\Delta\alpha_T(\omega,t) &\propto N_{rel}(t) = \int_{t'=0}^{t} \frac{1}{\tau_{\rm eq}} N_0^*(t')dt' \\ &= N_1(0) - N_1(0)(\tau_{\rm eq}e^{-t/\tau_{\rm eq}} - T_1 e^{-t/T_1})/(\tau_{\rm eq} - T_1). \quad (7.8)\end{aligned}$$

Heating affects the cross-sections of all molecules, not only of the the initially excited number of molecules $N_1(0)$, as we implicitly assume above. It can be shown that taking into account the heating effect on all molecules in fact gives the same expression for $\Delta\alpha_{\rm T}$ as above provided the fraction of excited molecules $N_1(0)/C$ is small, which is the case in our experiment [105].

7.8 Appendix B: details line shape calculation

Assuming a classical fluctuating bath, the dipole time correlation function can be written as Eq. 2.25:

$$C_{ij}(t) = \left\langle u_{ij}(0)u_{ij}(t)\ m_{ij}(0)m_{ij}(t)\ e^{i\int_0^\tau \omega_{ij}(\tau)d\tau - \Gamma_{ij}t} \right\rangle, \quad (7.9)$$

where $m_{ij} = \langle i|M|j\rangle$ equals the magnitude of the transition dipole moment and u(t)=$\hat{\epsilon}\cdot\hat{M}$ as the molecular orientation, $\vec{M} = M\hat{M}$ the molecular dipole operator and $\hat{\epsilon}$ the laser field polarisation. In the above expression vibrational relaxation was introduced phenomenologically.[b]

The Γ_{ij} equal the dipole dephasing rates due to vibrational relaxation, which are given by

$$\Gamma_{01} = \frac{1}{2T_1^{v=1}}, \quad (7.10)$$

$$\Gamma_{12} = \frac{1}{2T_1^{v=1}} + \frac{1}{2T_1^{v=2}}. \quad (7.11)$$

$T_1^{v=j}$ equals the vibrational population decay time for vibrational state $|j\rangle$ (we write $2T_1$ since within the density matrix formalism, polarisations are proportional to coherences, which dephase due to vibrational relaxation at half the population relaxation rate of the corresponding excited state [19], see Eq. 2.52).

For ice we can neglect the effects of reorientation, and take $u_{ij}(t) = 1$. In our model, the dipole transition moments m_{ij} and frequencies ω_{ij} depend parametrically on the hydrogen-bond length R. Length modulations in R will result in time-dependent fluctuations of ω_{ij} and m_{ij}. We assume that the O–H stretch motion depends parametrically on the hydrogen bond stretch (O$\cdots$O) coordinate. This type of adiabatic approach is commonly used in describing the coupling between a high-frequency O–H stretch vibration and a low frequency

[b] To account for population relaxation we add to the real frequency ω_{eg} in Eq. 2.25 a complex quantity according to $\omega_{eg}(t) \rightarrow \omega_{eg}(t) - i\Gamma_{eg}$, which adds an exponentially decay to the dephasing function $F_{\rm c}(t)$ on a rate Γ_{eg}.

O–H$\cdots$O hydrogen bond. The approximation will be valid when the O$\cdots$O modulations are slow compared to the O–H stretch motion, which is a fairly reasonable assumption since the thermally excited phonon vibrations ($\sim$200 cm^{-1}) in ice are an order of magnitude slower in frequency than the O–H stretch vibrations ($\sim$3000 cm^{-1}) [24]. We solve the one-dimensional Schrödinger Equation for the LS-potential with a parametric dependence on the hydrogen bond coordinate R using a Numerov algorithm [67] (we adopt reduced units of energy (cm^{-1}), length (Å) and mass (m/$\hbar^2$), and take the reduced mass of an OH-oscillator equal to 0.0279 Å^{-2}/ cm^{-1}). This results in eigen energies E_v and eigenfunctions $|v\rangle$ up to $v_{\rm OH} = 2$ for each hydrogen bond coordinate R. The O–H stretch absorption frequency is given by the relation $\omega_{ij}(R) = (E_j - E_i)/\hbar$ and the absorption cross-sections m_{ij} are found by calculating the matrix elements $\langle i|r|j\rangle$ for each $v_{\rm OH} = i \rightarrow j$ transition.

Making explicit the ensemble average over the hydrogen-bond length distributions in Eq. 7.4, we have

$$C_{ij}(t) \quad = \quad \int_0^\infty dR' \cdot f_{\rm stat}(R') \int_0^\infty dR \cdot C_{ij}(R, R', t), \tag{7.12}$$

where

$$C_{ij}(R, R', t) \quad = \quad P_{ij}(R, R', 0)\ P_{ij}(R, R', t). \tag{7.13}$$

$P_{ij}(R, R', t)$ now equals a macroscopic time-dependent polarisation. The (R,R') hydrogen bond coordinates refer to the dynamic and static hydrogen bond distributions, as discussed in Sec. 7.4.2, i.e. $P_{ij}(R, R', t)$ is generated by the subset of oscillators that experience an instantaneous hydrogen-bond length R and have an equilibrium hydrogen-bond length R'. $P_{ij}(R, R', t)$ accumulates phase by a factor $e^{i\omega(R)t}$, but gains additional phase and changes amplitude as a result of the frequency modulations. The line shape calculation is now reduced to the calculation of the dipole time correlation functions $C_{ij}(R, R', t)$.

The length spread and dynamics of the hydrogen bonds in the ice crystal were discussed in Sec. 7.4.2. These are related to a frequency spread and modulation in O–H stretch frequencies by the LS-model. The inhomogeneous spread in hydrogen bonds $f_{\rm stat}(R')$ follows a Gaussian distribution of width $\Delta_{R,\rm stat}$=0.4 pm and mean R_0=2.76 Å. Around each hydrogen-bond length R' we centre a distribution of hydrogen bond lengths $f_{\rm dyn}(R, R')$, to account for the stochastic modulation of the hydrogen bonds by phonons. $f_{\rm dyn}(R, R')$ equals a Gaussian distribution of width $\Delta_{R,\rm dyn}$=1.0 pm and mean R'.

We rewrite the integrals in Eq. 7.12 as discrete summations over the variables (R,R'), adopting integration steps of length dR=1×10^{-13} m:

$$C_{ij}(t) = \sum_k \cdot f_{\rm stat}(R'_k) \sum_l C_{ij}(R_l, R'_k, t). \tag{7.14}$$

We assume that the pump and probe pulses are short compared to the system dynamics (impulsive pump-probe limit), and take the excited state and ground

state dynamics fully uncorrelated and in thermal equilibrium. We can then neglect cross-correlations between the different states in the third order response. We calculate the transient spectrum from the linear response for thermal equilibrium populations in both the ground and excited state.

For each transition $v_{\mathrm{OH}} = v - 1 \rightarrow v$, each bin l in Eq. 7.14 has an associated cross-section $m_{l,v}$ as calculated from the LS-model (this bin-associated transition dipole moment should not be confused with the earlier definition of the transition dipole moment m_{ij}, where the indices refer to vibrational states). The bins exchange population from bin l=m to l=n on a rate $k_{m,n}$ according to a diffusional process, to account for the stochastic stretching modulations of the hydrogen-bond length. Assuming constant diffusion over the entire distribution of hydrogen bonds ($(k_{m,m+1} + k_{m+1,m})/2 = k_0$), and using detailed balance $k_{m,m+1} \cdot f_{\mathrm{dyn}}(R_m, R'_k) = k_{m+1,m} \cdot f_{\mathrm{dyn}}(R_{m+1}, R'_k)$, the hop rates are given by

$$k_{m,n} = \begin{cases} k_0 \frac{2 f_{\mathrm{dyn}}(R_n, R'_k)}{f_{\mathrm{dyn}}(R_m, R'_k) + f_{\mathrm{dyn}}(R_n, R'_k)} & \text{if } n = m \pm 1, \\ 0 & \text{if } n \neq m \pm 1, \end{cases} \tag{7.15}$$

$$k_0 = \frac{D_{\mathrm{hop}}}{dR^2}, \tag{7.16}$$

where D_{hop} is the diffusion constant determining the rate of the stochastic hydrogen bond modulations.

For simplicity we will write the simple indices (l, k) for the discretised variables $(R_l,\ R'_k)$ and index v to denote the $v_{\mathrm{OH}} = v - 1 \rightarrow v$ transition. In each time step of the integration we keep track of the complex amplitude $P_{l,k,v}(t) \equiv P_{v-1\,v}(R_l, R'_k, t)$ of the polarisation associated with each bin l, according to

$$\begin{aligned} \frac{dP_{l,k,v}}{dt} &= \Big(i\omega_l - \Gamma_{v-1\,v} - k_{l,l+1} - k_{l,l-1}\Big) P_{l,k,v} \\ &\quad + k_{l+1,l} \frac{m_{l,v}}{m_{l+1,v}} P_{l+1,k,v} + k_{l-1,l} \frac{m_{l,v}}{m_{l-1,v}} P_{l-1,k,v}, \end{aligned} \tag{7.17}$$

$$P_{l,k,v}(0) = f_{\mathrm{dyn}}(R_l, R'_k) m_{l,v}. \tag{7.18}$$

$\Gamma_{v-1\,v}$ equals the polarisation decay due to vibrational relaxation (see Eq. 7.10). Eq. 7.17 consists of a system of l linear differential equations for each $v_{\mathrm{OH}} = v - 1 \rightarrow v$ transition and each hydrogen bond coordinate R'_k. This system is solved by numerical integration. The only remaining fit parameter is D_{hop}, which was adjusted to give the best description of the linear $v_{\mathrm{OH}} = 0 \rightarrow 1$ absorption ($D_{\mathrm{hop}} = 30$ pm^2/ps).

In the limit of a Gaussian hydrogen bond length distribution, a linear mapping between R and O–H stretch frequency, and a constant cross-section spectrum, D_{hop} is related to the frequency-frequency correlation time τ_{c} by [8, 25]

$$\tau_{\mathrm{c}} = \frac{dR^2}{D_{\mathrm{hop}}} \Big(1 - \sqrt{1 - 2\ dR^2/\Delta^2_{R,\mathrm{dyn}}}\Big)^{-1}, \tag{7.19}$$

$$\rightarrow \frac{\Delta^2_{R,\mathrm{dyn}}}{D_{\mathrm{hop}}} \quad \text{if } dR \ll \Delta_{R,\mathrm{dyn}}. \tag{7.20}$$

Because of the anharmonicities included in the LS-model, the mapping between hydrogen-bond coordinates R and the O–H stretch frequencies and cross-sections is however a more complicated relation (including non-Condon effects). Numerical calculation of τ_c by determining the exponential decay-time of the frequency time correlation function (FTCF) $\langle \delta\omega(0)\delta\omega(t)\rangle$ ($\delta\omega(t) = \omega(t) - \omega_0$, ω_0 being the mean frequency of the distribution), resulted in $\tau_c = 0.33$ ps for the $v_{OH} = 0 \rightarrow 1$ transition and $\tau_c = 0.27$ ps for the $v_{OH} = 1 \rightarrow 2$ transition. From Eq. 7.19 we find $\tau_c \simeq 0.3$ ps, which shows that the distributions are near-Gaussian.

Chapter 8

Vibrational dynamics of ice in reverse micelles

The ultrafast vibrational dynamics of HDO:D_2O ice at 180 K in AOT reverse micelles is studied by mid-infrared femtosecond pump-probe spectroscopy. Solutions containing reverse micelles are cooled to low temperatures by a fast-freezing procedure. The heating dynamics of the micellar solutions is studied to characterise the micellar structure. Small reverse micelles with a water content up to approximately 150 water molecules contain an amorphous form of ice that shows remarkably different vibrational dynamics compared to bulk hexagonal ice. The micellar amorphous ice has a much longer vibrational lifetime than bulk hexagonal ice and micellar liquid water. The vibrational lifetime is observed to increase linearly from 0.7 to 4 ps with the resonance frequency ranging from 3100-3500 cm^{-1}. From the dependence of the vibrational relaxation on the excitation frequency the homogeneous line width of the amorphous ice is determined (55±5 cm^{-1}).

8.1 Introduction

The confinement of liquid water to small volumes changes its structure and dynamics [10,30,37–39,43,56,99,109,111,122,130], but also its phase behaviour. Liquid water may be supercooled to much lower temperature when confined to micrometre sized capillaries. In the case of strongly confined ice, surface effects become important, and this may induce the formation of ice structures different from normal hexagonal ice *Ih*. [40, 65].

In the work presented in this chapter, reverse micellar solutions are cooled to low temperatures to study the effect of micellar confinement on the freezing behaviour of water. Low temperature reverse micelles have become of relevance to the field of cryoenzymology and low-temperature structural biology [3, 41], since these systems can be used to solubilise large amounts of protein. Several techniques have previously been used to study the freezing behaviour of reverse micelles, including linear spectroscopy [93], fluorescent probes [91] and

NMR [115]. These studies show that freezing occurs within the water pool at temperatures between 210-265 K, and that water inside reverse micelles may be supercooled to 240 K [91, 115]. Also the hydrogen bond network behaviour of the water pool exhibits a strong dependence on w_0 and does not approximate that of bulk water until w_0=40. [93]

The sample preparation of stable reverse micelles at low temperatures is challenging. Breakdown of micellar structure was observed for slowly frozen reverse micellar solutions [58, 91, 115, 138]. Using a fast-freezing procedure we find that clear reverse micellar dispersions can be prepared at low temperature, suggesting the retainment of the room-temperature micellar structure. Micelle stability is investigated by studying the heating dynamics of the micellar solutions. We find that the freezing leads to the formation of an amorphous type of ice in the interior of small reverse micelles. We study the ultrafast vibrational dynamics of this micellar amorphous ice, and find that it differs markedly from that of bulk crystalline ice.

8.2 Experimental

8.2.1 Sample Preparation

The investigated samples were mixtures of the surfactant salt AOT (Sodium bis(2-ethylhexyl) sulfosuccinate, SigmaUltra grade >99%, Aldrich), isooctane (anhydrous grade 99.8%, Aldrich), pentane (anhydrous grade >99%, Aldrich) and water (H_2O HPLC grade, Aldrich. D_2O >99.9%, Apollo Scientific). We used isotopic dilutions of HDO in D_2O (H_2O:D_2O = 1:40) to prevent the signals to be affected by intermolecular resonant energy transfer of the O–H stretch vibrations [131]. From the linear IR spectrum we deduced that the AOT used contains 1 H_2O molecule/25 AOT molecules, which was taken into account in determining the appropriate amounts of the constituents. The water mass fraction of all samples was 0.015. Pentane and isooctane were added in a 1:1 volume ratio. Samples were prepared by mixing the constituents without further purification. The micellar solution is contained within a copper sample cell consisting of two 2 mm thick sapphire windows that are separated by a 500 μm thick Kalrez spacer. The sample is mounted within a closed cycle cryostat (CTI-Cryogenics).

The micellar solutions were frozen rapidly by plunging the sample holder into liquid nitrogen, with resulting cooling rates on the order of 10^2 K/s [5, 62]. Even faster cooling rates ($> 10^5$ K/s) can be reached when freezing isolated micrometre sized droplets. In such cases water can be frozen into other forms than the usual hexagonal ice, like amorphous or cubic ice [64, 65]. Based on cooling speed alone, such different forms of ice are not expected to form in the reverse micelles, as in our experiments they are contained in bulk solutions that freeze relatively slowly.

We used a 1:1 ratio of isooctane and pentane as apolar solvent, since we found this mixture to form a clear glass upon freezing. After freezing the sample

the cryostat is closed and vacuumed. The temperature is subsequently raised to 180 K, so that ice deposited from the air onto the sample cell can be pumped off. At 180 K the apolar glass matrix melts and leaves the frozen micelles suspended.

The stability of reverse micelles is known to depend on temperature, and at low temperatures spontaneous solution demixing can occur [138]. Reverse micelles will then shed water from their interior [58, 91], thereby strongly decreasing the micelle water content. The rate of water shedding depends on temperature and micelle size, but has been reported to be a fairly slow process taking up to minutes [115]. During water shedding phase separation takes place in which the micellar structures breaks down and visual inspection reveals that large ice clusters form that sink to the bottom of the sample cell.

We use fast cooling to prevent water shedding from the micelle interior. In this way we prepare samples that are optically clear, suggesting the inhibition of water shedding. The micellar stability of our samples is characterised in Sec. 8.3.1. For normal micelles it has been well established that micellar structure can be retained when freezing the micellar solutions quickly [4, 11, 76], and similar reports exist for quickly frozen reverse micelles [5, 62].

8.2.2 Pump-probe experiment

Absorbance changes were recorded for probe light polarised parallel and perpendicular to the pump, as described previously in chapter 7. The sapphire windows of the sample cell are somewhat birefringent, which causes a limited amount of mixing of the parallel and perpendicular components (∼20%). We performed reference measurements using more fragile CaF_2 windows that do not introduce any birefringence. These measurements confirmed that the anisotropy parameter remained constant, which is expected for a rigid (not reorienting) solid as ice. We chose to only use the perpendicular data for further analysis, which is the probe polarisation least susceptible to scattered pump light.

8.3 Results and Discussion

8.3.1 Ultrafast heating dynamics and micelle stability

Linear infrared absorption spectra for the O–H stretch absorption of HDO:D_2O in AOT micellar solutions are displayed in Fig. 8.1, both at room temperature (top) and at 180 K after fast-freezing (bottom). For small reverse micelles ($w_0 \leq 3.5$) the O–H stretch spectrum remains broad upon freezing, which shows that a large spread in hydrogen bond lengths is present at low temperatures. The width of the absorption agrees well with that recorded for amorphous HDO:D_2O ice [129]. For micelles of $w_0 \geq 4$ an additional narrow absorption peak at 3300 cm^{-1} appears, which becomes the dominant feature for large micelles. This peak appears at the same spectral position as the O–H stretch absorption for bulk crystalline ice HDO:D_2O.

Fig. 8.2 shows the pump-induced transient absorption change as a function of delay for micelles with w_0=2 and w_0=4. Both pump and probe are tuned to the

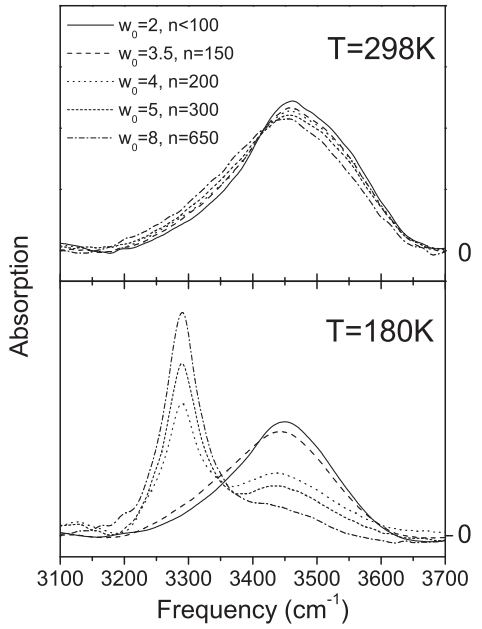

FIGURE 8.1. Linear O–H stretch absorption for AOT reverse micellar solutions at room temperature (top) and at 180 K (bottom). The micelle size increases with the parameter w_0=[water]/[surfactant]. The value of n equals the approximate number of water molecules per reverse micelle [1, 112].

maximum of the absorption band. At delay zero the transmission is increased because of ground state depletion of the O–H stretch vibration and stimulated emission out of the v_{OH}=1 state. The transmission increase is followed by vibrational relaxation and thermalisation dynamics. The vibrational relaxation will be discussed in detail in the next subsection. A striking difference between the signals measured for the two micelles is the magnitude of the signal at delays >10 ps. For a micelle with $w_0 = 2$ the signal has practically vanished, whereas for a micelle with $w_0 = 4$ a large transmission change related to thermalisation dynamics is observed.

The signal measured at large delays reflects the amount of heating induced by the pump-pulse excitation. Heating affects the cross-section spectrum of the O–H stretch vibration by a blue-shift and decrease in amplitude (see chapter 7, [36]). These cross-section changes result in absorption changes $\Delta\alpha_T(\omega, t)$ for the time-delayed infrared pulse probing the sample. The amplitude of this absorption change is known to be linearly dependent on the amount of heat absorbed by the sample for both water [118] and ice [60]. The amplitude of the

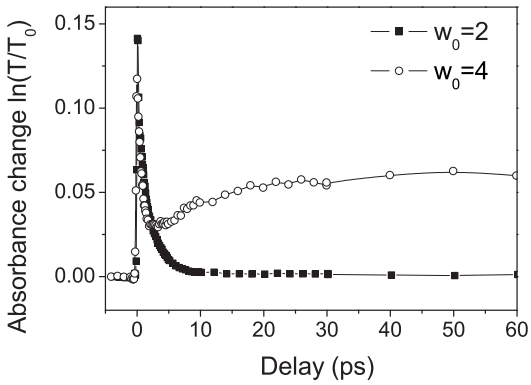

FIGURE 8.2. Pump induced absorbance change plotted as a function of probe delay for a sample of w_0=2 and 4 at 180 K. The pump/probe frequencies were 3450/3444 cm^{-1} and 3300/3293 cm^{-1}, respectively. Much stronger absorbance changes related to heating are observed for samples of $w_0 \geq 4$ than for $w_0 < 4$.

absorption change can thereby act as a local thermometer.

Fig. 8.3a shows the amplitude of the transmission changes induced by the heating effect at 60 ps time delay as a function of w_0. The amplitude of the heat effect is scaled to the amplitude of the transmission changes at 0.2 ps, to correct for the intensity of the excitation pulse (since the data for liquid micelles were recorded at magic angle instead of at a perpendicular probe polarisation [38], the relative amplitude of the heating effect was upscaled for these measurements by a factor 5/3). For $w_0 \leq 3.5$ the heating effect is equally small for frozen micellar solutions as for liquid micellar solutions. Directly after vibrational relaxation of a liquid reverse micellar solution, the sample will contain hot reverse micelles suspended in a cooler apolar solvent. The micelles will cool to the surrounding solvent on a picosecond timescale [112]. When the micelle cooling is complete, the heat is equilibrated over the micelles and the solvent. Since the solvent takes up the majority of the sample volume, the final heating effect on the micelles will be very small.

For frozen micellar solutions of $w_0 \geq 4$ very slow cooling is observed, and more than 50% of the heating signal remains at 1000 ps. At 60 ps the heating effect still has a similar amplitude as a heated sample of bulk ice of the same concentration of HDO molecules, while for liquid micellar solutions of the same w_0 at this delay time cooling is already complete. The heating dynamics reveal that our preparation method leads to stable micelles up to $w_0 = 3.5$ and that for $w_0 \geq 4$ the micelles fall apart forming large clusters of ice. The cooling times of these clusters are slower than 1000 ps, which implies that the clusters must have a typical size larger than 10 nm [112]. The fact that the solutions

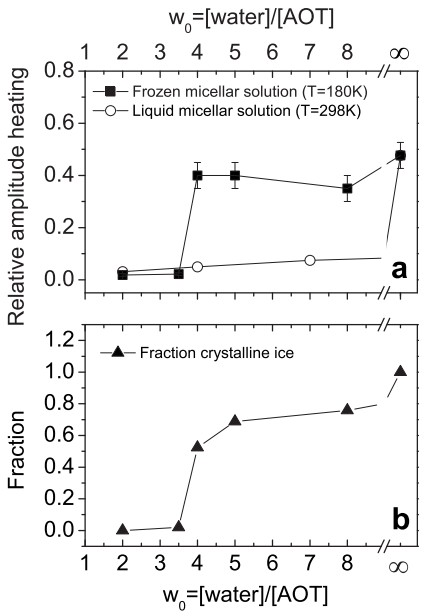

FIGURE 8.3. a: Amplitude of the measured absorption changes induced by heating at 60 ps probe delay (at the probe frequency of maximum absorption change). The amplitudes are scaled relative to the absorption change induced by population transfer at 0.2 ps, to divide out any dependence of the signal amplitude on the laser intensity. b: Fraction crystalline ice as a function of the parameter w_0. This fraction is determined by fitting the linear absorption spectra of Fig. 8.1 to a linear combination of the w_0=2 and bulk crystalline ice spectra.

are optically clear puts an upper limit of 500 nm to the cluster size.

It is instructive to correlate the heating dynamics with the appearance of the crystalline ice peak in the linear absorption spectrum. For all micellar solutions the linear absorption spectrum can be fitted by a linear combination of the spectrum of the $w_0 = 2$ sample and that of bulk HDO:D_2O ice. Only the relative fraction of the two components varies over the range of w_0 considered. The fraction crystalline ice for each sample is plotted as a function of w_0 in Fig. 8.3b. From this figure it is clear that in the transition from a micellar solution of $w_0 = 3.5$ to $w_0 = 4$ the relative amount of crystalline ice is sharply increasing. The transition takes place at the same value of w_0 at which we identified the onset of micellar breakup from the heating dynamics (see Fig. 8.3a). Most crystalline ice will therefore be found outside the reverse micelles, coalesced in larger ice crystals.

We conclude that the aqueous core of the micelles is stabilised in an amorphous form of ice for micellar structures up to $w_0 = 3.5$. This micelle contains

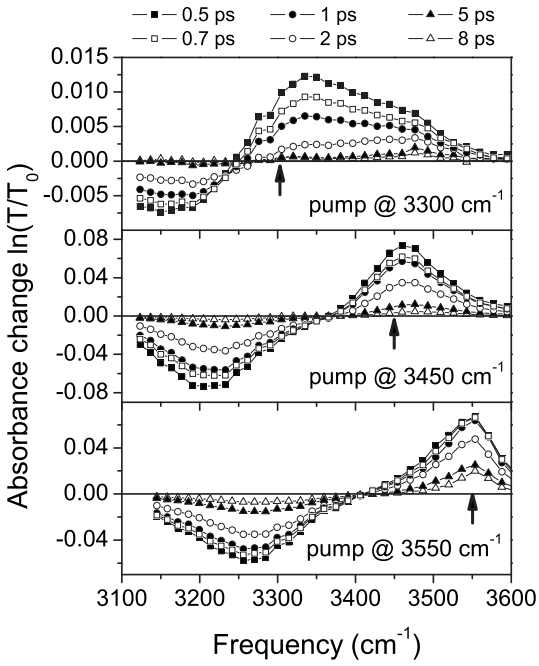

FIGURE 8.4. Transient absorbance change for a micelle of w_0=2 at various probe delays, when exciting the sample by a pump pulse centered at 3300 cm^{-1} (top), 3450 cm^{-1} (middle) and 3550 cm^{-1} (bottom). The transient spectrum shifts with pump frequency.

approximately 150 water molecules [1, 112]. Breakup of larger reverse micelles is observed to coincide with the appearance of crystalline ice in the sample.

8.3.2 Vibrational dynamics of micelle-confined amorphous ice

Fig. 8.4 shows the pump-induced transient absorption change plotted for different pump frequencies and varying probe delays for a micelle with w_0=2. After excitation by the pump, the transmission is increased at frequencies matching the $v_{\mathrm{OH}} = 0 \rightarrow 1$ transition (because of ground state depletion of the O–H stretch vibration and stimulated emission out of the v_{OH}=1 state), whereas the transmission is decreased at the more red-shifted frequencies matching the $v_{\mathrm{OH}} = 1 \rightarrow 2$ transition (where the induced population in the v=1 state causes absorption). The pump–probe spectra obtained with different pump frequencies are shifted in frequency and remain so at all delays. The amorphous ice apparently contains a strongly inhomogeneous distribution of OH oscillators that are

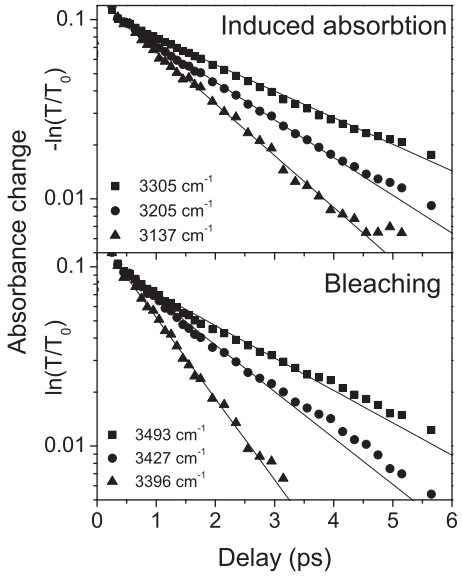

FIGURE 8.5. Pump induced absorbance change plotted as a function of probe delay at various probe frequencies. The pump frequency was 3450 cm^{-1}. Vibrational relaxation is observed to be strongly frequency dependent; the transient absorption change is well described by a mono-exponential decay with a time-constant depending on the probe frequency.

spectrally different and do not interchange their absorption frequencies. The O–H stretch frequency is strongly correlated to the length of the donated hydrogen bond. For this reason, the absence of any spectral dynamics shows the absence of large fluctuations in hydrogen bond lengths. The amorphous ice apparently contains a static ensemble of different hydrogen bonds.

It should be noted that a large amount of the amorphous ice will be surfactant bound water. The interaction between the AOT surfactant and water can be strong, and its sulfonate head group can accept hydrogen bonds from several water molecules [35]. Therefore the majority of the micellar amorphous ice may in fact be bound to surfactant molecules.

The vibrational relaxation of the micellar amorphous ice is observed to be very frequency dependent. This is illustrated in Fig. 8.5, where we show the transient absorption at different probe frequencies as a function of pump-probe delay. The relaxation decay constant increases with absorption frequency from 0.7 to 4 ps. The vibrational relaxation of HDO water in liquid micelles has been described with a two-component model in chapter 4. Two relaxation times were sufficient to describe the vibrational dynamics at all frequencies within the

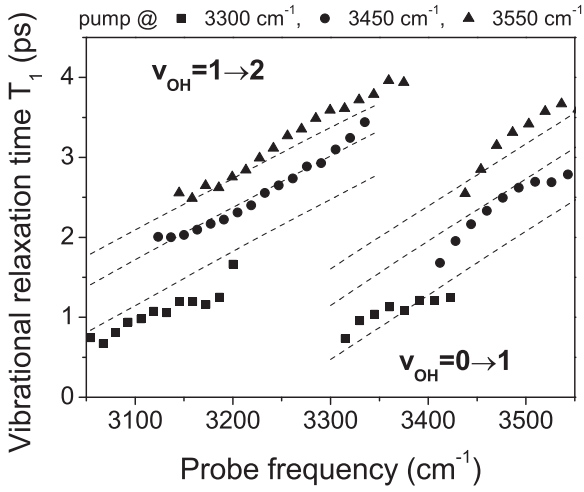

FIGURE 8.6. Fitted exponential time constants for the transient absorption change recorded at different probe frequencies. The time-constants are observed to depend on the centre frequency of the pump (data shown for a pump centred at 3300 cm^{-1}, 3450 cm^{-1} or 3550 cm^{-1}). Dotted lines are fits that assume a linear dependence of the vibrational relaxation time on the O–H stretch frequency and a homogeneous line width of 55 cm^{-1}.

absorption band. The two components in the vibrational relaxation could be related to two different types of water molecules, bulk-like molecules in the core of the micelles (T_1=0.7-1 ps) versus interfacial molecules bound to the AOT surfactant molecules (T_1=2.8 ps). The vibrational relaxation presented here for frozen micelles cannot be described with two time constants, and a much more inhomogeneous distribution of relaxation times is observed.

While for bulk HDO:D_2O water the vibrational relaxation becomes faster upon freezing (from 0.8 ps to 0.4 ps, see chapter 7, [133]), for micellar HDO:D_2O it becomes slower. The freezing of bulk water results in a strong narrowing and red shift of the O–H stretch absorption, related to increased structural order and hydrogen bond strengthening. The red shift brings the O–H stretch energy in closer resonance with the HOD bending overtone, facilitating faster vibrational relaxation. The O–H stretch spectrum of amorphous micellar ice does not undergo such a red shift. Therefore the energy gap with the overtone of the bending mode remains large and the relaxation involves lower-frequency modes to make up for the energy gap. At low temperatures the coupling to these modes will be reduced, because these modes will be less populated due to a small Boltzmann factor. This effect likely explains why the relaxation is even slower than for HDO:D_2O micellar water in the liquid phase.

The relaxation at each frequency can be well described by a single exponential decay (see Fig. 8.5). The fitted time-constants are plotted in Fig. 8.6. Besides a dependence on the probe frequency, the vibrational relaxation also depends on the pump frequency. At a fixed probe frequency, more slowly relaxing molecules are observed if these are excited by a pump that has been tuned to the blue side of the spectrum. This can be understood by noting that the inhomogeneously broadened O–H stretch absorption consists of an ensemble of homogeneous absorption lines with different centre frequencies. At a fixed probe frequency, more high frequency homogeneous lines will be excited by a more blue pump frequency, which have a longer associated T_1 relaxation time.

We model the pump-selectivity in the observed T_1 by assuming a frequency dependence for T_1 and a single homogeneous line width across the entire O–H stretch absorption band. We define $S_{\rm hom}(\omega,\omega')$ as a Gaussian homogeneous line of width $\sigma_{\rm hom}$ and centre frequency ω'. We can deconvolute the homogeneous broadening from the linear absorption spectrum to obtain the frequency distribution of homogeneous lines $I(\omega)$, such that the linear absorption spectrum equals $\int I(\omega')S_{\rm hom}(\omega-\omega',0)d\omega'$. The effectively observed T_1 at a probe frequency $\omega_{\rm pr}$ will then be the weighted average over all the homogenous distributions that have been excited by the pump centred at frequency $\omega_{\rm pu}$:

$$T_1(\omega_{\rm pr},\omega_{\rm pu}) = \frac{\int_0^\infty d\omega S_{\rm pu}(\omega,\omega_{\rm pu})S_{\rm hom}(\omega_{\rm pr},\omega)I(\omega)\cdot T_1(\omega)}{\int_0^\infty d\omega S_{\rm pu}(\omega,\omega_{\rm pu})S_{\rm hom}(\omega_{\rm pr},\omega)I(\omega)}. \qquad (8.1)$$

$S_{\rm pu}(\omega,\omega_{\rm pu})$ equals the pump spectrum when centred at $\omega_{\rm pu}$, which is taken to be a Gaussian of FWHM 80 cm^{-1}. $T_1(\omega)$ equals the relaxation time as a function of O–H stretch absorption frequency. In view of the observed inhomogeneities in the vibrational relaxation, the homogeneous line width will be much smaller than the width of the linear absorption spectrum. In this limit we can approximate $I(\omega)$ with the linear absorption spectrum itself.

We find a good description of the measured relaxation times of the $v_{\rm OH} = 0 \rightarrow 1$ transition when $T_1(\omega)$ varies linearly with frequency according to $T_1(\omega) = A + B(\omega-\omega_0)$, where ω_0 is taken the central frequency of the O–H stretch band (ω_0=3450 cm^{-1}). For the $v_{\rm OH} = 1 \rightarrow 2$ absorption the same relation holds, but since this transition is red-shifted by the anharmonicity Δ and broadened by a factor k=1.2, we make the transformation B $\rightarrow$ B/k and $\omega_0 \rightarrow \omega_0-\Delta$. By a least squares fit we find A=2.4±0.2 ps, B=0.014±0.002 ps/cm^{-1}, Δ=255±10 cm^{-1} and $\sigma_{\rm hom}$=55±5 cm^{-1}. The fitted curves are displayed as dotted lines in Fig. 8.6. The homogeneous line width for the amorphous ice (55 cm^{-1}) turns out to be similar to the line width of bulk HDO:D_2O ice (50 cm^{-1}) at 180 K. The bulk HDO:D_2O ice absorption is known to be only slightly inhomogeneously broadened (see chapter 7).

In view of the spectral width of the pump (80 cm^{-1}) and the homogeneous line width (55 cm^{-1}) a distribution of oscillators with different relaxation times T_1 will be excited at each probe frequency. This leads in principle to a slight multi-exponential decay of the pump-probe signal. Oscillators with a longer T_1 will contribute longer to the signal than oscillators with a shorter T_1, causing

the pump-probe signal to decay somewhat slower at later delay times. A close inspection of the decay curves of Fig. 8.5 indeed reveals some multi-exponential behaviour.

Comparing data and fit of Fig. 8.6 shows that a fully linear relation between T_1 and the O–H stretch frequency as assumed in our model is a slight over-simplification. At low frequencies the T_1 increases with frequency somewhat more slowly than at high frequencies. For many hydrogen-bonded systems T_1 is related to the O–H stretch frequency not according to a linear dependence, but by a nearly inverse quadratic relation: $T_1(\omega) = a(\omega_{\mathrm{OH}} - \omega_{\mathrm{OH,g}})^{-1.8}$, with a a constant and $\omega_{\mathrm{OH,g}}$ the vibrational frequency of the O-H group in the gas phase [89,117]. This relation shows a stronger frequency dependence of the T_1 at blue frequencies compared to red frequencies, but this nonlinearity was found to be far too strong to be in accordance with our experimental data. The formula was derived for the case of vibrational predissociation, in which vibrational energy can be transferred to the O$\cdots$O hydrogen bond stretch coordinate only. In amorphous ice, the relaxation likely involves energy transfer to the overtone of the bending mode. This prevents the relaxation time to go to infinity near the gas-phase frequency, as predicted by the inverse quadratic equation. A linear frequency dependence is more adequate in describing the experiment.

The $v_{\mathrm{OH}} = 1 \rightarrow 2$ line shape of the amorphous ice is slightly broader than the $v_{\mathrm{OH}} = 0 \rightarrow 1$ transition, by a factor of 1.2. This strongly contrasts with the case of bulk HDO:D_2O ice [113], where the $v_{\mathrm{OH}} = 1 \rightarrow 2$ transition is broadened by a factor of 5. The broadening in bulk ice was found to be related primarily to a very short vibrational lifetime of the v_{OH}=2 state [36] (see chapter 7). The v_{OH}=2 state of bulk ice is resonant with the HDO bending overtone, which facilitates very fast vibrational energy relaxation. The amorphous ice studied here has an O–H stretch spectrum that absorbs at more blue-shifted frequencies, frustrating enhanced relaxation by this Fermi resonance. The $v_{\mathrm{OH}} = 1 \rightarrow 2$ transition is therefore not significantly life-time broadened.

The micellar amorphous ice that is hydrogen bonded to the sulfonate head group of the surfactant likely experiences a somewhat different OH$\cdots$O potential than bulk water and ice. For liquid water a second broadening mechanism of the $v_{\mathrm{OH}} = 1 \rightarrow 2$ transition was identified, related to proton delocalization in the $v_{\mathrm{OH}} = 2$ state [7, 36]. In bulk ice this mechanism cannot be present as it does not agree with the narrow spread in hydrogen bond lengths [36]. In the micellar amorphous ice the spread in hydrogen bond lengths is much broader, however no $v_{\mathrm{OH}} = 1 \rightarrow 2$ broadening is observed in this case either. This confirms that the OH$\cdots$O potential for amorphous ice contained in the micelles differs from that of liquid water.

8.4 Conclusions

We studied the vibrational dynamics of frozen water contained in AOT reverse micelles with femtosecond mid-infrared pump-probe spectroscopy. From the thermalisation dynamics we deduce that fast freezing of AOT reverse micellar

solutions leaves the micellar structure intact up to a micelle water content of $w_0 = 3.5$. Larger micelles break up to form larger crystalline ice structures in the size range of 10-500 nm. Freezing micellar solutions at higher cooling rates is necessary to extend the stability range to micelles with a higher water content.

The intact reverse micelles of water content $w_0 \leq 3.5$ contain amorphous ice, which may for a large part be hydrogen bonded to AOT surfactant molecules. The linear absorption spectrum of this micellar amorphous ice is equally broad as for water in the liquid phase, which implies the existence of a large degree of structural disorder and spread in hydrogen bond lengths.

The vibrational relaxation rate of micellar amorphous ice is found to increase almost linearly with the O–H stretch absorption frequency, from 0.7 to 4 ps. Compared to the relaxation rate of micellar water in the liquid phase [38] (surfactant-bound 2.8 ps, D_2O-bound 0.7-1 ps), the average vibrational relaxation of the amorphous water slows down upon freezing. This contrasts with the case of bulk HDO:D_2O, for which the vibrational relaxation rate increases (from 740 fs at T=298 K to 420 fs at T=180 K) [133]. From the pump-frequency dependence of the vibrational relaxation we deduce that the homogeneous line width equals 55±5 cm^{-1}.

The line width of the $v_{OH} = 1 \rightarrow 2$ transition of the micellar amorphous ice is only slightly broadened compared to the $v_{OH} = 0 \rightarrow 1$ transition. This differs from the case of liquid HDO:D_2O, which has equal structural disorder, but where the $v_{OH} = 1 \rightarrow 2$ is broadened significantly due to proton delocalisation in the $v_{OH} = 2$ state [7]. The O–H stretch potential of the amorphous ice must thus be different from that of bulk water.

Bibliography

[1] S. Abel, F. Sterpone, S. Bandyopadhyay, and M. Marchi. Molecular modeling and simulations of AOT-water reverse micelles in isooctane: Structural and dynamic properties. *J. Phys. Chem. B*, 108:19458–19466, 2004.

[2] P. W. Atkins. *Physical Chemistry.* Oxford University Press, 1994.

[3] C. R. Babu, V. J. Hilser, and A. J. Wand. Direct access to the cooperative substructure of proteins and the protein ensemble via cold denaturation. *Nat. Struct. Mol. Biol.*, 11(4):352–357, Apr. 2004.

[4] P. Baglioni and L. Kevan. Structural effects of alcohol addition to sodium dodecyl sulfate micelles studied by electron spin-echo modulation of 5-doxylstearic acid spin probe. *J. Phys. Chem.*, 91:1516–1518, 1987.

[5] P. Baglioni, H. Nakamura, and L. Kevan. Electron spin echo modulation study of AOT reverse micelles. *J. Phys. Chem.*, 95:3856–3859, 1991.

[6] H. J. Bakker and H.-K. Nienhuys. Delocalization of protons in liquid water. *Science*, 297:587–590, 2002.

[7] H. J. Bakker, H.-K. Nienhuys, G. Gallot, N. Lascoux, G. M. Gale, J.-C. Leicknam, and S. Bratos. Transient absorption of vibrationally excited water. *J. Chem. Phys.*, 116:2592–2598, 2002.

[8] H. J. Bakker, S. Woutersen, and H.-K. Nienhuys. Reorientational motion and hydrogen-bond stretching dynamics in liquid water. *Chem. Phys.*, 258:233–245, 2000.

[9] S. Balasubramanian, S. Pal, and B. Bagchi. Hydrogen-bond dynamics near a micellar surface: Origin of the universal slow relaxation at complex aqueous interfaces. *Phys. Rev. Lett.*, 89(11):115505, 2002.

[10] M.-C. Belissent-Funel, S. H. Chen, and J.-M. Zanotti. Single-particle dynamics of water molecules in confined space. *Physical Review E*, 51(5):4558–4568, 1995.

[11] J. R. Bellare, T. Kaneko, and D. F. Evans. Seeing micelles. *Langmuir*, 4:1066–1067, 1988.

[12] P. A. Bergstrom, J. Lindgren, and O. Kristiansson. An IR study of the hydration of ClO_4^-, NO_3^-, I^-, Br^-, Cl^-, and SO_4^{2-} anions in aqueous-solution. *J. Phys. Chem.*, 95(22):8575–8580, Oct. 1991.

[13] S. Berr, R. R. M. Jones, and J. S. Johnson. Effect of counterion on the size and charge of alkyltrimethylammonium halide micelles as a function of chain-length and concentration as determined by small-angle neutron-scattering. *J. Phys. Chem.*, 96(13):5611–5614, June 1992.

[14] S. S. Berr. Solvent isotope effects on alkytrimethylammonium bromide micelles as a function of alkyl chain length. *J. Phys. Chem.*, 91:4760–4765, 1987.

[15] J. E. Bertie and E. Whalley. Infrared spectra of ices Ih and Ic in the range 4000-350 cm^{-1}. *J. Chem. Phys.*, 40:1637, 1963.

[16] B. Bhushan, J. N. Israelachvili, and U. Landman. Nanotribology - friction, wear and lubrication at the atomic-scale. *Nature*, 374:607–616, 1995.

[17] P. Bodis, O. F. A. Larsen, and S. Woutersen. Vibrational relaxation of the bending mode of HDO in liquid D_2O. *J. Phys. Chem. A*, 109:5303–5306, 2005.

[18] V. Botan, E. H. G. Backus, R. Pfister, A. Moretto, M. Crisma, C. Toniolo, P. H. Nguyen, G. Stock, and P. Hamm. Energy transport in peptide helices. *Proc. Natl. Acad. Sci. U. S. A.*, 104:12749–12754, 2007.

[19] R. W. Boyd. *Nonlinear Optics.* Academic Press, San Diego, 1992. p. 122.

[20] J. Braun, A. Glebov, A. P. Graham, A. Menzel, and J. P. Toennies. Structure and phonons of the ice surface. *Phys. Rev. Lett.*, 80:2638–2641, 1998.

[21] J. B. Brubach, A. Mermet, A. Filabozzi, A. Gerschel, D. Lairez, M. P. Krafft, and P. Roy. Dependence of water dynamics upon confinement size. *J. Phys. Chem. B*, 105(2):430–435, Jan. 2001.

[22] V. Buch and J. Devlin. A new interpretation of the OH-stretch spectrum of ice. *J. Chem. Phys.*, 110:3437–3443, 1999.

[23] C. A. Bunton, F. Nome, F. H. Quina, and L. S. Romsted. Ion binding and reactivity at charged aqueous interfaces. *Acc. Chem. Res.*, 24(12):357–364, Dec. 1991.

[24] C. J. Burnham, J. Li, S. S. Xantheas, and M. Leslie. The parametrization of a thole-type all-atom polarizable water model from first principles and its application to the study of water clusters (n=2–21) and the phonon spectrum of ice Ih. *J. Chem. Phys.*, 110:4566–4581, 1999.

[25] A. I. Burshtein and V. S. Malinovsky. Free-induction decay in the framework of sudden-modulation theory. *J. Opt. Soc. Am. B*, 8:1098–1113, 1991.

[26] G. Carlström and B. Halle. Water dynamics in microemulsion droplets. A nuclear spin relaxation study. *Langmuir*, 4:1346–1352, 1988.

[27] D. Chapman. A contribution to the theory of electrocapillarity. *Philos. Mag.*, 25:475–481, 1913.

[28] L. Cheng, P. Fenter, K. L. Nagy, M. L. Schlegel, and N. C. Sturchio. Molecular-scale density oscillations in water adjacent to a mica surface. *Phys. Rev. Lett.*, 87(15):156103, 2001.

[29] M. L. Cowan, B. D. Bruner, N. Huse, J. R. Dwyer, B. C. B, E. T. J. Nibbering, T. Elsaesser, and R. J. D. Miller. Ultrafast memory loss and energy redistribution in the hydrogen bond network of liquid H_2O. *Nature*, 434:199–202, 2005.

[30] D. Cringus, J. Lindner, M. T. W. Milder, M. S. Pshenichnikov, P. Voehringer, and D. A. Wiersma. Femtosecond water dynamics in reverse-micellar nanodroplets. *Chem. Phys. Lett.*, 408:162–168, 2005.

[31] I. M. Cuccovia, L. G. Dias, F. A. Maximiano, and H. Chaimovich. Analysis of the bromide ion distribution in the water pool of reverse micelles of hexadecyltrimethylammonium bromide in chloroform/n-dodecane and isooctane/n-hexanol by chemical trapping. *Langmuir*, 17(4):1060–1068, Feb. 2001.

[32] P. K. Das, G. V. Srilakshmi, and A. Chaudhuri. Experimental probing of water and counterion concentrations inside a reversed micelle water-pool: An overlooked parameter in micellar enzymology? *Langmuir*, 15(4):981–987, Feb. 1999.

[33] J. Deak, S. Rhea, L. Iwaki, and D. Dlott. Vibrational energy relaxation and spectral diffusion in water and deuterated water. *J. Phys. Chem. A*, 104:4866, 2000.

[34] J. C. Deak, Y. Pang, T. D. Sechler, Z. Wang, and D. D. Dlott. Vibrational energy transfer across a reverse micelle surfactant layer. *Science*, 306:473–476, 2004.

[35] B. Derecskei, A. Derecskei-Kovacs, and Z. Schelly. Atomic-level molecular modeling of AOT reverse micelles. 1. The AOT molecule in water and carbon tetrachloride. *Langmuir*, 15:1981–1992, 1999.

[36] A. M. Dokter and H. J. Bakker. Transient absorption of vibrationally excited ice. *J. Chem. Phys.*, 128:024502, 2008. Accepted JCP Manuscript A7.09.175, AIP ID: 010748JCP.

[37] A. M. Dokter, S. Woutersen, and H. J. Bakker. Anomalous slowing down of the vibrational relaxation of liquid water upon nanoscale confinement. *Phys. Rev. Lett.*, 94:178301, 2005.

[38] A. M. Dokter, S. Woutersen, and H. J. Bakker. Inhomogeneous dynamics in confined water nanodroplets. *Proc. Natl. Acad. Sci. U. S. A.*, 103:15355–15358, 2006.

[39] A. M. Dokter, S. Woutersen, and H. J. Bakker. Ultrafast dynamics of water in cationic micelles. *J. Chem. Phys.*, 126:124507, 2007.

[40] J. Dore. Structural studies of water in confined geometry by neutron diffraction. *Chem. Phys.*, 258:327–347, 2000.

[41] P. Douzou, E. Keh, and C. Balny. Cryoenzymology in aqueous media: Micellar solubilized water clusters. *Proc. Natl. Acad. Sci. U. S. A.*, 76:681–684, 1979.

[42] J. Faeder, M. V. Albert, and B. M. Ladanyi. Molecular dynamics simulations of the interior of aqueous reverse micelles: A comparison between sodium and potassium counterions. *Langmuir*, 19(6):2514–2520, Mar. 2003.

[43] J. Faeder and B. M. Ladanyi. Molecular dynamics simulations of the interior of aqueous reverse micelles. *J. Phys. Chem. B*, 194:1033–1046, 2000.

[44] M. Falk. On the satellite bands accompanying the OH and OD stretching fundamentals of isotopically dilute HDO in ice Ih. *J. Chem. Phys.*, 87:28–30, 1987.

[45] R. J. Farn, editor. *Chemistry and Technology of Surfactants.* Blackwell Publishing Ltd, 2006.

[46] R. A. Farrer and J. T. Fourkas. Orientational dynamics of liquids confined in nanoporous sol-gel glasses studied by optical kerr effect spectroscopy. *Acc. Chem. Res.*, 36:605–612, 2003.

[47] C. J. Fecko, J. D. Eaves, J. J. Loparo, A. Tokmakoff, and P. L. Geissler. Ultrafast hydrogen-bond dynamics in the infrared spectroscopy of water. *Science*, 301(5640):1698–1702, Sept. 2003.

[48] C. J. Fecko, J. J. Loparo, S. T. Roberts, and A. Tokmakoff. Local hydrogen bonding dynamics and collective reorganization in water: Ultrafast infrared spectroscopy of HOD/D_2O. *J. Chem. Phys.*, 122:054506, 2005.

[49] D. Fioretto, M. Freda, G. Onori, and A. Santucci. Effect of counterion substitution on aot-based micellar systems: Dielectric study of $Cu(AOT)_2$ reverse micelles in CCl_4. *J. Phys. Chem. B*, 103:2631–2635, 1999.

[50] F. Franks, editor. *Water - A Comprehensive Treatise*, volume 3. Plenum Press, 1973.

[51] M. Fredo, G. Onori, A. Paciaroni, and A. Santucci. Hydration and dynamics of Aerosol OT reverse micelles. *J. Mol. Liq.*, 1-3:55–68, 2002.

[52] A. Gale, G. Gallot, F. Hache, N. Lascoux, S. Bratos, and J. Leicknam. Femtosecond dynamics of hydrogen bonds in liquid water: A real time study. *Phys. Rev. Letters*, 82:1068–1071, 1999.

[53] M. Giustini, G. Palazzo, G. Colafemmina, M. DellaMonica, M. Giomini, and A. Ceglie. Microstructure and dynamics of the water-in-oil CTAB/n-pentanol/n-hexane/water microemulsion: A spectroscopic and conductivity study. *J. Phys. Chem.*, 100(8):3190–3198, Feb. 1996.

[54] G. Gouy. Sur la constitution de la charge électrique à la surface d'un électrolyte. *J. Phys.*, 9:457–468, 1910.

[55] C. Haas and D. F. Hornig. Inter- and intramolecular potentials and the spectrum of ice. *J. Chem. Phys.*, 32:1763, 1960.

[56] M. R. Harpham, B. M. Ladanyi, and N. E. Levinger. Water motion in reverse micelles studied by quasielastic neutron scattering and molecular dynamics simulations. *J. Chem. Phys.*, 121:7855–7868, 2004.

[57] M. R. Harpham, B. M. Ladanyi, and N. E. Levinger. The effect of the counterion on water mobility in reverse micelles studied by molecular dynamics simulations. *J. Phys. Chem. B*, 109:16891–16900, 2005.

[58] W. D. V. Horn, A. K. Simorellis, and P. F. Flynn. Low-temperature studies of encapsulated proteins. *J. Am. Chem. Soc.*, 127:13553–13560, 2005.

[59] N. Huse, S. Ashihara, E. Nibbering, and T. Elsaesser. Ultrafast vibrational relaxation of O–H bending and librational excitations in liquid H_2O. *Chem. Phys. Lett.*, 404:389, 2005.

[60] H. Iglev, M. Schmeisser, K. Simeonidis, A. Thaller, and A. Laubereau. Ultrafast superheating and melting of bulk ice. *Nature*, 439:183–186, 2006.

[61] J. Israelachvili. *Intermolecular and Surface Forces.* Academic Press, Elsevier Ltd., 1991.

[62] W. Jahn and R. Strey. Microstructure of microemulsions by freeze fracture electron microscopy. *J. Phys. Chem.*, 92:2294–2301, 1988.

[63] T. K. Jain, M. Varshney, and A. Maitra. Structural studies of Aerosol OT reverse micellar aggregates by FT-IR spectroscopy. *J. Phys. Chem.*, 93(21):7409–7416, Oct. 1989.

[64] G. Johari and O. Andersson. Vibrational and relaxational properties of crystalline and amorphous ices. *Thermochim. Acta*, 461:14–43, 2007.

[65] G. P. Johari. Water's size-dependent freezing to cubic ice. *J. Chem. Phys.*, 122:194504, 2005.

[66] F. N. Keutsch and R. J. Saykally. Water clusters: Untangling the mysteries of the liquid, one molecule at a time. *Proc. Natl. Acad. Sci. U. S. A.*, 98:10533–10540, 2001.

[67] S. Koonin. *Computational Physics.* Menlo Park Ca, Benjamin, 1986.

[68] M. F. Kropman and H. J. Bakker. Dynamics of water molecules in aqueous solvation shells. *Science*, 291:2118–2120, 2001.

[69] M. F. Kropman and H. J. Bakker. Effect of ions on the vibrational relaxation of liquid water. *J. Am. Chem. Soc.*, 126(29):9135–9141, July 2004.

[70] M. F. Kropman, H.-K. Nienhuys, and H. J. Bakker. Real-time measurement of the orientational dynamics of aqueous solvation shells in bulk liquid water. *Phys. Rev. Lett.*, 88:077601–1–077601–4, 2002.

[71] R. Kubo, M. Toda, and N. Hashitsume. *Statistical Physics II: Nonequilibrium Statistical Mechanics.* Springer-Verlag Berlin Heidelberg New York, 2nd edition, 1995.

[72] W. Kuhs and M. Lehmann. The geometry and orientation of the water molecule in ice-Ih. *J. Phys. (Paris)*, 48:C1, 3, 1987.

[73] J.-L. Kuo, M. L. Klein, and W. F. Kuhs. The effect of proton disorder on the structure of ice-Ih: A theoretical study. *J. Chem. Phys.*, 123:134505–1–134505–6, 2005.

[74] D. Laage and J. Hynes. A molecular jump mechanism of water reorientation. *Science*, 311:832–835, 2006.

[75] J. Lang, G. Mascolo, R. Zana, and P. L. Luisi. Structure and dynamics of cetyltrimethylammonium bromide water-in-oil microemulsions. *J. Phys. Chem.*, 94:3069–3074, 1989.

[76] C. Lange and T. Wolff. Calorimetric effects in rapidly frozen micellar solutions below the macroscopic melting point. *Colloid Polym. Sci.*, 284:214–217, 2005.

[77] D. Langevin. Microemulsions. *Acc. Chem. Res.*, 21:255–260, 1988.

[78] C. P. Lawrence and J. L. Skinner. Vibrational spectroscopy of HOD in liquid D_2O. III. spectral diffusion, and hydrogen-bonding and rotational dynamics. *J. Chem. Phys.*, 118:264–272, 2003.

[79] N. E. Levinger. Water in confinement. *Science*, 298:1722–1723, 2002.

[80] J. Lindner, P. Vöhringer, M. S. Pshenichnikov, D. Cringus, D. A. Wiersma, and M. Mostovoy. Vibrational relaxation of pure liquid water. *Chem. Phys. Lett.*, 421:329–333, 2006.

[81] G. Lipari and A. Szabo. Effect of librational motion on fluorescence depolarization and nuclear magnetic resonance relaxation in macromolecules and membranes. *Biophys. J.*, 30:489–506, 1980.

[82] E. R. Lippincott and R. Schroeder. One-dimensional model of the hydrogen bond. *J. Chem. Phys.*, 23:1099–1106, 1955.

[83] A. J. Lock and H. J. Bakker. Temperature dependence of vibrational relaxation in liquid H_2O. *J. Chem. Phys.*, 117:1708–1713, 2002.

[84] R. Loudon. *The Quantum Theory of Light*. Oxford University Press, 2000.

[85] H. MacDonald, B. Bedwell, and E. Gulari. FTIR spectroscopy of microemulsion structure. *Langmuir*, 2:704–708, 1986.

[86] A. Maitra. Determination of size parameters of water-Aerosol OT-oil reverse micelles from their nuclear magnetic resonance data. *J. Phys. Chem.*, 88:5122–5125, 1984.

[87] I. Mellman. Endocytosis and molecular sorting. *Annu. Rev. Cell Dev. Biol.*, 12:575–625, 1996.

[88] W. Mikenda and S. Steinböck. Stretching frequency vs. bond distance correlation of hydrogen bonds in solid hydrates: a generalized correlation function. *J. Mol. Struct.*, 384:159–163, 1996.

[89] R. E. Miller. The vibrational spectroscopy and dynamics of weakly bound neutral complexes. *Science*, 240:447–453, 1988.

[90] S. Mukamel. *Principles of Nonlinear Optical Spectroscopy*. Oxford University Press, 1999.

[91] C. A. Munson, G. A. Baker, S. N. Baker, and F. V. Bright. Effects of subzero temperatures on fluorescent probes sequestered within aerosol-OT reverse micelles. *Langmuir*, 20(5):1551–1557, Mar. 2004.

[92] H.-K. Nienhuys, R. A. van Santen, and H. J. Bakker. Orientational relaxation of liquid water molecules as an activated process. *J. Chem. Phys.*, 112(9):8487–8494, 2000.

[93] N. V. Nucci and J. M. Vanderkooi. Temperature dependence of hydrogen bonding and freezing behavior of water in reverse micelles. *J. Phys. Chem. B*, 109:18301–18309, 2005.

[94] A. W. Omta, M. F. Kropman, S. Woutersen, and H. J. Bakker. Negligible effect of ions on the hydrogen-bond structure in liquid water. *Science*, 301:347–349, 2003.

[95] G. Otting, E. Liepinsh, and K. Wuthrich. Protein hydration in aqueous-solution. *Science*, 254:974–980, 1991.

[96] S. K. Pal, J. Peon, and A. H. Zewail. Biological water at the protein surface: Dynamical solvation probed directly with femtosecond resolution. *Proc. Natl. Acad. Sci. U. S. A.*, 99:1763–1768, 2002.

[97] T. Patzlaff, M. Janich, G. Seifert, and H. Graener. Ultrafast dynamics of water-AOT-octane microemulsions. *Chem. Phys.*, 261:381, 2000.

[98] L. Pauling. The structure and entropy of ice and of other crystals with some randomness of atomic arrangement. *J. Am. Chem. Soc.*, 57:2680–2684, 1935.

[99] I. R. Piletic, D. E. Moilanen, D. B. Spry, N. E. Levinger, and M. Fayer. Testing the core/shell model of nanoconfined water in reverse micelles using linear and nonlinear IR spectroscopy. *J. Phys. Chem. A*, 110:4985–4999, 2006.

[100] C. F. Polnaszek and R. G. Bryant. Nitroxide radical induced solvent proton relaxation: Measurement of localized translational diffusion. *J. Chem. Phys.*, 81:4038–4045, 1984.

[101] S. Raugei and M. L. Klein. An ab initio study of water molecules in the bromide ion solvation shell. *J. Chem. Phys.*, 116:196–202, 2001.

[102] U. Raviv, P. Laurat, and J. Klein. Fluidity of water confined to subnanometre films. *Nature*, 413:51–54, 2001.

[103] M. F. Reedijk, J. Arsic, F. F. A. Hollander, S. A. de Vries, and E. Vlieg. Liquid order at the interface of KDP crystals with water: Evidence for icelike layers. *Phys. Rev. Lett.*, 90(6):066103, 2003.

[104] R. Rey, K. B. Mller, and J. T. Hynes. Hydrogen bond dynamics in water and ultrafast infrared spectroscopy. *J. Phys. Chem. A*, 106:11993–11996, 2002.

[105] Y. L. A. Rezus and H. J. Bakker. On the orientational relaxation of HDO in liquid water. *J. Chem. Phys.*, 123:114502, 2005.

[106] Y. L. A. Rezus and H. J. Bakker. Orientational dynamics of isotopically diluted H_2O and D_2O. *J. Chem. Phys.*, 125:144512, 2006.

[107] K. Rottger, A. Endriss, J. Ihringer, S. Doyle, and W. F. Kuhs. Lattice-constants and thermal-expansion of H_2O and D_2O ice Ih between 10 and 265 K. *Acta Crystallogr., Sect. B: Struct. Sci.*, 50:644–648, Dec. 1994.

[108] J. A. Rupley and G. Careri. Protein hydration and function. *Advances in Protein Chemistry*, 41:37–172, 1991.

[109] G. M. Sando, K. Dahl, and J. C. Owrutsky. Vibrational relaxation dynamics of azide in ionic and nonionic reverse micelles. *J. Phys. Chem. A*, 108(51):11209–11217, Dec. 2004.

[110] F. Sciortino and G. Corongiu. Structure and dynamics in hexagonal ice: A molecular dynamics simulation with an ab rinifio polarizable and flexible potential. *J. Chem. Phys.*, 98:5694–5700, 1993.

[111] A. Scodinu and J. T. Fourkas. Comparison of the orientational dynamics of water confined in hydrophobic and hydrophillic nanopores. *J. Phys. Chem. B*, 106:10292–10295, 2002.

[112] G. Seifert, T. Patzlaff, and H. Graener. Size dependent ultrafast cooling of water droplets in microemulsions by picosecond infrared spectroscopy. *Phys. Rev. Lett.*, 88:147402, 2002.

[113] G. Seifert, K. Weidlich, and H. Graener. Picosecond ir hole-burning spectroscopy on HDO ice Ih. *Phys. Rev. B*, 56:231–234, 1997.

[114] M. Senō, K. Sawada, K. Araki, K. Iwamoto, and H. Kise. Properties of water in hexadecyltrimethylammonium bromide/chloroform system. *J. Colloid Interface Sci.*, 78:57–64, 1980.

[115] A. K. Simorellis, W. D. V. Horn, and P. F. Flynn. Dynamics of low temperature induced water shedding from AOT reverse micelles. *J. Am. Chem. Soc.*, 128:5082–5090, 2006.

[116] G. Sposito, N. T. Skipper, R. Sutton, S.-H. Park, A. K. Soper, and J. A. Greathouse. Surface geochemistry of the clay minerals. *Proc. Natl. Acad. Sci. U. S. A.*, 96:3358–3364, 1999.

[117] A. Staib and J. T. Hynes. Vibrational predissociation in hydrogen-bonded OH$\cdots$O complexes via OH stretch-OO stretch energy transfer. *Chem. Phys. Lett.*, 204:197–205, 1993.

[118] T. Steinel, J. B. Asbury, J. Zheng, and M. D. Fayer. Watching hydrogen bonds break: A transient absorption study of water. *J. Phys. Chem. A*, 108:10957–10964, 2004.

[119] O. Stern. Zur theorie der elektrolytischen doppelschicht. *Z. Elektrochem.*, 30:508, 1924.

[120] D. Stigter. On the adsorption of counterions at the surface of detergent micelles. *J. Phys. Chem.*, 68:3603–3611, 1964.

[121] A. Szabo. Theory of fluorescence depolarization in macromolecules and membranes. *J. Chem. Phys.*, 81:150–167, 1984.

[122] H.-S. Tan, I. R. Piletic, and M. Fayer. Orientational dynamics of water confined on a nanometer length scale in reverse micelles. *J. Chem. Phys.*, 122:174501, 2005.

[123] A. Tokmakoff. Introductory quantum mechanics II. http://oxw.mit.edu/OcwWeb/Chemistry/, 2007.

[124] M. F. Toney, J. N. Howard, J. Richer, G. L. Borges, J. G. Gordon, O. R. Melroy, D. G. Wiesler, D. Yee, and L. B. Sorensen. Voltage-dependent ordering of water molecules at an electrode-electrolyte interface. *Nature*, 368:444–446, 1994.

[125] D. S. Venables, K. Huang, and C. A. Schmuttenmaer. Effect of reverse micelle size on the librational band of confined water and methanol. *J. Phys. Chem. B*, 105:9132–913, 2001.

[126] G. E. Walrafen. Raman spectral studies of the effects of perchlorate ion on water structure. *J. Chem. Phys.*, 52(8):4176–4198, 1979.

[127] D. M. Willard, R. E. Riter, and N. E. Levinger. Dynamics of polar solvation in lecithin/water/cyclohexane reverse micelles. *J. Am. Chem. Soc.*, 120:4151–4160, 1998.

[128] T. Witten and P. Pincus. *Structured Fluids: Polymers, Colloids, Surfactants*. Oxford University Press, 2004.

[129] M. Wojcik and V. Buch. Spectra of isotopic ice mixtures. *J. Chem. Phys.*, 99:2332–2344, 1993.

[130] M. Wong, J. K. Thomas, and T. Nowak. Structure and state of H_2O in reversed micelles. 3. *J. Am. Chem. Soc.*, 99:4730–4736, 1977.

[131] S. Woutersen and H. J. Bakker. Resonant intermolecular transfer of vibrational energy in liquid water. *Nature*, 402:507–509, 1999.

[132] S. Woutersen, U. Emmerichs, and H. Bakker. A femtosecond midinfrared pump–probe study of hydrogen-bonding in ethanol. *J. Chem. Phys.*, 107:1483, 1997.

[133] S. Woutersen, U. Emmerichs, H. K. Nienhuys, and H. J. Bakker. Anomalous temperature dependence of vibrational lifetimes in water and ice. *Phys. Rev. Lett.*, 81(5):1106–1109, Aug. 1998.

[134] C. F. Wu, S. H. Chen, L. B. Shih, and J. S. Lin. Direct measurement of counterion distribution around cylindrical micelles by small-angle X-ray-scattering. *Phys. Rev. Lett.*, 61(5):645–648, Aug. 1988.

[135] Q. Zhong, A. Baronavski, and J. Owrutsky. Reorientation and vibrational energy relaxation of pseudohalide ions confined in reverse micelle water pools. *J. Chem. Phys.*, 119:9171, 2003.

[136] Q. Zhong, A. P. Baronavski, and J. C. Owrutsky. Vibrational energy relaxation of aqueous azide ion confined in reverse micelles. *J. Chem. Phys.*, 118:7074–7080, 2003.

[137] G.-W. Zhou, G.-Z. Li, and W.-J. Chen. Fourier transform infrared investigation on water states and the conformations of Aerosol-OT in reverse microemulsions. *Langmuir*, 18:4566–4571, 2002.

[138] M. Zulauf and H.-F. Eicke. Inverted micelles and microemulsions in the ternary system H_2O/Aerosol-OT/Isooctane as studied by photon correlation spectroscopy. *J. Phys. Chem.*, 83:480–486, 1979.

Summary

Water is the most abundant liquid on our planet and has a ubiquitous presence in our lives. It constitutes the main component of all living organisms, supporting the popular knowledge that water is crucial to the existence of life. When examining the role of water in biological systems, we see many examples of water not being present as a bulk liquid, but hydrating lipid or protein surfaces, often in strongly confined regions. The cell is a crowded environment in which macromolecules occupy a considerable fraction (between 10% and 40%) of the total volume. The conformations of proteins and membrane sheets in cells are often such that their surface encloses small pockets of water, either continuously or during part of their functional cycle. Confinement of water to volumes of only a few nanometre length scale is a regularly encountered motive in biological systems.

Water containing reverse micelles have emerged as a suitable model system for studying confined water. These micelles consist of small aqueous droplets that are coated by a layer of surfactant molecules, and form spontaneously in an apolar solvent. The dimensions of reverse micelles are similar to confined spaces found in cavities in biological systems. The work presented in this thesis aims at studying the properties of water inside reverse micelles and at understanding how the properties of water change as a result of confinement. In bulk water the water molecules are arranged in a dynamical hydrogen bond network, in which each molecule is near tetrahedrally coordinated by four other molecules. By confining water to small volumes this hydrogen bond network gets truncated, which may change both the structural and dynamical properties of the liquid.

Mid-infrared spectroscopy is well suited for studying the hydrogen bonding properties of water. The O–H stretch vibration of a water molecule, which absorbs in the mid-infrared spectral region, is very sensitive to the precise strength of the donated hydrogen bond. To study the dynamics of confined water, we use femtosecond pump-probe spectroscopy. In these experiments we use two short ($\sim$100 fs) infrared light pulses: a pump pulse to excite the O–H stretch vibration of a fraction of the water molecules, and a second probe pulse to monitor the absorption changes in the sample resulting from the vibrational excitation. By probing the sample at various time delays after the pump, we can measure the O–H stretch vibrational relaxation. If we perform the experiment with a combination of different pump and probe polarisations, we can also obtain information on the reorientational motions of the excited water molecules.

Most experiments have been performed on the O–H stretch vibration of isotopic dilutions of HDO in heavy water D_2O and not on neat water H_2O. In neat water vibrational excitations rapidly hop from one water molecule to another (by Förster energy transfer) and as a result we cannot measure water reorientations.

Experiments on water confined in anionic reverse micelles [using the surfactant AOT (Sodium bis(2-ethylhexyl) sulfosuccinate)] reveal that primarily two types of water molecules can be distinguished in the interior of such a reverse micelle. We find that water molecules hydrogen bonded to the outer micellar wall have a slower vibrational relaxation and a much lower orientational mobility ($\tau_{or}>15$ ps) than water molecules in the core of the reverse micelles, which behave much like bulk water ($\tau_{or}=3$ ps). The micellar confinement only affects the mobility of approximately a single layer of interfacial water molecules, and no long range effect on the orientational mobility is observed. The experiment also illustrates that the strength of its hydrogen bond does not determine the orientational mobility of a water molecule. The interfacial water molecules are more weakly hydrogen bonded than the water molecules in the micelle core, but nevertheless their mobility is lower.

The effect of confinement of water in AOT reverse micelles was also studied for neat water H_2O. Förster energy transfer in neat water causes rapid sampling of different water molecules by a single vibrational excitation. The observed dynamics is thereby averaged over the core and interfacial water molecules, and only an averaged single exponential vibrational relaxation is observed. Consistent with the results obtained for isotopically diluted water, the lifetime of the O–H stretch vibration is found to increase upon confinement ($T_1=0.85\pm0.1$ ps), which is more than three times as long as in bulk liquid water ($T_1=0.26\pm0.02$ ps).

Because specific interface-water interactions are important in explaining the different behaviour of interfacial water compared to bulk water, it is interesting to see how other surfactants than AOT affect water dynamics within reverse micelles. We therefore studied water contained in cationic instead of anionic reverse micelles, by preparing micelles with the surfactant salt CTAB (cetyltrimethylammonium bromide). For this system we find an anomalously slow vibrational relaxation rate for water that is hydrogen-bonded to the Br^- counterions of the surfactant. Such slow vibrational relaxation points to a very high local concentrations of Br^- ions (>10M). Most of the Br^- ions are found to be densely packed at the micellar interface. Such a dense layer of counterions is also observed at the interface of normal (not reversed) ionic micelles, and is referred to as the Stern layer. Within our experimental accuracy, bulk-like water in the core of the micelles is found to have an orientational mobility similar to bulk liquid water, as was found previously for anionic AOT micelles. Water bound to Br^-, found predominantly at the micellar interface, has a much lower orientational mobility, that further decreases with decreasing micelle size ($\tau_{or}=8\rightarrow55$ ps).

The confinement of liquid water to small volumes can also affect its phase behaviour and transition to solid ice. Preliminary experiments were undertaken

to first measure and understand the femtosecond pump-probe spectra of normal crystalline ice *Ih*, after which we performed experiments on ice confined in reverse micelles.

We find the vibrational lifetime of bulk HDO:D_2O ice to be 420±30 fs, and show that the OH-stretch relaxation proceeds via a localised mode which is likely the H–O–D bending vibration. A striking feature of the pure pump-probe spectrum of ice is the strongly broadened $v_{OH} = 1 \rightarrow 2$ transition. We modelled the $v_{OH} = 0 \rightarrow 1$ and $v_{OH} = 1 \rightarrow 2$ line shapes of ice using the Lippincott-Schröder model for the O–H stretch potential. Using this model, we find that the strongly broadened $v_{OH} = 1 \rightarrow 2$ line shape cannot be explained from proton delocalization in the $v_{OH} = 2$ vibrational state, as has been reported for liquid water, but that this broadening arises from a very short vibrational lifetime of the $v_{OH} = 2$ state (20±4 fs). This short vibrational lifetime can be explained from the resonance between the $v_{OH} = 1 \rightarrow 2$ transition with the overtone of the H–O–D bending mode (2900 cm^{-1}).

We find that HDO:D_2O water confined in small AOT reverse micelles can no longer freeze in a crystalline form. Instead a type of amorphous ice is observed in the micelle interior. The vibrational relaxation rate of the micellar amorphous ice is found to increase almost linearly with the O–H stretch absorption frequency, from 0.7 to 4 ps, which is considerably slower than the vibrational relaxation rate of bulk ice.

Samenvatting

De overvloedige aanwezigheid van water op onze planeet is één van de belangrijkste voorwaarden geweest voor het ontstaan van leven op aarde. Alleen al het feit dat ons lichaam voor meer dan 60% uit water bestaat, toont het belang aan van water voor het functioneren van leven. Kijken we op microscopische schaal of, nog kleiner, op moleculaire schaal naar levensprocessen, dan is de belangrijke rol van water voor leven even evident. Een levende cel is een buitengewoon drukke biochemische fabriek propvol met organellen, membranen en eiwitten waarmee de dagelijkse operaties van een cel worden uitgevoerd. Al deze structuren zijn omgeven door water, dat vaak essentieel is voor hun functie. In deze context wordt er wel gesproken van 'biologisch water'.

Water bevindt zich niet alleen aan de buitenkant van biologische structuren, het maakt er vaak actief deel van uit. Weggestopt in door membranen begrensde compartimenten, of in holtes binnenin eiwitten, vinden we watermoleculen die aan meerdere kanten worden ingeperkt. Deze inperking van water, of 'confinement' in het engels, is een veelvoorkomend motief binnen biologische structuren. Het ingeperkte water kan bestaan uit slechts een paar tot enkele duizenden water moleculen, waardoor de afmetingen van deze waterpakketjes slechts enkele nanometers zijn (miljoenste millimeters). In dit proefschrift wordt bestudeerd of zulk ingeperkt water zich anders gedraagt dan normaal puur water.

Om ingeperkt water te kunnen bestuderen gebruiken we een model-systeem: zogenaamde inverse micellen. Dat zijn zeer kleine druppeltjes water van een welbepaalde grootte, zoals afgebeeld in Figuur 1. Zulke druppeltjes ontstaan vanzelf wanneer een kleine hoeveelheid water wordt gemengd met een olie, onder toevoeging van een zeep-achtig molecuul of surfactant. Een surfactant is een molecuul met een staart die graag oplost in olie, en een kop die graag oplost in water. Een dergelijk molecuul dat zowel hydrofiele als hydrofobe delen heeft wordt een amfifiel molecuul genoemd, en dit type molecuul vormt de bouwsteen van de meeste biologische membranen. Normaal gesproken mengen water en olie buitengewoon slecht, maar door toevoeging van de surfactant onstaat een oplossing van kleine druppeltjes water omgeven door een laag surfactant moleculen, die rondzweven in een omgeving van olie. De surfactant moleculen richten hun waterminnende kop naar het water en hun waterafstotende staart naar de olie, en stabiliseren daarmee het druppeltje. Iets soortgelijks maar dan omgekeerd gebeurt bij het afwassen van een vette pan, waar het afwasmiddel kleine druppeltjes olie oplost in een omgeving van water.

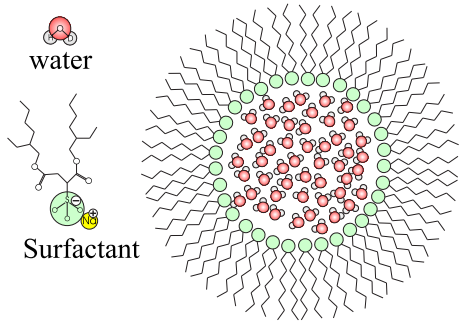

FIGUUR 1. Schematische weergave van een inverse micel, een druppel water van enkele nanometers grootte omgeven door surfactant moleculen.

Één van de belangrijkste eigenschappen van een vloeistof als water is dat deze niet statisch is, maar dynamisch, oftewel continu in beweging. De bewegingen van watermoleculen zijn ontzettend snel: een watermolecuul draait gemiddeld eens in de paar picoseconden om zijn as, oftewel in een miljoenste van een miljoenste van een seconde. Dat is vele malen sneller dan het snelste electronische apparaat, waardoor het onmogelijk is om met een camera de bewegingen van watermoleculen te filmen. Om een snelle beweging te kunnen waarnemen moet je de beweging af kunnen beelden met iets dat nog sneller is dan de beweging zelf, anders raakt de waarneming uitgesmeerd als bij het ne-

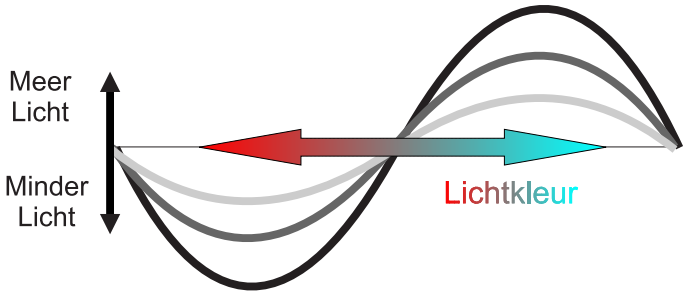

FIGUUR 2. Verandering in de hoeveelheid infrarood licht doorgelaten door water, wanneer dit water in trilling wordt gebracht met een intense infrarood (pomp) puls. De verandering in lichttransmissie is weergeven als functie van de lichtkleur, en de verschillende lijnen corresponderen met verschillende tijdstippen na de excitatie door de pomp puls. Trillende moleculen absorberen licht bij lagere frequenties, waardoor licht bij deze frequenties minder goed wordt doorgelaten. Doordat er minder niet-trillende watermoleculen zijn (ten koste van de trillende moleculen) worden de hoge frequenties juist beter doorgelaten. Naar analogie met zichtbaar licht noemen we de hogere frequenties blauw en de lagere frequenties rood. Naarmate de tijd verloopt verdwijnt het signaal als gevolg van het uitdoven van de O–H strek trillingen.

men van een sportfoto met een te lange sluitertijd. Een experimentele techniek die heel geschikt is om waterbewegingen te kunnen meten is ultrasnelle mid-infrarood pomp-probe spectroscopie. Deze meettechniek zullen we illustreren aan de hand van Figuur 2, 3 en 4.

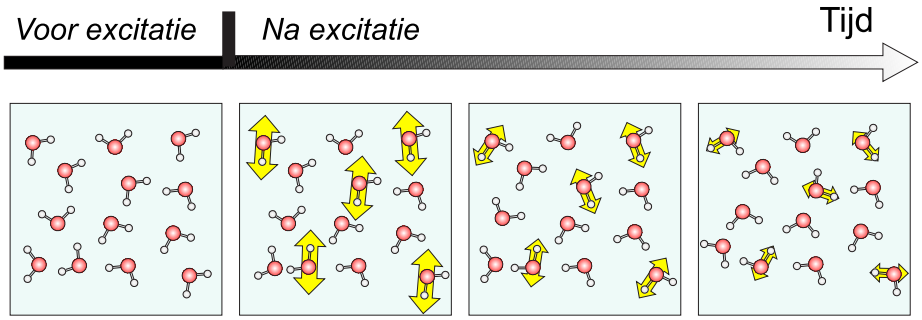

FIGUUR 3. Met behulp van een gepolarizeerde lichtpuls kunnen selectief verticaal georienteerde O–H strek vibraties in water worden aangebracht. Door draaiingen van de watermoleculen zijn na verloop van tijd evenveel vibraties horizontaal als verticaal georiëntateerd. Het aantal vibrerende moleculen in beide richtingen kan worden gemeten met een tweede probe puls. De snelheid waarmee het aantal horizontaal en verticaal trillende moleculen gelijk wordt definieert de gemiddelde reorientatietijd van een watermolecuul.

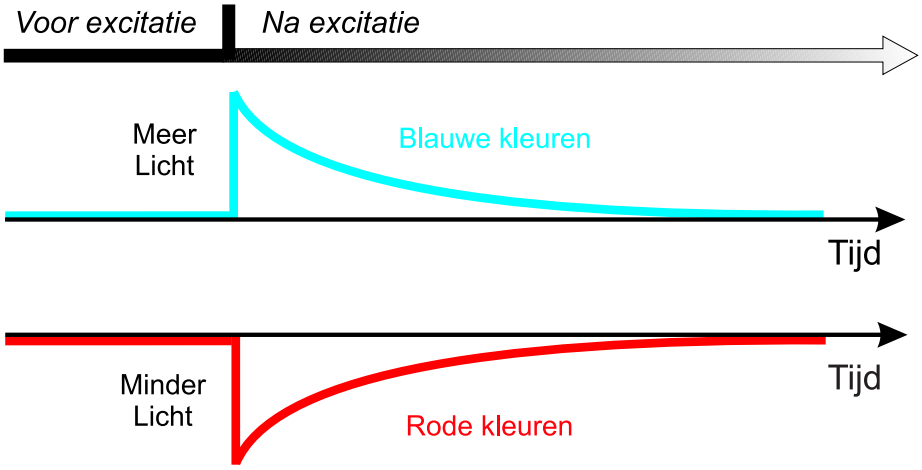

FIGUUR 4. Verandering in de hoeveelheid infrarood licht doorgelaten door water, wanneer water in trilling wordt gebracht met een intense infrarood (pomp) puls. Naarmate de tijd verloopt verdwijnt het signaal als gevolg van het uitdoven van de O–H strek trillingen.

We maken gebruik van twee ultrakorte infrarode lichtpulsen van ongeveer 0.1 picoseconde tijdsduur. Water is volledig transparant voor zichtbaar licht. Dat is anders in het infrarood, het golflengtegebied van onder andere warmtestraling van de zon. Met een intense infrarode lichtpuls (de pomp-puls) kunnen we watermoleculen in trilling brengen langs de bindingen tussen de waterstofatomen en het zuurstofatoom, de O–H strek vibraties. Omdat we een lichtpuls gebruiken waarvan het lichtveld alleen trilt in verticale richting (zogenaamd verticaal gepolarizeerd licht), brengen we alleen verticaal georienteerde moleculen in trilling (zoals aangegeven met de gele pijlen in figuur 3). Omdat de moleculen continu bewegen en hun orientatie wijzigen, blijven de O–H vibraties niet verticaal georienteerd, maar na verloop van tijd zullen steeds meer vibraties ook in de horizontale richting wijzen, en uiteindelijk trillen evenveel moleculen in beide richtingen. Hoe snel dat gebeurt hangt af van hoe snel de watermoleculen draaien.

De hoeveelheid trillende moleculen kunnen we meten met een tweede infrarode lichtpuls, de probe-puls. Een trillend watermolecuul absorbeert licht bij een rodere kleur dan een niet-trillend watermolecuul, dat blauwer licht absorbeert. Het in trilling brengen van moleculen door de pomp puls heeft daardoor tot gevolg een toename in absorptie van roder licht (als gevolg van lichtabsorptie door de trillende moleculen) en een afname in de absorptie van blauwer licht (doordat de hoeveelheid niet-trillende moleculen is afgenomen ten koste van de trillende moleculen), zoals geïllustreerd in Figuur 2 en 4. Door deze veranderingen in lichtabsorptie van de probe-puls te meten op een zekere tijd t na de pomp puls, kunnen we afleiden hoeveel moleculen op dat specifieke moment t in trilling zijn, in zowel de verticale als de horizontale orientatierichting. We moeten ons wel realiseren dat deze tijdsvertraging t van de probe puls ten opzichte van de pomp puls ontzettend kort moet zijn, en dat we deze vertraging nauwkeurig moeten kunnen variëren. Daartoe maken we gebruik van de lichtsnelheid: we laten de probe puls over een pad lopen dat we langer of korter maken. Omdat de lichtsnelheid eindig is kunnen we de vertraging ten opzichte van de pomp puls regelen door de padlengte aan te passen (zo komt 0.3 millimeter padlengte overeen met 1 picoseconde).

Behalve rotatiesnelheden van watermoleculen kunnen we ook de trillingstijden van watermoleculen bepalen: na de excitatie van een watermolecuul door de pomp-puls dooft de trilling in het molecuul geleidelijk uit, net zoals het geluid en de trilling van een kerkklok uitdooft nadat deze is aangeslagen. De vibratietijd van een watermolecuul kan sterk afhangen van de omgeving waarin het zich bevindt. Zo blijken we in veel gevallen een verschil in trillingstijd te kunnen gebruiken om biologisch water te onderscheiden van normaal water.

Wat zien we nu als we met deze techniek de zeer kleine waterdruppeltje bestuderen, die we hebben gemaakt in de vorm van inverse micellen? Onze experimenten laten zien dat watermoleculen in de buitenste schil van zo'n druppeltje (zogenaamd interface water) zich heel anders gedragen dan watermoleculen in het binnenste van de micellen (zogenaamd core water), zoals aangegeven in Figuur 5. Het interface water staat vrijwel stil, terwijl het core water net zo beweeglijk is als normaal water. Slechts een laagje met een dikte van 1-2 wa-

termoleculen wordt beïnvloed door het inperkende oppervlak van de surfactant moleculen, en al op zeer korte afstand van dit oppervlak gedraagt het water zich weer normaal.

De surfactant moleculen waarmee micellen worden gevormd zijn vaak zouten; de hydrofiele kopgroep van het molecuul heeft een lading die gecompenseerd wordt door een los ion van tegengestelde lading. Door de trillingstijd van water rondom deze losse ionen te bepalen kunnen we afleiden hoe de losse ionen binnen de waterdruppeltjes zijn verdeeld. Hieruit blijkt dat de meeste ionen zich zeer sterk concentreren in de buitenste schil van de druppeltjes, grenzend aan de surfactant moleculen. De precieze eigenschappen van de grenslaag waar het water wordt ingeperkt wordt daarom voor een belangrijk deel bepaald door de eigenschappen van deze ionen.

In een vervolgexperiment bij lage temperaturen laten we zien dat de inperking van vloeibaar water ook de wijze van bevriezen van water verandert. Normaal water kristalliseert in een faseovergang naar ijs. De posities van de watermoleculen in een ijskristal zijn netjes geordend, terwijl water in de vloeistoffase veel wanordelijker is. Ingeperkt water in kleine inverse micellen blijkt niet te kristalliseren. De watermoleculen in de micel verliezen wel hun beweeglijkheid, echter met behoud van de wanordelijke structuur die kenmerkend is voor vloeibaar water. Voor zowel normaal ijs als voor ijs ingeperkt in micellen hebben we de energierelaxatie van de O–H strek vibratie gemeten. Voor normaal ijs vinden we dat het absorptiespectrum van trillende moleculen veel breder is dan het absorptiespectrum van niet-trillende moleculen. Aan de hand van een theoretische berekening van deze absorptiespectra komen we tot de conclusie dat deze spectrale verbreding wordt veroorzaakt door zeer snelle energie-overdracht naar de buigvibratie van water.

Concluderend kunnen we stellen dat de inperking van water heel sterke effecten heeft op de dynamica van water dat grenst aan het oppervlak: de reorientatietijd wordt meer dan vijf keer trager, en de energierelaxatie ongeveer vier keer trager in vergelijking met normaal water. De invloed van een inperkend oppervlak is van zeer korte dracht en enkele waterlagen vanaf het oppervlak gedraagt water zich praktisch als normaal water. In de context van biologische systemen speelt daarom het interface water verreweg de belangrijkste biologische functie.

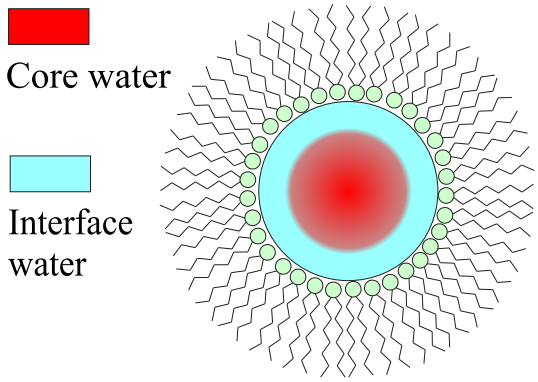

FIGUUR 5. Schematische weergave van een inverse micel. Het water in de buitenste schil van de micel (interface water) is veel minder mobiel dan het water in de kern (core water), dat zich vrijwel gedraagt als normaal water.

Dankwoord

Tijdens mijn promotieonderzoek heb ik het geluk gehad te kunnen beschikken over twee directe begeleiders, wat maakte dat ik nooit om aandacht verlegen heb gezeten. Zowel Huib Bakker als Sander Woutersen wil ik bedanken voor de opvallend losse sfeer waarin we hebben samengewerkt, en voor hun enthousiasme tijdens onze vele wetenschappelijke discussies. Direct vanaf de eerste ontmoeting heb ik me thuis gevoeld op de ultrasnelle afdeling. Huib was nooit de gedistingeerde professor of de baas die zei wat je moest doen, maar meer de groepsgenoot bij wie je als eerste aanklopte met een probleem en bij wie je nooit een blad voor de mond hoefde te nemen. Had Huib licht anarchistische trekjes, dan deed Sander daar graag een schepje bovenop, wat vaak leidde tot hilarische conversaties of een kijkje in juist die keuken waar je eigenlijk niet mocht zijn, maar wel alles van wilde weten.

Van het begin af aan is me een grote vrijheid gegeven om het onderzoek zelf in te vullen. Net als in het echte leven is het maken van keuzes in de wetenschap belangrijk, want de tijd schrijt altijd voort. Gelukkig kregen zelfstandigheid en eigen verantwoordelijkheid alle ruimte voor ontwikkeling in de leerschool van Sander en Huib. Tot mijn spijt verhuisde Sander halverwege mijn promotie naar de UvA, maar op wetenschappelijk en bovenal moreel vlak bleef hij altijd van grote steun, net als zijn partner Saskia die mij menig toekomstgerichte tip aan de hand heeft gedaan.

Hinco Schoenmaker ben ik buitengewoon erkentelijk voor het oplossen van vele technische problemen, met een handigheid en snelheid waar ik vaak versteld van stond. Ik zal ook nooit de vreugde vergeten toen Idsart en Henk de laser wisten te reanimeren toen ik al dacht dat deze definitief bij het schroot gezet moest worden.

Meerdere generaties promovendi en post-docs zijn de afgelopen vier jaar voorbij getrokken. Vanaf het eerste uur waren dat Joop, Michel, Arjan, Dorte, Anne Willem en Olaf, en niet te vergeten Thomas met wie je na werktijd uren kunt zitten praten om je vervolgens te realiseren dat het nog geen minuut over natuurkunde is gegaan. Later volgden Rutger, Sergiy, Han-Kwang en Bradley, die lange tijd mijn aanstekelijk enthousiaste kamergenoot was. Voor een goede tijd dank ik ook mijn latere kamergenoten Klaas-Jan en Pavol, die onze kamer tot een oase van rust maakten (behalve dan wanneer Pavol en Sander de hotline tussen Amolf en UvA opereerden), waar je een verloren minuutje kon wegdromen bij de buitelende mezen, spechten en boomkruipers van de binnentuin.

De Bakker-groep werd ten slotte versterkt door Jocelyn (i.e. JoJo, muzikaal metgezel), Łukasz (i.e. Komrad Kukasz, komediant), Christian en Nuria. Yves Rezus is van de buitencategorie. Hij was er altijd, en het was goed te delen in zowel de lol als de onvermijdelijke frustratie die naar voren komt bij het doen van wetenschap. Harm Geert Muller was een onuitputtelijk orakel voor als je het echt niet meer wist. Edgar Groenen is als afstudeerbegeleider van grote invloed geweest op mijn natuurkundige carrière, en ik wil hem bedanken voor het contact dat we ook de laatste jaren hebben gehad.

De meeste betrokkenheid en steun tijdens mijn promotie ontving ik van mijn partner in crime Lenie, met wie ik vele avonturen en eye-openers beleefde en die me als geen ander heeft geholpen bij het maken van de grote keuzes. Ook Pieter gaf mij hierbij steuntjes in de rug, zowel op de baan als in de buitenlandse bush. Ten slotte bedank ik mijn ouders voor de goede thuishaven en vrienden en familie voor een mooie tijd.